Research Paper

GEOSPHERE

GEOSPHERE, v. 20, no. 6

https://doi.org/10.1130/GES02704.1

13 figures; 7 tables; 1 set of supplemental files

CORRESPONDENCE: aforte8@lsu.edu

CITATION: Forte, A.M., Cowgill, E.S., Sumner, D.Y., Garello, D.I., Niemi, N.A., and Fowler, K.C., 2024, Timing and evolution of structures within the southeastern Greater Caucasus and Kura Fold-Thrust Belt from multiproxy sediment provenance records: Geosphere, v. 20, no. 6, p. 1533–1574, https://doi.org/10.1130/GES02704.1.

Science Editor: Andrea Hampel
Associate Editor: Joel Saylor

Received 1 August 2023
Revision received 29 July 2024
Accepted 17 September 2024

Published online 25 October 2024

Timing and evolution of structures within the southeastern Greater Caucasus and Kura Fold-Thrust Belt from multiproxy sediment provenance records

Adam M. Forte[1], Eric S. Cowgill[2], Dawn Y. Sumner[2], Dominique I. Garello[1], Nathan A. Niemi[3], and K. Colton Fowler[1]

[1]Department of Geology and Geophysics, Louisiana State University, Baton Rouge, Louisiana 70803, USA
[2]Department of Earth and Planetary Sciences, University of California, Davis, California 95616, USA
[3]Department of Earth and Environmental Sciences, University of Michigan, Ann Arbor, Michigan 48109, USA

ABSTRACT

The Greater Caucasus (GC) mountains are the locus of post-Pliocene shortening within the northcentral Arabia-Eurasia collision. Although recent low-temperature thermochronology constrains the timing of orogen formation, the evolution of major structures remains enigmatic—particularly regarding the internal kinematics within this young orogen and the associated Kura Fold-Thrust Belt (KFTB), which flanks its southeastern margin. Here we use a multiproxy provenance analysis to investigate the tectonic history of both the southeastern GC and KFTB by presenting new data from a suite of sandstone samples from the KFTB, including sandstone petrography, whole-rock geochemistry, and detrital zircon (DZ) U-Pb geochronology. To define source terranes for these sediments, we integrate additional new whole-rock geochemical analyses with published DZ results and geological mapping. Our analysis reveals an apparent discrepancy in up-section changes in provenance from the different methods. Sandstone petrography and geochemistry both indicate a systematic up-section evolution from a volcanic and/or volcaniclastic source, presently exposed as a thin strip along the southeastern GC, to what appears similar to an interior GC source. Contrastingly, DZ geochronology suggests less up-section change. We interpret this apparent discrepancy to reflect the onset of sediment recycling within the KFTB, with the exhumation, weathering, and erosion of early thrust sheets in the KFTB resulting in the selective weathering of unstable mineral species that define the volcaniclastic source but left DZ signatures unmodified. Using the timing of sediment recycling and changes in grain size together as proxies for structural initiation of the central KFTB implies that the thrust belt initiated nearly synchronously along strike at ~2.0–2.2 Ma.

1. INTRODUCTION AND MOTIVATION

The provenance histories of siliciclastic sedimentary rocks in foreland basins commonly provide a robust and, in some cases, singular record of the past structural and kinematic history of the flanking orogenic system (e.g., Sinclair, 1997; DeCelles et al., 1998; Lawton et al., 2010; Nagel et al., 2014; Leary et al., 2016; Capaldi et al., 2020). In detail, shifts in sediment provenance recorded in forelands can elucidate the order of initiation, direction of propagation, and style of structures within a mountain range, thus providing crucial constraints for tectonic models of orogen evolution (e.g., Carrapa et al., 2006; Panaiotu et al., 2007; Bande et al., 2012; Laskowski et al., 2013; Garber et al., 2020). The resulting information on both absolute and relative timing of structures can prove especially important in evaluating the extent to which particular mountain ranges obey the expected behavior of critically tapered orogenic wedges (e.g., Davis et al., 1983; Dahlen and Suppe, 1988; Dahlen, 1990). For example, critical wedge theory suggests a direct relationship between the efficiency of climate and the width of mountain ranges (e.g., Stolar et al., 2006; Whipple and Meade, 2006; Roe et al., 2008), where changes in width would be reflected in part in the order of initiation of structures and degree of temporal synchronicity of structural changes within the orogen and causative climatic changes. A potential example of this can be found in the Greater Caucasus (GC) and associated Kura Fold-Thrust Belt (KFTB; Fig. 1), where some prior work suggested that initiation of the fringing fold-thrust belts, including the KFTB, may reflect a climatically driven widening of the orogen after a shift to more arid conditions (e.g., Forte et al., 2013, 2022). Testing this hypothesis has been hindered in part by the relatively poor constraints on relative timing and along-strike patterns of initiation of individual structures within the range and foreland. Here we consider the extent to which sediment provenance can elucidate the structural history of both the southeastern GC and KFTB and help to resolve whether the growth of the KFTB was largely synchronous along strike and is thus compatible with climatically induced widening of the orogen.

Specifically, while recent work by Trexler et al. (2022, 2023) has significantly clarified the locations, geometry, and nature of many of the first-order structures within the internal GC, the timing and evolution of these first-order structures remain under-constrained, with the exception of very specific locations in the western GC (Vasey et al., 2020) and extreme eastern GC (Tye et al., 2022). Similarly, while it is relatively well constrained that since initiation, portions of the KFTB have accommodated upwards of 50% of the

Adam M. Forte https://orcid.org/0000-0003-4515-7792

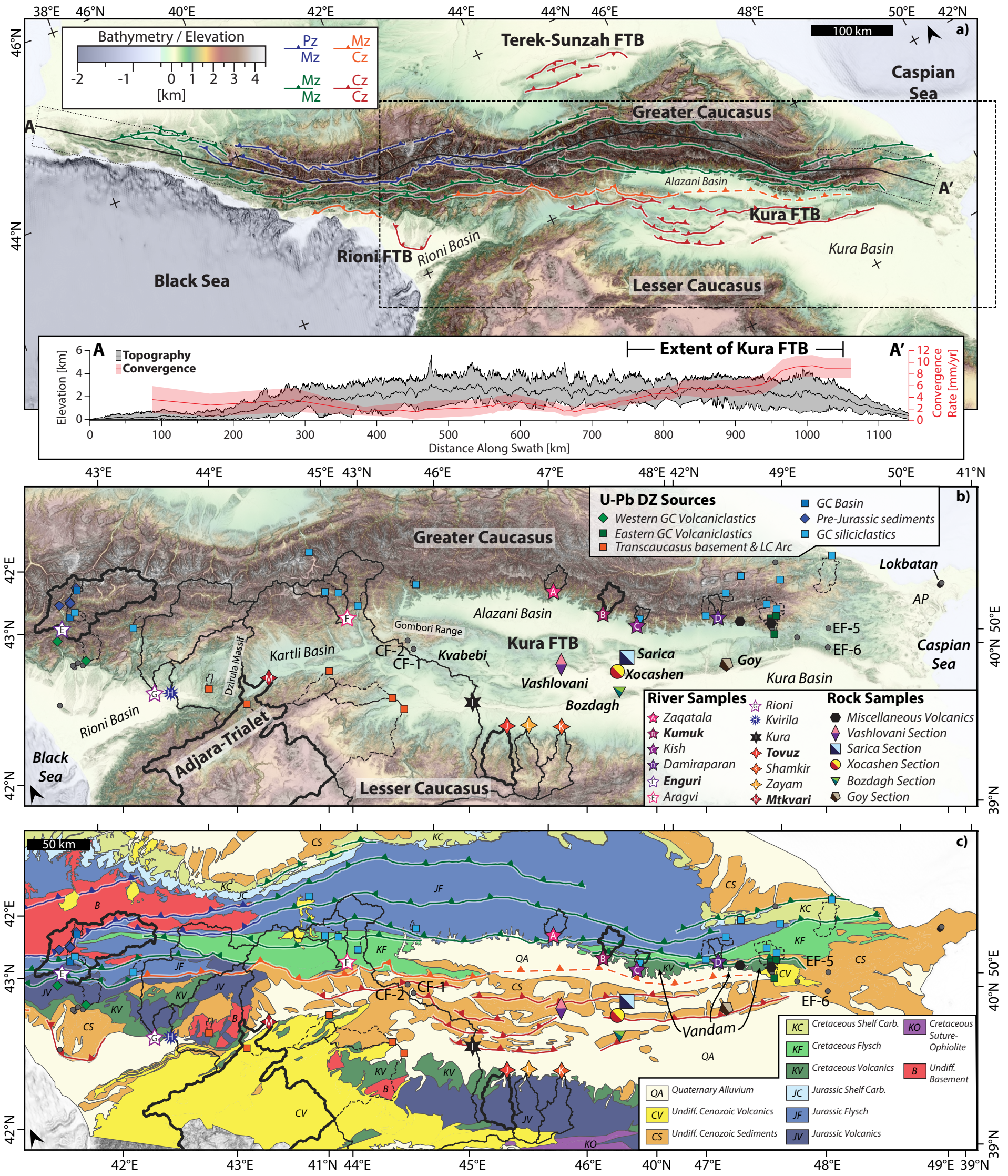

Figure 1. Tectonic context, sample locations, and regional geology of the Caucasus region. (A) Locations of major thrusts from Trexler et al. (2022), colored by ages of strata they structurally juxtapose (Pz—Paleozoic; Mz—Mesozoic; Cz—Cenozoic). Bottom inset shows swath profiles that display maximum, minimum, and mean topography within A-A′ swath profile (gray) and maximum, minimum, and mean estimated N25°E convergence rates between Greater and Lesser Caucasus (red) as modified from Forte et al. (2022), which provides further discussion of these plots. Dashed box outlines extent of lower two panels. (B) Map showing locations of modern river and bedrock samples, as explained in the bottom-right legend. Also shown are locations of samples and their respective detrital zircon (DZ) U-Pb source terranes from Tye et al. (2020) and references therein, plus additional samples from Forte et al. (2022), as explained in the top-right legend. Black lines indicate watershed boundaries for modern sediment samples; bold watershed boundaries indicate catchments for which we present geochemical data and Cowgill et al. (2016) presented DZ geochronology. Note that modern river samples for Kura and Mtkvari Rivers represent samples from the same river, where Mtkvari is sampled upstream from Kura and reflects Georgian (Mtkvari) and Azerbaijani (Kura) names for the river. Gray circles are other foreland provenance samples from Tye et al. (2020), Allen et al. (2006), and Abdullayev et al. (2018), including several suites from the Apsheron Peninsula (AP). Previous foreland samples from Tye et al. (2020) that we discuss in detail are labeled with their sample names (CF-#, EF-#). GC—Greater Caucasus; LC—Lesser Caucasus. Elevation scale the same as in panel A. (C) Same as B but over a map showing a simplified version of bedrock geology from Forte et al. (2014). Also highlighted is the zone of predominantly Cretaceous volcanic and volcaniclastic rocks in the eastern Greater Caucasus, which we refer to here as the Vandam zone, consistent with prior literature (e.g., Tye et al., 2022). FTB—Fold-Thrust Belt; undiff.—undifferentiated; carb.—carbonates.

orogen-perpendicular shortening between Arabia and Eurasia and nearly all of the convergence between the GC and Lesser Caucasus (LC) between 45°E and 49°E (Forte et al., 2010, 2013), the exact timing of KFTB initiation and the extent to which the structures within the KFTB initiated diachronously or synchronously along strike both remain unclear.

The formation of the KFTB is coincident with either a reduction in activity or large-scale abandonment of the GC range front thrust(s) (e.g., Forte et al., 2010; Mosar et al., 2010) and represents a southward advance of the active thrust front by ~25–100 km, implying significant widening of the orogen and simultaneous formation of the Alazani piggyback basin (Fig. 1). As such, the formation of the KFTB reflects a significant structural reorganization within the southeastern GC (e.g., Forte et al., 2010; Mosar et al., 2010), and constraining the timing and evolution of deformation within the KFTB is critical for understanding the broader structural evolution of the GC and the context of this reorganization. For example, based on relatively limited data, Forte et al. (2013) originally hypothesized that initiation of the KFTB and resultant widening of the GC initiated at 1.5–1.8 Ma, coincident with regional records of an increase in aridity (e.g., Kvavadze and Vekua, 1993; Gabunia et al., 2000; Kovda et al., 2008; Messager et al., 2010a, 2010b). Forte et al. (2013) considered that this shift to more arid conditions could have initiated orogen widening and KFTB formation, consistent with the proposal that active, doubly vergent orogens experiencing less-efficient erosion would expand (Whipple and Meade, 2004, 2006). If orogenic widening driven by climatic forcing is a viable mechanism to explain the formation of the KFTB, this fundamentally predicts that initiation of the KFTB was synchronous along strike.

While some prior work suggested a diachronous initiation of the KFTB along strike (Forte et al., 2010), recent constraints suggest a more synchronous initiation is viable, although these constraints come from the western and eastern termini of the belt (Fig. 2; Forte et al., 2013; Lazarev et al., 2019; Sukhishvili et al., 2021). The eastern KFTB initiated at ~2.1 Ma at the boundary between the Akchagylian and Apsheronian regional stages (Forte et al., 2013; Lazarev et al., 2019), and the western KFTB in the Gombori Range (eastern Georgia) initiated sometime between 2.7 and 1 Ma (Sukhishvili et al., 2021). To better understand the tectonic context of the KFTB, it is necessary to establish the timing of the central KFTB and the relationship between thrust propagation and evolution of structures internal to the southeastern GC. Here we investigate these problems by tracking changes in provenance in the foreland sedimentary strata now exposed within the KFTB.

Prior work describing source terranes within the GC broadly suggest relatively distinct, thrust-bounded packages that have the potential to have left diagnostic signatures within the strata deformed by the KFTB (e.g., Cowgill et al., 2016; Tye et al., 2020). However, the previously available provenance data within the Kura Basin and associated KFTB region are limited and focused primarily on the oil-producing sandstones of the Productive Series at the eastern edge of the Kura Basin (Morton et al., 2003; Allen et al., 2006; Abdullayev et al., 2018) or on strata at its western and eastern ends, all of which are inferred to largely predate formation of the KFTB (Tye et al., 2020).

To explore the tectonic history of both the southeastern GC and KFTB, we present new detailed provenance analyses from Miocene–Pleistocene sedimentary rocks that are now exposed within the central portion of the KFTB. A majority of prior provenance work within the GC focused on either detrital zircon (DZ) U-Pb geochronology (Allen et al., 2006; Cowgill et al., 2016; Abdullayev et al., 2018; Tye et al., 2020) or sandstone and/or modern sediment petrography or geochemistry (Vincent et al., 2013; Vezzoli et al., 2014, 2020). We build on this context and consider U-Pb ages from detrital zircons, sandstone composition from petrography, and bulk-sample major and trace element geochemical data. To compare source characterizations between DZ and geochemical and/or framework grain compositions, we supplement our foreland samples with additional geochemical analyses of both modern sediments from rivers draining the southern GC and northern LC and Mesozoic-aged sandstone and volcanic rocks within the GC. With these data, we specifically address the following questions: (1) How did the provenance of the northern Kura Basin evolve during the early growth of the GC? (2) What does the evolution of foreland provenance during this time suggest for structural evolution of the southeastern GC? (3) Does the provenance constrain the timing of KFTB initiation and along-strike evolution, and if so, did the belt initiate synchronously along strike as predicted by models of climatic modulation of a bivergent orogenic wedge?

The results of our multiproxy approach reveal fundamental, and in many ways confusing, disconnects between implied provenance changes from geochemistry and petrography compared to DZ geochronology. On the one hand, the geochemistry and petrography data suggest a general up-section shift from one GC-related source to another that appears to have occurred asynchronously across the basin. On the other hand, a more limited data set of DZ geochronology suggests effectively static sediment sourcing through time. We interpret this apparent discrepancy to result from sediment recycling, where the apparent up-section change in provenance inferred from the geochemical and petrographic data is a signal generated by selective weathering. Specifically, we infer that exhumation, exposure, weathering, and erosion of foreland basin sediments from thrust sheets within the KFTB led to selective weathering of components that are diagnostic of one of the key GC source terranes, thus producing a signal that looks like a change in provenance. As a result, we argue that the onset of this sediment recycling signal is actually indicative of the timing of structural initiation of portions of the KFTB and thus helps to establish the timing and along-strike evolution of the KFTB and place it in tectonic context with the structural evolution of the southeastern GC.

2. BACKGROUND

2.1 Tectonic Setting

The GC mountains are the main locus of Arabia-Eurasia convergence at their longitude and form the northern structural margin of the collision (Fig. 1; e.g.,

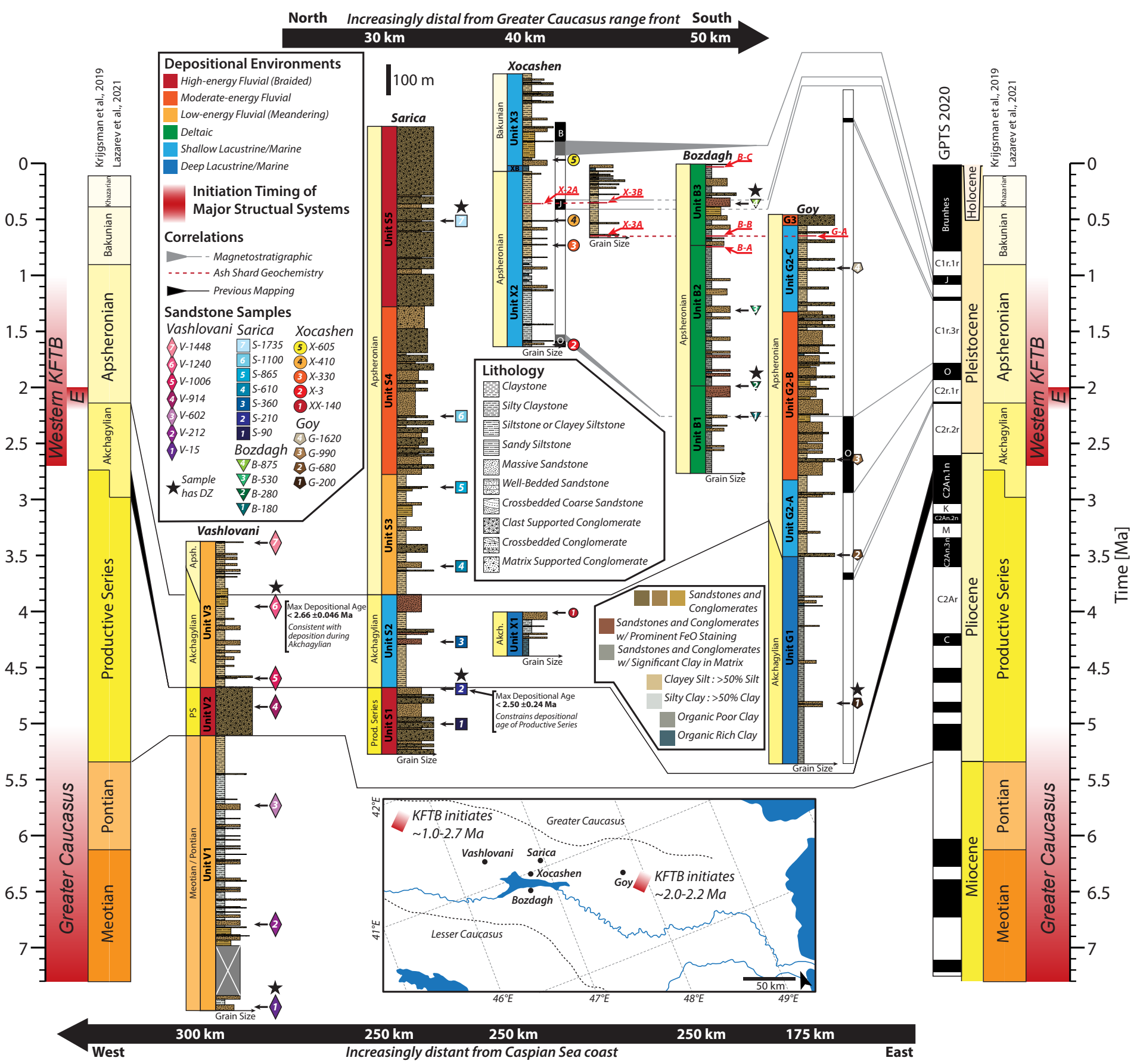

Figure 2. Stratigraphic correlations of measured sections based on ash geochemistry (red lines), published magnetostratigraphy (Van Baak et al., 2013; Lazarev et al., 2019) (gray lines), and previous mapping (Abdullaev et al., 1957; Ali-Zade, 2005; Forte, 2012; Forte et al., 2015a) (black lines). Colored symbols with numbers to the right of each column indicate samples analyzed here. Boxes containing unit names within each section are colored by depositional environment, as indicated in legend. Black lines show our correlations between the sections, global geomagnetic polarity time scale (GPTS; Ogg, 2020), and regional time scales of Krijgsman et al. (2019) and Lazarev et al. (2021), which differ in Akchagylian duration. In Vashlovani and Goy sections, diagonal boundaries between Akchagylian and Apsheronian indicate uncertainty in exact location of the boundary within the measured section. Inset map shows locations of stratigraphic sections (black dots) and areas (boxes with red gradients) where timing of the Kura Fold-Thrust Belt (KFTB) initiation is constrained to east (Forte et al., 2013; Lazarev et al., 2019) and west (Sukhishvili et al., 2021). Vertical bars with red shading on the timeline indicate initiation ages of major structures in the region (E—eastern KFTB). DZ—detrital zircon.

Philip et al., 1989; Jackson, 1992; Allen et al., 2004; Dhont and Chorowicz, 2006; Reilinger et al., 2006). The range results from ongoing Cenozoic shortening that partially inverted a Jurassic–Cretaceous back-arc basin, which opened north of the Pontide-LC island arc during north-directed subduction of Neotethyan oceanic lithosphere (e.g., Adamia et al., 1977; Gamkrelidze, 1986; Zonenshain and Le Pichon, 1986; Cowgill et al., 2016; Vincent et al., 2016; van Hinsbergen et al., 2019; Vasey et al., 2021). Significant debate has centered on the early Cenozoic geometry and dimensions of the GC back-arc basin north of the LC (Cowgill et al., 2016, 2018; Vincent et al., 2016, 2018), but paleogeographic reconstructions constrain the NE-SW width to being between 200 and 400 km (van der Boon et al., 2018; van Hinsbergen et al., 2019; Darin and Umhoefer, 2022), similar to the dimensions of the Black Sea and South Caspian Basins, which are likely remnants of the same back-arc basin system (Zonenshain and Le Pichon, 1986). Timing of initiation of closure and shortening of the GC back-arc basin is unclear but had likely begun by the Eocene–Oligocene (e.g., Vincent et al., 2007) and was accommodated in part by northward subduction of oceanic or transitional lithosphere, based on seismic evidence of a subducted slab in the eastern GC (Skobeltsyn et al., 2014; Mumladze et al., 2015; Gunnels et al., 2020). The timing of the transition from subduction to collision and beginning of significant upper-plate shortening and exhumation has also proven controversial, but recent new results from, and syntheses of, low-temperature thermochronology data have largely confirmed the original suggestion by Avdeev and Niemi (2011) of initiation of rapid exhumation between 10 and 5 Ma throughout much of the range (e.g., Vincent et al., 2020; Forte et al., 2022; Tye et al., 2022; Cavazza et al., 2023). Subsequently, active deformation and the locus of shortening at the surface have largely shifted to a series of fringing foreland fold-thrust belts in the northcentral and northwestern (Sobornov, 1994, 1996, 2021; Forte et al., 2014), southwestern (Banks et al., 1997; Tsereteli et al., 2016; Tibaldi et al., 2017, 2018, 2021; Trexler et al., 2020; Alania et al., 2021b), southcentral (Alania et al., 2021a), and southeastern (Forte et al., 2010, 2013, 2014; Alania et al., 2015) GC. The initiation of the majority of these fold-thrust belts is broadly constrained to have occurred during the Plio-Pleistocene. Our focus here is on clarifying the initiation age of the southeastern fold thrust-belt, i.e., the KFTB.

2.2 Regional Geology

The geology of the central and eastern GC (Fig. 1C) is dominated by Jurassic to Cretaceous shallow-marine carbonate rocks along the northern flank, Jurassic to Cretaceous flysch to molasse within much of the core of the orogen, and Jurassic to Cretaceous volcanic and volcaniclastic rocks along the southern flank (e.g., Saintot et al., 2006; Adamia et al., 2011a; Forte et al., 2014; Cowgill et al., 2016; Tye et al., 2020). Three observations of the regional geology are particularly important with respect to sediment provenance and potential source terranes for sediments within the Kura foreland basin. First, within the GC, intrusive, metamorphic, and metasedimentary rocks predating Jurassic rifting in the GC back-arc basin are exposed only in the western GC (undifferentiated basement in Fig. 1C; Saintot et al., 2006; Adamia et al., 2011a). Second, there are two geographically distinct sequences of predominantly Jurassic to Cretaceous volcanic and/or volcaniclastic rocks exposed along the southern margin of the GC, with the one in the west being more extensively exposed and having a wider cross-strike width than the one in the east; the latter is sometimes referred to as the Vandam zone, and both are considered to be genetically linked with the similarly aged Pontide-LC arc (e.g., Kopp and Shcherba, 1985). Third, and finally, there are various small exposures of Precambrian to Paleozoic crystalline rocks within the Dzirula Massif (Zakariadze et al., 1998; Mayringer et al., 2011; Shengelia et al., 2012) and LC (e.g., Khrami and Loki Massifs; Gamkrelidze et al., 2011; Rolland et al., 2011).

Structurally, the interior of the GC is dominated by south-directed thrusts and reverse faults that progressively steepen toward the interior of the range (Fig. 1; Philip et al., 1989; Saintot et al., 2006; Mosar et al., 2010; Adamia et al., 2011b; Somin, 2011; Trexler et al., 2022, 2023). While many prior works described the structural architecture of the internal GC in the context of a single master structure or structures, commonly referred to as the Main Caucasus Thrust (e.g., Philip et al., 1989; Mosar et al., 2010), recent work has suggested that the majority of thrusts along the southern margin of the range accommodate similar amounts of displacement (Vasey et al., 2020; Trexler et al., 2022), and especially in the eastern GC, it is actually unclear which structure(s) should be considered the Main Caucasus Thrust (e.g., Forte et al., 2015b, and discussions therein). More critical to our efforts are that many of these structures juxtapose rocks of different composition and/or DZ age populations, so that initiation and activity of these structures during deformation of the GC is expected to have produced diagnostic provenance changes in the foreland basin (Fig. 1). Of particular importance is the Vandam zone (Fig. 1C), a thrust-bounded terrane of predominantly Mesozoic-aged volcanic and volcaniclastic rocks that is likely a continuation of, or at least genetically linked to, the LC arc (Kopp and Shcherba, 1985). The Vandam zone was accreted into the range between 13 and 3 Ma and subsequently deformed (Tye et al., 2022).

2.3 Prior Work on Source Terranes

Potential source terranes and their expected provenance signatures in foreland strata of the Caucasus region are relatively well characterized in terms of U-Pb ages of zircons (Allen et al., 2006; Wang et al., 2011; Cowgill et al., 2016; Vasey et al., 2020; Tye et al., 2020; Forte et al., 2022; Trexler et al., 2022) and, to a lesser extent, heavy mineral assemblages (Morton et al., 2003; Morton and Yaxley, 2007; Vezzoli et al., 2014, 2020). Prior work by Tye et al. (2020) integrated both modern sediments and bedrock samples (Allen et al., 2006; Wang et al., 2011; Cowgill et al., 2016; Vasey et al., 2020; Trexler et al., 2022) to define a suite of seven distinct source terranes distinguishable in DZ U-Pb age populations within the Caucasus region: Eurasian interior, pre-Jurassic sedimentary rocks, GC basement, GC siliciclastic strata, eastern GC

volcaniclastics, western GC volcaniclastics, and Transcaucasus basement and LC arc. While these individual sources do not correspond to single mapped units (Tye et al., 2020), they do define three broad geographic groups: those that reflect a source from the East European craton to the north of the GC (Eurasian interior), a GC source (pre-Jurassic sedimentary rocks, GC basement, GC siliciclastic strata, eastern GC volcaniclastics, and western GC volcaniclastics), or a LC source (Transcaucasus basement and LC arc). In more detail, the GC sources roughly correspond to distinct tectonostratigraphic and, in part, geographic zones within the GC itself, with the pre-Jurassic sedimentary rocks and GC basement reflecting exposures in the core of the western orogen, the GC siliciclastics corresponding to the Jurassic to Cretaceous flysch exposed throughout the range, and the western and eastern GC volcaniclastics corresponding to the two volcanic packages along the southern range front, the latter of which is also effectively the same as the Vandam zone (Fig. 1). The seven source terranes defined by Tye et al. (2020) largely reflect differences in the relative proportions of six different distinct age populations within given samples, specifically: (1) grains <90 Ma associated with the LC arc; (2) grains 90–200 Ma associated with the LC arc or GC rifting; (3) grains 200–380 Ma associated with the Variscan orogeny; (4) grains 380–500 Ma associated with an earlier arc that formed along, and then rifted from, the former northern margin of Gondwana prior to accretion onto the southern margin of Eurasia (Laurussia); (5) grains 500–900 Ma associated with the Pan-African orogeny; and (6) >900 Ma grains associated with the East European craton. Recently, alternative characteristic age divisions within GC and LC DZ ages have been presented by Vasey et al. (2024) that clarify details of the Mesozoic and Paleozoic history of the region, but because the exact interpretations of these age divisions are not critical for our understanding of the recent (i.e., late Cenozoic) structural history of the GC or KFTB, we elect to maintain the somewhat simpler divisions of Tye et al. (2020).

A relatively smaller amount of work in terms of geographic area covered has considered the heavy mineral assemblage of potential source terranes within the Caucasus region (e.g., Morton et al., 2003; Morton and Yaxley, 2007; Vincent et al., 2007; Vezzoli et al., 2014, 2020). Here we focus on results from Morton et al. (2003) and Morton and Yaxley (2007) because Vezzoli et al. (2014, 2020) focused on sources in the far western and northern GC, which do not appear to be relevant for provenance within the Kura Basin. Morton et al. (2003) and Morton and Yaxley (2007) considered heavy mineral assemblages from the modern Volga River (which represents contributions from the East European craton), the modern Kura River (which drains both the GC and LC), and several smaller rivers draining the eastern tip of the GC. Broadly, the results highlight relatively distinct provenance signatures between all three sources. The Volga River is dominated by primarily stable, more evolved and felsic components. In contrast, the Kura River is dominated by more unstable components like clinopyroxene and amphibole sourced from extensive volcanic deposits in the LC. Finally, the GC reflects a mixture of both stable and unstable components, including species like clinopyroxene, but generally in lower abundances than in the Kura River (Morton et al., 2003; Morton and Yaxley, 2007).

2.4 Kura Basin Framework and Regional Time Scale

Here we focus primarily on the stratigraphic framework of the Kura Basin, a foreland basin to the southeast of the GC and subbasin of the South Caspian Basin (Fig. 1; e.g., Khain, 1975; Philip et al., 1989; Kremenetskiy et al., 1990). Although at present the GC is separated from the Kura Basin by the KFTB and piggyback Alazani Basin to the north, the Kura and Alazani Basins and KFTB formed a single continuous basin prior to the formation of the KFTB. Thus, we consider the stratigraphy exposed within the KFTB to largely represent deposition within this former, larger version of the Kura Basin. Results from deep boreholes drilled during the 1970s reveal that the stratigraphic fill of the central Kura Basin, which spans the Cenozoic, is deposited on top of Jurassic–Cretaceous volcanic rocks thought to be associated with the LC arc (Agabekov et al., 1976; Shikhalibeyli et al., 1988). Seismic velocities within the Kura Basin suggest that the Cenozoic sediment thicknesses exceed 10 km through much of the basin, with thickness likely exceeding 15 km at the western and eastern ends of the KFTB (Gunnels et al., 2020). The seismic velocity of the Mesozoic floor of the Kura Basin is consistent with it being either oceanic crust or highly attenuated continental crust (McKenzie et al., 2019; Gunnels et al., 2020), consistent with it representing a still-subducting portion of the former GC back-arc basin.

Depositional environments represented by strata exposed in the KFTB vary from shallow marine to terrestrial, and the strata are predominantly siliciclastic, with general coarsening-upward trends observed throughout most stratigraphic sections (e.g., Agustí et al., 2009; Forte et al., 2013, 2015a; Van Baak et al., 2013; Lazarev et al., 2019, 2021). Strata exposed in the KFTB were deposited in environments influenced by both the development of the GC and KFTB (e.g., Forte et al., 2013, 2015a) and large-magnitude (~1000 m) base-level changes of the Caspian Sea during the late Cenozoic (e.g., Popov et al., 2006; Forte and Cowgill, 2013; van Baak et al., 2017; Krijgsman et al., 2019; Lazarev et al., 2021). Variations in Caspian Sea base level along with potentially related intermittent connections between the Black and Caspian Seas along the southern range front of the GC (e.g., Popov et al., 2010; Forte and Cowgill, 2013; van der Boon et al., 2018; van Hinsbergen et al., 2019) are commonly considered a first-order driver of stratigraphy within the Kura Basin. As such, the stratigraphy of the Kura Basin and surrounding regions is classified in terms of regional stages associated with transgressions and regressions of the Caspian Sea and associated changes in biota (e.g., Zubakov and Borzenkova, 1990; Jones and Simmons, 1996).

We primarily place our provenance and resulting structural interpretations into the temporal context of the regional Caspian time scale as opposed to a global time scale. We do this for two reasons. First, this approach helps insulate our results from the disruption of future revisions to the Caspian time scale and its correlation with the global time scale. Establishing the absolute ages of the boundaries between Caspian stages, their correspondence with stages in the Paratethyan realm more broadly, and their correlation to the global time scale have all proven extremely controversial, with significant

revisions and/or shifts numerous times over the past several decades (see review in Krijgsman et al., 2019). Some of these changes were significant enough to shift a regional stage from one global stage to another. While concentrated magneto- and biostratigraphic work has significantly clarified the temporal extents of individual Caspian and related Paratethyan stages, disagreements remain, likely because (1) specific stage-bounding transgressive or regressive surfaces may have formed at different times in different Paratethyan basins, and/or (2) the individual stage-bounding surfaces may be time-transgressive within individual basins and their subbasins (e.g., Vasiliev et al., 2011; Van Baak et al., 2013, 2017, 2019; Forte et al., 2015a; Richards et al., 2018; Krijgsman et al., 2019; Lazarev et al., 2019, 2021). Because of the long-standing and ongoing problems with correlation of the regional stages to standard international geological epochs, nearly all prior international literature on the stratigraphy of this region has used regional stage names (e.g., Mamedov, 1973; Jones and Simmons, 1996; Vincent et al., 2010, 2013; Vasiliev et al., 2011, 2022; Van Baak et al., 2013, 2019; van Baak et al., 2016, 2017; Richards et al., 2018; Krijgsman et al., 2019; Lazarev et al., 2019, 2021; Palcu et al., 2019; Aghayeva et al., 2023). Thus, our second reason for using regional stage names is to follow this prior work.

The regional age divisions of primary relevance to the measured stratigraphic sections presented here are, from oldest to youngest: Meotian (base 7.65 Ma: Palcu et al., 2019), Pontian (base 6.12 Ma: van Baak et al., 2016), Productive Series (base 5.33 Ma: Aghayeva et al., 2023), Akchagylian (base 2.7 Ma: Krijgsman et al., 2019; base 2.95 Ma: Lazarev et al., 2021), Apsheronian (base 2.1 Ma: Lazarev et al., 2019), and Bakunian (base 0.8 Ma: Van Baak et al., 2013) (Fig. 2).

In the present study, we use Caspian time scales derived from magnetostratigraphy of several sections in the Apsheron Peninsula (Azerbaijan) and eastern Kura Basin (Krijgsman et al., 2019, and references therein) and the Kvabebi section (eastern Georgia) within the western KFTB (Fig. 1; Lazarev et al., 2021). The time scales are equivalent except for the age of the base of the Akchagylian regional stage (Fig. 2), which represents a transgressive surface reflecting an ~200 m base-level rise of the Caspian Sea following an extreme (~600 m below modern base level) regression during the preceding Productive Series time (e.g., Van Baak et al., 2017, 2019; Lazarev et al., 2021). In the composite time scale of Krijgsman et al. (2019), the Akchagylian spans from 2.7 to 2.1 Ma, whereas in the time scale of Lazarev et al. (2021), the Akchagylian is longer and spans from 2.95 to 2.1 Ma. Lacking a basis on which to choose between these two alternate time scales, we consider both when correlating the KFTB stratigraphy to the global time scale.

2.5 Prior Work on Foreland Provenance

Published studies of provenance in the foreland basins of the GC are limited. Existing results (Fig. 1) include isolated data from the Rioni Fold-Thrust Belt and related Cenozoic stratigraphy of the western GC (Vincent et al., 2013, 2014; Tye et al., 2020), data from the extreme western and eastern termini of the KFTB (Tye et al., 2020), and an expansive data set focused on exposures of Productive Series strata on the Apsheron Peninsula and in the eastern Kura Basin (Morton et al., 2003; Allen et al., 2006; Morton and Yaxley, 2007; Abdullayev et al., 2018). Those from the KFTB, Kura Basin, and Apsheron Peninsula are the most relevant here.

Results of heavy mineral analysis of Productive Series sandstones sampled on the Apsheron Peninsula are similar to those of the modern Volga River and rivers draining the eastern tip of the GC (Morton et al., 2003; Morton and Yaxley, 2007). This is consistent with the suggestion that during the extreme Caspian Sea low-stand coeval with Productive Series deposition, the paleo–Volga River mouth migrated southwards and entered the Caspian Sea near the modern-day position of the Apsheron Peninsula (e.g., Reynolds et al., 1998; Aliyeva, 2005; Kroonenberg et al., 2005; Vincent et al., 2010). Contrastingly, samples of Productive Series sandstones from the eastern margin of the Kura Basin, near the modern Kura River, contain a decidedly different heavy mineral assemblage, more consistent with samples from the modern Kura River taken near its outlet into the Caspian Sea (Morton et al., 2003; Morton and Yaxley, 2007). Generally, both modern Volga River samples and Apsheron Peninsula Productive Series rocks are characterized by more evolved, felsic heavy mineral assemblages when compared with samples from the Kura River or Kura Basin Productive Series rocks (Morton and Yaxley, 2007). In general, Morton et al. (2003) and Morton and Yaxley (2007) suggested that the presence of distinctive unstable species like clinopyroxene and calcic amphiboles in sediments is strongly suggestive of LC sourcing. However, Trexler et al. (2022) reported both of these phases in Jurassic volcanic and volcaniclastic rocks of the western GC in Georgia.

The heavy mineral results from the Apsheron Peninsula exposures of Productive Series sediments are largely reinforced by DZ age populations (Allen et al., 2006; Abdullayev et al., 2018), which are dominated by >900 Ma grains characteristic of the East European craton and rivers draining this terrane (Safonova et al., 2010; Wang et al., 2011; Tye et al., 2020) and which are encapsulated into the Eurasian interior DZ source defined by Tye et al. (2020). In contrast, DZ data from the extreme eastern GC and KFTB and western KFTB sampled from sedimentary strata ranging in age from Paleogene to Quaternary record mixtures of source terranes indicative of sourcing from either the GC or LC, with minimal input from the Eurasian interior (Tye et al., 2020). The majority of foreland samples from Tye et al. (2020) show affinity with one or more of the GC-associated sources, but some samples (e.g., their sample CF-1), even those extremely proximal to or within the modern GC (e.g., their sample EF-6), show affinity with the Transcaucasus basement and LC arc source. Where such provenance affinities are present, Tye et al. (2020) largely followed Morton et al. (2003) in considering these samples to reflect deposition of sediment delivered by a paleo–Kura River system, predominantly draining the LC, requiring a paleo–Kura River that was in part shifted northward and much closer to the GC range front relative to its modern position. Ultimately, with respect to the questions we consider here, the majority of existing DZ data

within the southeastern foreland (1) are derived from strata that are largely pre-tectonic with respect to both rapid exhumation of the GC and possible formation of the KFTB, and (2) also lack detailed stratigraphic or structural context (Tye et al., 2020), and as such, interpreting either unroofing patterns from the GC or details of the KFTB is challenging. We address these difficulties directly in this work. We begin by describing the stratigraphic context of the provenance samples we analyze (Section 3). Next, we introduce methods and results to establish correlations between the sampled measured sections and the regional time scale (Section 4). Finally, we present the methods and results of a diverse suite of provenance techniques (Section 5).

3. SAMPLE DESCRIPTION AND CONTEXT

The samples (Tables 1–3) that form the basis for this work mainly represent either samples of foreland basin deposits with unknown provenance sampled from five Mio-Pleistocene measured stratigraphic sections exposed within the KFTB (group A) or samples to characterize potential sources for these foreland basin deposits (group B). The sample types can be further divided into four groups. In group A, there is (1) volcanic ash from within the five measured stratigraphic sections or adjacent regions to enable stratigraphic correlations, and (2) sandstone with unknown provenance from the same stratigraphic sections; within group B, there are (3) modern stream sediments with catchments in adjacent mountains to characterize potential source areas for the KFTB sandstones, and (4) Mesozoic volcanic and volcaniclastic rocks of the Vandam zone now exposed within the GC to further clarify aspects of potential source areas for the KFTB sandstones. The majority of KFTB sandstone samples of unknown provenance were 2–4 kg of medium- to coarse-grained sandstone, whereas sample volume of ash horizons varied depending on thickness of the particular deposits.

3.1 Stratigraphic Context of KFTB Sandstone and Ash Samples

The five measured sections are at Vashlovani (eastern Georgia) and Sarica (western Azerbaijan; Forte et al., 2015a), Xocashen (western Azerbaijan; van Baak, 2010; Forte, 2012; Van Baak et al., 2013), Bozdagh (western Azerbaijan; Forte, 2012), and Goy (central Azerbaijan; Forte et al., 2013; Lazarev et al., 2019), and we refer readers to the source publications for detailed stratigraphic descriptions, logs, and ancillary data such as biostratigraphy (Figs. 1 and 2). To facilitate placing the 8 ash and 27 sandstone samples that come from these sections into stratigraphic context, we provide brief descriptions of the stratigraphy of each measured section in the Supplemental Material[1] (Section S1). Sandstone sample names indicate both the name of the measured section and stratigraphic height above base at which the sample was collected. Thus, sample V-15 is from the Vashlovani section, 15 m above the section base. Original (field) sample names are reported in Table 2. Summary geological maps showing the detailed locations and geological context of the sections are provided in the Supplemental Material (Figs. S1–S5).

To interpret the provenance records from the measured sections, it is necessary to correlate these measured sections to each other and the regional time scale. Forte (2012) proposed an initial set of correlations between the five measured sections considered here. However, that correlation lacked the detailed tephra glass geochemistry reported below (Section 4) and predated both new magnetostratigraphic work (Lazarev et al., 2019) and significant revisions to the regional time scale (e.g., van Baak et al., 2017; Krijgsman et al., 2019; Lazarev et al., 2021). In Section 4, we present an updated correlation based on these new data sources and prior magnetostratigraphy (e.g., Van Baak et al., 2013) and mapping (Abdullaev et al., 1957; Ali-Zade, 2005; Forte et al., 2015a).

TABLE 1. COORDINATES OF BASE AND TOP OF MEASURED SECTIONS

Section	Coordinates of base	Coordinates of top
Vashlovani	41.214°N, 46.360°E	41.237°N, 46.365°E
Sarica	41.052°N, 46.951°E	41.081°N, 46.953°E
Xocashen, section 1	40.991°N, 46.809°E	40.999°N, 46.953°E
Xocashen, section 2	41.017°N, 46.758°E	41.020°N, 46.758°E
Xocashen, section 3	40.981°N, 46.802°E	40.979°N, 46.800°E
Bozdagh	40.844°N, 46.735°E	40.874°N, 46.727°E
Goy	40.585°N, 48.198°E	40.591°N, 48.203°E

3.2 Context of Samples of Known Provenance

The 13 samples of modern stream sediment (Fig. 1) typically comprised >4 kg of medium- to coarse-grained modern river sand collected from the active channel at locations chosen to characterize particular source terranes within the adjacent mountain ranges. The source areas include the GC Paleozoic core (Enguri Rivers), Jurassic–Cretaceous Greater Caucasus Basin sediments (Aragvi, Zaqatala, Kumuk, Kish, and Damiraparan Rivers), Dzirula Massif (Kvirila River), Adjara-Trialet and western LC (Mtkvari River, which is the upstream equivalent of the Kura River), LC arc (Tovuz, Shamkir, and Zayam Rivers), and mixtures thereof (Kura and Rioni Rivers). Where applicable, samples were collected upstream of major dams (e.g., Enguri). For these samples, we present bulk geochemistry as described in the methods section below (section 5.1). DZ U-Pb age populations for four of these rivers (Enguri, Kumuk, Mtkvari, and Tovuz) were presented by Cowgill et al. (2016). For the 11 volcaniclastic samples from the Vandam, we analyzed bulk geochemistry for all and sandstone petrography for a subset (6 samples). A DZ population was published for one of these samples (AB0862 = SE-GC) by Cowgill et al. (2016).

[1]Supplemental Material. Includes additional analyses and methods, figures, and tables. Please visit https://doi.org/10.1130/GEOS.S.27139257 to view the supplemental material. Contact editing@geosociety.org with questions.

TABLE 2. COORDINATES OF PROVENANCE SAMPLES INCLUDING ORIGINAL (FIELD) SAMPLE NUMBERS, SAMPLE NAMES USED IN THE TEXT, AND ANALYSES PERFORMED

Original sample number	Sample name	Latitude (°N)	Longitude (°E)	Analyses	Analyses in other publications
Kura Basin					
091025-4	B-875	40.87	46.73	PC, G, DZ	
091025-1	B-530	40.86	46.73	PC, G	
091007-6	B-280	40.85	46.73	PC, G, DZ	
091007-3	B-180	40.85	46.74	PC, G	
090924-4	G-1620	40.73	47.79	PC, G	
090923-1A	G-990	40.71	47.77	PC, G	
090922-2A	G-680	40.71	47.77	PC, G	
090921-2	G-200	40.70	47.77	G, DZ	
090921-1	G-175	40.70	47.77	PC	
090911-2	S-1735	41.08	49.95	PC, G, DZ	
090910-2	S-1100	41.08	46.95	PC, G	
090909-3B	S-865	41.07	46.95	PC, G	
090909-1	S-610	41.07	46.95	PC, G	
090907-1	S-360	41.06	46.95	PC, G	
090906-4	S-210	41.06	46.95	PC, G, DZ	
090906-2	S-90	41.05	46.95	PC, G	
091001-1	X-605	41.00	46.82	PC, G	
091002-3	X-410	41.00	46.81	G	
090930-3	X-330	41.00	46.81	PC, G	
090929-1	X-3	40.99	46.81	PC, G	
091011-4	XX-140	40.98	46.80	PC, G	
101311-10	V-1448	41.237	46.365	PC, G	
101311-7	V-1240	41.234	46.363	PC, G, DZ	
101311-4	V-1006	41.231	46.361	PC, G	
101311-3	V-914	41.231	46.359	PC, G	
101311-2	V-602	41.229	46.354	PC, G	
101211-2	V-212	41.218	46.359	PC, G	
101211-1	V-15	41.216	46.360	PC, G, DZ	
Modern sediment					
080902-1B	Kish	41.229	47.166	G	
080902-2B	Kumuk	41.410	46.931	G	DZ (Cowgill et al., 2016)
080908-3A	Kura	41.248	45.442	G	
090916-1B	Damiraparan	41.021	47.889	G	
091009-1B	Tovuz	40.985	45.642	G	DZ (Cowgill et al., 2016)
091009-2B	Shamkir	40.814	40.814	G	
091009-3B	Zayam	40.923	45.833	G	
AB0885	Zaqatala	41.717	46.596	G	
100511-6	Rioni	42.248	42.702	G	
100411-2	Enguri	42.931	42.120	G	DZ (Cowgill et al., 2016)
101011-12	Aragvi	42.176	44.697	G	
100511-8	Mtkvari	42.021	43.769	G	DZ (Cowgill et al., 2016)
100511-7	Kvirila	42.202	42.845	G	
Greater Caucasus bedrock					
AB0856		40.820	48.307	G	
AB0862	SE-GC	40.837	48.335	PC, G	DZ (Cowgill et al., 2016)
AB0863		40.913	48.069	G	
AB0864		40.927	48.068	G	
AB0867		40.840	48.367	G	
AB0895		40.796	48.319	G	
AB0857		40.819	48.308	PC, G	
AB0855		40.838	48.340	G	
AB0865		40.927	48.068	G	
AB0866		40.841	48.346	G	
AZ0603		40.796	48.319	G	

Notes: PC—petrography; G—bulk geochemistry; DZ—detrital zircon U-Pb geochronology.

4. STRATIGRAPHIC CORRELATIONS

The source publications for each of the five measured sections provide existing age estimates (see Section S1 and Figs. S1–S5, footnote 1). In this section, we use major element chemistry of glass shards isolated from ash horizons (Fig. S6; Table 3) to refine stratigraphic correlations between these sections and thus their ages.

4.1 Analytical Methods for Major Element Geochemistry of Volcanic Glass

Major element fingerprinting of volcanic glass shards within tephra deposits is a useful stratigraphic correlation tool (e.g., Lowe, 2011; Lowe et al., 2017). For this study, geochemical analyses were conducted on volcanic glass shards (125–250 µm) manually separated from eight tephra samples collected from locations throughout Georgia and Azerbaijan; an additional ninth sample (B-A) from the Bozdagh section yielded no usable glass shards. Five of the samples (B-B from the Bozdagh section; X-2A, X-3A, and X-3B from the Xocashen section; G-A from the Goy section) came from measured sections described in section 3.1, whereas the other three (TG, WQ-A, and WQ-B) were collected in similarly aged units in the eastern KFTB mapped by Forte et al. (2013), which we include largely for future work in this region. Sample locations are in Table 3. All tephra samples were separated and cleaned following common tephra preparation procedures (e.g., Roman et al., 2008). Specifically, samples were first wet sieved at Arizona State University (ASU; Tempe, Arizona, USA) using 841–420–250–177 micron sieves. The 420–250 micron fractions were washed with 5% nitric acid to remove any carbonates, rinsed with deionized water, and then washed with 5% hydrofluoric acid one to three times in 2 min ultrasonic baths to remove clay adhering to the glass shards. Glass shards were then mounted in epoxy rounds, polished, and carbon coated for analysis in an electron microprobe.

Individual glass shards were analyzed for major element oxide abundances (SiO_2, Al_2O_3, K_2O, Na_2O, CaO, MgO, MnO, Fe_2O_3, and TiO_2) using a JEOL JXA-8530F electron probe microanalyzer with JEOL software in the John M. Cowley Center for High Resolution Electron Microscopy at ASU. Using wavelength-dispersive spectrometry, the instrument was operated at 15 kV, with a 10 nA beam current and a 15 µm defocused beam to minimize alkali loss (Froggatt, 1992; Lowe, 2011). All data were adjusted using atomic number (Z), absorption (A), and fluorescence (F) corrections. If possible, 20 or more glass shards were analyzed for each sample. To assess analytical precision, the Lipari glass INTAV standard (Kuehn et al., 2011) and the Los Posos Rhyolite (RHY5) in-lab standard were run at the start and end of an analysis session and after every 40–60 unknown analyses.

Major element analytical results are reported as un-normalized data averages with 1σ standard deviation error (Table 3). Brief descriptions of the glass and crystals (if present) are also provided in Table 3. Individual shard analyses are reported in the Supplemental Material (Table S1). Individual analyses with totals <90% or with otherwise anomalous values (e.g., SiO_2 >90%) were not included in the averages or later statistics but are still reported in the Supplemental Material. Low totals can be a result of alteration (potential leaching) or analytical issues and are not viable for considering stratigraphic correlations.

4.2 Statistical Methods for Major Element Geochemistry of Volcanic Glass

In our treatment of the major element data for the volcanic glasses, we primarily follow recommendations from Lowe et al. (2017). Specifically, we explore potential correlations with plots of log ratios of various major element pairs and select one set (CaO/Al_2O_3 and TiO_2/Fe_2O_3) that provides meaningful separation of different tephra beds or components. Prior to plotting, rounded zeroes (quantities measured but present in amounts below the detection limit) were replaced by a nonparametric imputation as described by Martín-Fernández et al. (2003) using the CoDaPack software package (Comas and Thió-Henestrosa, 2011). We compare this with the results of a principal component analysis (PCA), a technique for reducing dimensionality (Krzanowski, 2000), applied to all of the major oxides. Prior to PCA, the oxide concentrations were normalized using a standard scaler so that data were normally distributed with a zero mean and unit variance (Lowe, 2011; Lowe et al., 2017).

We also estimated the similarity of the tephra samples via a modified Euclidean distance measure, D^2, defined by Perkins et al. (1995) as:

$$D^2 = \sum_{k=1}^{n}\left[\frac{\left(x_{k1} - x_{k2}\right)^2}{2\sigma_k^2}\right], \quad (1)$$

where x_{k1} is the concentration of element x_k in the glass of tephra 1, x_{k2} is the concentration of element x_k in the glass of tephra 2, σ_k is the analytical precision of element x_k, and n is the number of elements used in the comparison. We refer to this modified Euclidean distance measure as the "Perkins statistical distance." Here we select five of the major oxides, CaO, Fe_2O_3, MgO, MnO, and TiO_2, for this distance calculation. We follow Perkins et al. (1995) and do not include Al_2O_3 and SiO_2 in this calculation because they do not show much variation for the majority of samples and could bias the distance measures. Similarly, we exclude Na_2O and K_2O from the calculation because the concentrations of these elements are sensitive to post-depositional hydration of glass shards. Calculated D^2 measures have a chi-squared distribution, and thus with five elements (five degrees of freedom), two tephras can be considered statistically different at the 95% and 99% confidence levels if D^2 exceeds 11.1 and 15.1, respectively. Correspondingly, D^2 less than these critical values suggests that the respective tephras may be correlative. We report the D^2 values in Table 4.

4.3 Ash Correlations

Geochemically, six of the eight analyzed ashes contain exclusively rhyolitic shards (Fig. S7). The other two samples (B-B and X-3A) both have two

TABLE 3. COORDINATES OF ASH SAMPLES AND MEANS AND STANDARD DEVIATIONS OF MAJOR ELEMENTS OF THE ASH SHARDS EXTRACTED FROM THE ASH SAMPLES

Original sample number	Latitude (°N)	Longitude (°E)	Section (height above base)	Sample name used in text	Glass content (%)	Crystal content (%)	Glass description	Crystals description	Lithics description	No. of shards analyzed	K_2O (wt%)	±	CaO (wt%)	±	SiO_2 (wt%)	±	Al_2O_3 (wt%)	±	Na_2O (wt%)	±	MgO (wt%)	±	TiO_2 (wt%)	±	Fe_2O_3 (wt%)	±	MnO (wt%)	±
80904-3A	40.865	46.726	Bozdagh (740 m)	B-A	0	N/A	N/A	N/A	N/A	0	N/A	N/A	N/A	N/A	N/A	N/A	N/A	N/A	N/A	N/A	N/A	N/A	N/A	N/A	N/A	N/A	N/A	N/A
80904-4B	40.867	46.724	Bozdagh (775 m)	B-B, mode 1	90–95	10–5	Mostly altered pumice or glass, few frothy clear glass shards	Biotites, feldspar		19	4.006	0.194	0.888	0.024	76.450	0.128	13.581	0.091	4.189	0.133	0.072	0.013	0.083	0.021	0.684	0.025	0.046	0.029
80904-4B	40.867	46.724	Bozdagh (775 m)	B-B, mode 2	N/A	N/A	N/A	N/A	N/A	7	0.785	0.071	4.917	0.402	62.064	0.530	23.745	0.377	8.319	0.254	0.000	0.000	0.009	0.012	0.155	0.021	0.007	0.008
90924-8C	40.730	47.790	Goy (1720 m)	G-A	80–90	10–20	Frothy and elongate thin white to clear glass, some partially altered	Biotites, feldspar		30	4.323	0.203	0.899	0.056	76.388	0.444	13.602	0.119	3.876	0.427	0.076	0.019	0.079	0.020	0.695	0.055	0.061	0.024
91013-1A	40.634	47.904	N/A	TG	90	10	Thick clear to white, platy and block, bubble walled, few elongate, few frothy pumice	Very few: augite	Felsic to mafic grains, glass aggregates	25	4.480	0.069	0.613	0.026	76.878	0.126	13.029	0.076	3.903	0.112	0.109	0.011	0.149	0.015	0.797	0.020	0.043	0.027
91015-1	40.624	47.900	N/A	WQ-A	60–55	40–45	Platy to bubble walled, frothy to reticulite, elongate	Olivine to augite, quartz,	Felsic grains	25	4.621	0.118	0.472	0.028	76.089	0.175	13.423	0.094	4.066	0.144	0.018	0.011	0.072	0.022	1.210	0.055	0.030	0.024
91015-2	40.624	47.900	N/A	WQ-B	90–95	10–5	Frothy, bubble-walled or elongate white to clear glass	Very few: olivine	Felsic grains	30	4.612	0.097	0.481	0.029	76.076	0.117	13.444	0.118	4.041	0.088	0.018	0.013	0.061	0.016	1.240	0.029	0.027	0.024
91002-1A	41.000	46.820	Xocashen 2 (465m)	X-2A	95	5	Reticulite to frothy thin bubble or elongate, bubble-walled clear shards, few platy	None	Felsic grains	25	4.461	0.124	0.605	0.026	76.834	0.130	13.080	0.093	3.917	0.140	0.104	0.015	0.149	0.019	0.812	0.025	0.039	0.022
80901-2A	41.017	46.758	Xocashen 3 (5m)	X-3A, mode 1	85–90	10–15	Frothy and elongate thin white to clear glass	Biotites, feldspar, quartz, augite?	Few felsic grains	6	4.228	0.154	0.939	0.058	76.128	0.297	13.710	0.177	3.984	0.077	0.099	0.019	0.092	0.023	0.761	0.085	0.058	0.034
80901-2A	41.017	46.758	Xocashen 3 (5m)	X-3A, mode 2	N/A	N/A	N/A	N/A	N/A	1	0.448	0.000	7.266	0.000	59.042	0.000	25.948	0.000	7.039	0.000	0.000	0.000	0.000	0.000	0.220	0.000	0.036	0.000
91003-1A	41.020	46.758	Xocashen 3 (110 m)	X-3B	90–95	10–5	Thick clear to white, platy and block tobubble walled, some elongate, some frothy pumice	Very few: olivine, augite, feldspar	Felsic grains	25	4.449	0.094	0.600	0.024	76.886	0.178	13.040	0.103	3.901	0.100	0.110	0.013	0.148	0.029	0.820	0.024	0.046	0.026

Notes: For all columns but "Section," "N/A" implies there were insufficient crystals or glass shards to describe fully. For "Section," it means that these samples were taken from outside a measured section.

TABLE 4. PERKINS STATISTICAL DISTANCE BETWEEN ASH SAMPLES FROM WITHIN MEASURED SECTIONS

Sample name	B-B, mode 1	B-B, mode 2	G-A	TG	WQ-A	WQ-B	X-2A	X-3A, mode 1	X-3A, mode 2	X-3B
B-B, mode 1	0.00									
B-B, mode 2	8293.02	0.00								
G-A	**0.21**	8254.37	0.00							
TG	45.24	9494.17	47.67	0.00						
WQ-A	113.47	10,130.32	118.52	44.81	0.00					
WQ-B	111.85	10,091.80	116.75	46.08	0.17	0.00				
X-2A	46.77	9526.30	49.42	**0.12**	40.58	41.85	0.00			
X-3A, mode 1	**3.57**	8105.34	**2.48**	56.33	140.80	138.50	58.87	0.00		
X-3A, mode 2	20,730.70	2809.63	20,667.43	22,590.55	23,560.51	23,499.47	22,641.10	20,421.32	0.00	
X-3B	49.43	9552.96	51.89	**0.13**	42.33	43.62	**0.14**	60.79	22,679.74	0.00

Notes: Calculated using CaO, Fe_2O_3, TiO_2, MgO, and MnO; chi-squared distribution; degrees of freedom = 5 (5 elements); 95% confidence level = 11.1; 99% confidence level = 15.1. Bold values indicate statistical distance values that suggest a statistically significant relation between those samples.

compositional groups, with rhyolite shards (mode 1) most abundant and a secondary population (mode 2) that is somewhat geochemically diverse and distinctly lower in silica, having trachyte to trachyandesite compositions (Fig. S7). Bi-plots of log ratios and PCA reveal four broad tephra groupings, one of which includes the mode 2 shards (Fig. 3). Key observations from the bi-plots and PCA for correlating the measured sections are: (1) tephras X-3B and X-2A within the two younger Xocashen sections (plus TG at Goy; see next paragraph) are similar and likely indicate a single eruptive source, consistent with other stratigraphic correlations based on the Apsheronian-Bakunian boundary in both sections (van Baak, 2010; Van Baak et al., 2013); and (2) tephras X-3A in the Xocashen section, B-B in the Bozdagh section, and G-A in the Goy section are similar and likely represent a second eruptive source. Note that the pairs of mode 1 and mode 2 shards in X-3A and B-B also appear similar to each other, although the mode 2 shards have significant scatter (Fig. 3; Fig. S7). Although mode 2 shards are absent from the sample of G-A tephra, we did observe in the G-A ash a distinctively more mafic interval that may represent this mode but that we unfortunately did not sample (Fig. S7).

Outside of the measured sections, tephras WQ-A and WQ-B were both sampled from a single outcrop of unit G3 (cf. Fig. 2) in the Goy area (Forte et al., 2013), with WQ-A stratigraphically below WQ-B by ~40 cm. These two samples group with each other (Fig. 3) but are distinct from all other samples analyzed here, indicating they likely represent tephras from a third, distinct eruptive source. Tephra TG was collected from a thrust-bounded slice of unit 2G of Forte et al. (2013) in the Goy area and was assumed by Forte et al. (2013) to correlate with tephra G-A in the Goy section. However, the new geochemical data indicate TG correlates with tephras X-3B and X-2A in the Xocashen section, not with G-A.

For all the tephras, the correlations derived from the bi-plots are largely identical to those interpreted from Perkins statistical distance (Table 4). In detail, the Perkins statistical distance measure does not suggest that the more mafic mode 2 groups of tephras X-3A and B-B are correlative, but this likely reflects the relatively large variability in the geochemistry and small number of shard analyses, with only one shard from X-3A classified as mode 2.

4.4 Correlations

The new ash geochemistry establishes new ties between the Xocashen, Bozdagh, and Goy sections. Additionally, magnetostratigraphy in the Xocashen (Van Baak et al., 2013) and Goy (Lazarev et al., 2019) sections strengthens the correlations between these two sections. Combining these data with prior age calls from geological mapping (Abdullaev et al., 1957; Ali-Zade, 2005; Forte, 2012) and biostratigraphy (Forte et al., 2013, 2015a; Van Baak et al., 2013; Lazarev et al., 2019) allows us to correlate the different sections both to each other and to the regional time scale (Fig. 2). A summary of the key data sets informing our correlations are: (1) magneto- and biostratigraphy, which allow for direct correlation between the Xocashen and Goy sections and with both the regional time scale and global paleomagnetic time scale (van Baak, 2010; Van Baak et al., 2013; Lazarev et al., 2019); (2) new ash geochemistry, which allows for direct correlation between portions of the Xocashen, Bozdagh, and Goy sections (Fig. 3); (3) maximum depositional ages (MDAs) from U-Pb ages of DZs in the Sarica and Vashlovani sections, which allow connection between the global absolute time scale and the regional time scale (Forte et al., 2015a); and (4) mixtures of biostratigraphy, lithostratigraphy, depositional environment interpretations derived thereof, and inferred relations to Capsian stages, which allow for further correlation between stratigraphy in all sections and the regional time scale (e.g., Abdullaev et al., 1957; Ali-Zade, 2005; Forte, 2012; Forte et al., 2013, 2015a; Van Baak et al., 2013; Lazarev et al., 2019). Below we consider specific correlations between units within the measured sections and their respective correlations to the Caspian regional time scale.

Based on these data, the Meotian–Pontian stages are represented exclusively by Vashlovani unit V1, which does not correlate to any portions of the

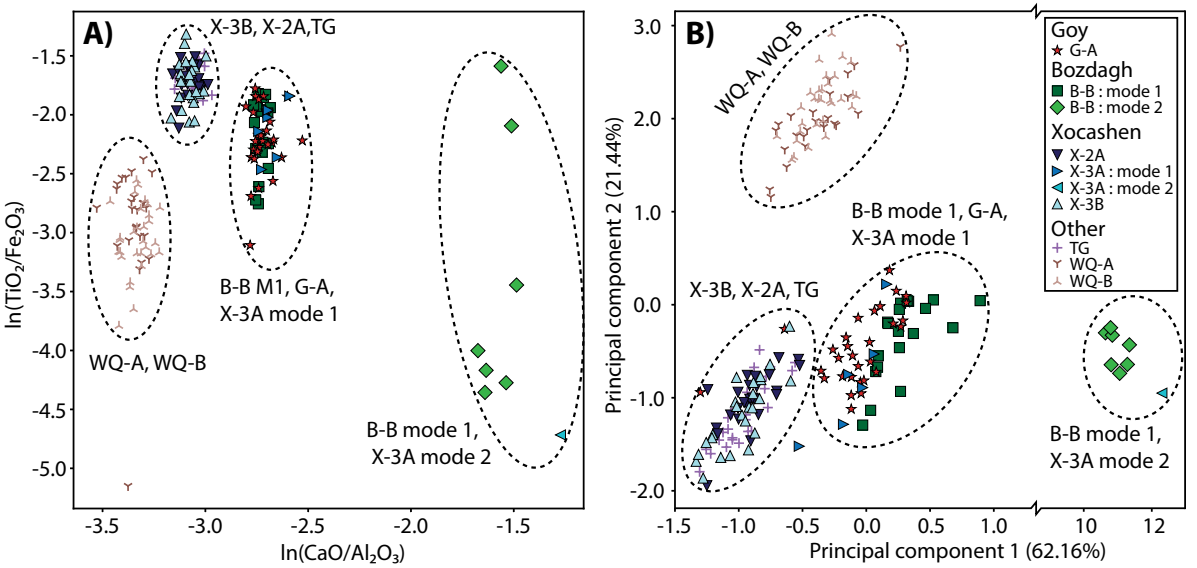

Figure 3. Plots of tephra shard geochemistry. Samples from measured sections are indicated in the explanation and indicated at the stratigraphic positions shown on Figure 2. Three ashes marked "Other" come from outside the measured sections and are included for potential future work in this region and are not directly relevant to the main points of this effort. (A) Plot of natural log of element ratios highlighting separation of different ash populations and emphasizing the existence of two modes (mode 1, mode 2) within ashes X-3A and B-B. (B) Plot of principal component analysis (PCA) of ash shard geochemistry suggesting similar groupings as log ratios. X axis shows first principal component and Y axis shows second principal components. Percentage of variance explained by each principal components are shown on axes. Notice significant break in *x*-axis, reflecting extreme difference between all other samples and mode 2 shards in samples B-B and X-3A.

other sections. The Productive Series stage is represented by Vashlovani unit V2 and Sarica unit S1. Note that within the Sarica section, Forte et al. (2015a) previously used a small subpopulation of zircons from sample S-210 near the top of unit S1 to determine an MDA of 2.5 ± 0.24 Ma. This MDA is consistent within uncertainty with deposition during Productive Series time if the age of the Productive Series–Akchagylian boundary is at 2.7 Ma (as reported by Krijgsman et al., 2019), but it is inconsistent if the boundary is at 2.95 Ma (as reported by Lazarev et al., 2021). Although resolving this question is beyond the scope of the present work, this discrepancy does indicate that the exact position of the Productive Series–Akchagylian boundary in the Sarica section may be unclear. For our purposes, we assume that the entirety of unit S1 is within the Productive Series to be consistent with Forte et al. (2015a).

The Akchagylian period is represented by the basal portion of unit V3 in the Vashlovani section, unit S2 in the Sarica section, unit X1 in section Xocashen-1, and unit G1 in the Goy section, which all correlate to each other based on prior results from Forte et al. (2013, 2015a). Forte et al. (2015a) previously reported a relatively large population of young zircon grains in sample V-1240 from Vashlovani unit V3, which they used to establish an MDA of 2.66 ± 0.046 Ma. At the time of publication of Forte et al. (2015a), the MDA corresponded to a long hiatus between the Akchagylian and Apsheronian stages (Van Baak et al., 2013), making it unclear if the sample was deposited during the Akchagylian or the Apsheronian. Subsequent work has refined the age of the Akchagylian-Apsheronian boundary to 2.1 Ma (e.g., Krijgsman et al., 2019; Lazarev et al., 2021). Thus, the MDA from V-1240 is now consistent with deposition during either early or mid-Akchagylian time, depending on which time scale is chosen.

The Apsheronian period is represented by the upper portion of Vashlovani unit V3; Sarica units S3–S5; Xocashen-2 unit X2; Bozdagh units B1–B3; and Goy units G2-A, G2-B, G2-C, and G3, as well as one tephra horizon represented by samples X-3B, X-2A, and TG and another represented by samples X-3A, B-B, and G-A. Our interpretation of unit V3 follows prior mapping from Abdullaev et al. (1957), which places the upper portion of this unit within the Apsheronian. However, V3 lacks a clear lithostratigraphic break, so the location of the Akchagylian-Apsheronian boundary within this unit is uncertain. At first, the correlation between Xocashen ash X-3A and Goy ash G-A may seem at odds with prior magnetostratigraphic results in these two sections (Van Baak et al., 2013; Lazarev et al., 2019) but, as described in detail in the Supplemental Material (see Section S1.6), are reconcilable if the different sedimentation rates of these two sections are considered.

TABLE 5. LINEAR DISCRIMINANT ANALYSIS (LDA) VALUES FOR SOURCE SAMPLES AND RESULTANT SOURCE DESIGNATIONS

Sample	LDA-1				LDA-2			LDA-3			
	LD1	LD2	LD3	Class	LD1	LD2	Class	LD1	LD2	LD3	Class
Kish	–23.063162	3.33069266	–3.064545	GC interior, low Si	–50.947494	1.4794405	GC interior	–50.221726	1.6883881	–0.0284059	GC interior
Kumuk	–35.05741	0.62102729	3.3206759	GC interior, high Si	–52.280879	0.5750608	GC interior	–51.559711	0.69945294	–0.6218547	GC interior
Kura	–22.031047	1.68564729	–2.1831491	GC interior, low Si	–16.632678	–2.9719189	GC interior	–15.958672	–4.0654237	–9.2204343	MB Kura River
Damiraparan	–30.566317	–0.0285815	2.4605471	GC interior, high Si	–50.085162	0.3068498	GC interior	–49.356217	0.65911577	1.14103957	GC interior
Tovuz	9.3779978	–4.5153659	–0.5598346	LC-Vandam, high Si	20.3594851	–4.2910357	LC-Vandam, high Si	21.080462	–4.0612327	1.25477066	LC-Vandam, high Si
Shamkir	29.2129268	2.95054538	1.1679753	LC-Vandam, low Si	40.3235595	4.3651333	LC-Vandam, low Si	41.058883	4.55706432	0.60715349	LC-Vandam, low Si
Zayam	8.1088383	–3.2591202	0.8992025	LC-Vandam, high Si	21.8464605	–2.9518209	LC-Vandam, high Si	22.563642	–2.8945045	–0.1215405	LC-Vandam, high Si
Zaqatala	–33.02755	0.00558985	1.786583	GC interior, high Si	–53.780264	–0.1517126	GC interior	–53.054617	0.13547621	0.64075484	GC interior
Rioni	–24.391135	1.51274194	–2.2130052	GC interior, low Si	–49.855676	0.1580155	GC interior	–49.128914	0.45552389	0.73938233	GC interior
Enguri	–32.625926	1.08908896	3.7057866	GC interior, high Si	–51.151257	1.5415121	GC interior	–50.424392	1.77870396	0.17884576	GC interior
Aragvi	–22.280889	2.04117229	–2.2177883	GC interior, low Si	–52.554831	1.31904	GC interior	–51.818021	1.84886524	2.3905515	GC interior
Mtkvari	29.2012084	5.4044959	–0.2875503	LC-Vandam, low Si	40.3585779	5.4186608	LC-Vandam, low Si	41.083318	5.26299685	–2.0889944	LC-Vandam, low Si
Kvirila	–23.016203	4.08993295	–2.6938416	GC interior, low Si	–51.365373	2.3261271	GC interior	–50.63896	2.51392707	–0.2483727	GC interior
AB0856	29.2240572	4.61133386	0.9905134	LC-Vandam, low Si	40.4647963	5.5223571	LC-Vandam, low Si	41.195753	5.53654651	–0.8109596	LC-Vandam, low Si
AB0862	10.119679	–4.5099671	1.9946777	LC-Vandam, high Si	21.1261218	–2.7808684	LC-Vandam, high Si	21.85727	–2.3374553	2.77779325	LC-Vandam, high Si
AB0863	61.4375046	–7.0886288	22.0786459	LC-Vandam, low Si	102.233462	8.2769125	LC-Vandam, low Si	103.052043	10.5252994	16.5395032	LC-Vandam, low Si
AB0864	28.8423465	2.1253214	0.8970055	LC-Vandam, low Si	41.1560628	3.4074289	LC-Vandam, low Si	41.889528	3.59096023	0.61544721	LC-Vandam, low Si
AB0867	8.4712544	–5.1862763	–1.6599299	LC-Vandam, high Si	21.3499078	–5.7291105	LC-Vandam, high Si	22.063781	–5.6329099	0.35006954	LC-Vandam, high Si
AB0895	8.598102	–5.6832945	–0.8190505	LC-Vandam, high Si	21.1926176	–5.5920641	LC-Vandam, high Si	21.911272	–5.3675477	1.30921103	LC-Vandam, high Si
AB0857	28.7514625	3.10875977	1.381953	LC-Vandam, low Si	41.7273111	4.3475972	LC-Vandam, low Si	42.459179	4.44083213	–0.1229622	LC-Vandam, low Si
AB0855	8.0902093	–4.3392068	–2.0155138	LC-Vandam, high Si	20.6017773	–5.2771349	LC-Vandam, high Si	21.312765	–5.2822453	–0.4532297	LC-Vandam, high Si
AB0865	30.4741953	4.84357687	–0.4259814	LC-Vandam, low Si	38.7453729	5.368203	LC-Vandam, low Si	39.477505	5.42556705	–0.4924687	LC-Vandam, low Si
AB0866	9.2008888	–5.7118129	–1.0397618	LC-Vandam, high Si	20.9936193	–5.5860518	LC-Vandam, high Si	21.713695	–5.3215057	1.60928034	LC-Vandam, high Si
AZ0603	8.3864735	–4.1863012	0.5750314	LC-Vandam, high Si	21.7752643	–3.7756271	LC-Vandam, high Si	22.494177	–3.6305956	0.59492306	LC-Vandam, high Si

Notes: MB—mid-basin; GC and LC are defined as abbreviations for the Greater and Lesser Caucasus; Class implies into which group from the training dataset that samples is classified; LDA—linear discriminant analysis.

The Bakunian period is represented by Xocashen-2 units XB and X3 and is not directly represented in other sections. Because the upper bounds of the Apsheronian in both the Sarica and Bozdagh sections are not well constrained, the upper parts of these sections may be of Bakunian age, but we do not implement such a correlation here because we have no direct evidence.

5. SEDIMENT PROVENANCE

We apply a variety of methods to determine the provenance of samples taken from the measured sections, including sandstone petrography, bulk sediment and/or rock major and trace element geochemistry, and DZ geochronology (Table 2). We analyze each data type using several different statistical and/or visualization approaches, resulting in a varied and multifaceted study. Ultimately, many of these statistical and/or visualization approaches provide similar conclusions, so for the sake of clarity, we present in the main text a streamlined view of the methods, results, and statistical and visualization approaches, with the additional information provided in the Supplemental Material (see footnote 1) for completeness.

In the following subsections, we consider each type of provenance data separately, first presenting the relevant analytical methods, then the statistical treatments and visualizations we apply to the data, and finally the results and our interpretations. For the geochemistry and petrography data, we define new provenance sources here. In contrast, for the DZ geochronology data, we use source characterizations previously defined by Tye et al. (2020). Importantly, the two different sets of provenance sources are not the same because of differences in sensitivity between the methods. As we elaborate in the discussion (section 6.1), exploring these differences in sensitivity explains why the different methods appear to record different apparent histories and sources and allows us to leverage those differences to gain deeper insight into the evolution of the KFTB.

5.1 Sandstone Major and Trace Element Geochemistry and Petrography

Both sandstone petrography (e.g., Dickinson, 1970; Dickinson and Suczek, 1979; Ingersoll et al., 1984; Ingersoll, 1990) and major and trace element geochemistry (e.g., Bonjour and Dabard, 1991; Totten et al., 2000; Von Eynatten, 2003; von Eynatten et al., 2003) are well established methods for determining

sediment provenance. It has been suggested that major and trace element geochemistry of bulk sediments provides a means of discerning provenance that is less biased by effects of chemical alteration and weathering than traditional petrographic approaches (e.g., Dickinson, 1970) and by effects of hydraulic sorting that may influence heavy mineral data and related geochronologic techniques (e.g., von Eynatten et al., 2003; Pe-Piper et al., 2008). However, as applied to the Kura Basin sandstones, the results and implications of bulk geochemistry and sandstone petrography are effectively the same (see Section 5.1.6). As such, we focus here on the use of trace elements to characterize provenance, reporting the methods, results, and discussion of our sandstone petrography in the Supplemental Material (Section S2.1 and Figs. S8 and S9).

5.1.1 Analytical Methods for Major and Trace Element Analysis

We obtain major and trace element geochemical analyses for 26 of the total 27 sandstone samples from the KFTB (unknown provenance), 13 samples of modern river sediment (known provenance), and 11 samples of Mesozoic Vandam volcaniclastic rocks (known provenance), complete results for which are in Table S4. For all but one sample (G-200), these were the same sample materials analyzed for sandstone petrography (see Section S2.1). We obtained interior sections of each sample by removing weathering rinds and then sent ~200 g of each sample to Activation Laboratories Ltd. (Ancaster, Ontario, California) where they were crushed and analyzed according to the laboratory's Code 4Lithoresearch and Code 4B1 protocols, which are similar to those used by Pe-Piper et al. (2008) and yield concentrations for 44 different elements in total (Table S4). In particular, major and trace element concentrations were measured using lithium metaborate/tetraborate fusion inductively coupled plasma (ICP) analysis and ICP-mass spectrometry (MS) analysis, respectively.

5.1.2 Statistical Methods for Major and Trace Element Analysis

Numerous methodologies have been developed to use the bulk rock major and/or trace element geochemistry analyses of siliciclastic sediments to establish tectonic setting (e.g., Bhatia, 1983; Bhatia and Crook, 1986; Roser and Korsch, 1986; Herron, 1988; Totten et al., 2000), provenance (e.g., Roser and Korsch, 1988; Bonjour and Dabard, 1991; Pe-Piper et al., 2008), or degree of chemical weathering (e.g., Nesbitt and Young, 1982; Harnois, 1988; Fedo et al., 1995). In this work, we consider all three applications of the geochemical data, but in the main text, we focus primarily on the use of trace element geochemistry with multivariate statistical techniques to characterize potential source terranes and then classify samples of unknown provenance within that context. In the Supplemental Material (Section S2.2), we provide additional methods and results related to both basic tectonic discrimination (Figs. S10 and S11) and chemical weathering indices (Fig. S12) that largely reinforce points that are made clearest with the multivariate statistical treatment.

Importantly, before applying multivariate statistical techniques, it is necessary to transform raw compositional data into a form that does not violate the underlying assumptions of those methods, specifically that input data follows a multivariate normal distribution (Aitchison, 1986; von Eynatten et al., 2003). Several different transformations have been proposed to convert compositional data into a form more appropriate for use in multivariate statistics, and from these, we elect to use the isometric log ratio (ILR) because it converts compositional data into values suitable for any standard multivariate statistical approach (e.g., Egozcue et al., 2003; Egozcue and Pawlowsky-Glahn, 2005; Pawlowsky-Glahn and Egozcue, 2006). We provide an expanded discussion of alternate transforms in the Supplemental Material (Section S2.2.1).

For the multivariate statistics, we test two different suites of elements. The first is a suite of 17 trace elements (Sc, V, Cr, Co, Ni, Rb, Sr, Y, Zr, Nb, La, Gd, Yb, Hf, Ta, Th, and U) and one oxide (TiO_2), which is suggested by Pe-Piper et al. (2008) to provide a good discrimination of source geochemistry in detrital samples. The second suite is a set of 10 major elements (SiO_2, Al_2O_3, Fe_2O_3(T), MnO, MgO, CaO, Na_2O, K_2O, TiO_2, and P_2O_5 and excluding loss on ignition [LOI]), which is another suite used by Pe-Piper et al. (2008). For both suites, we replace rounded zeroes in the same manner as for the glass geochemistry using the CoDaPack software, which we also use to transform the compositions into ILRs suitable for multivariate analyses (Table S5). Because our main goal is to understand the relations between the samples rather than the relations between the measured components, the ILR is suitable even though it is not possible to relate the ILR coordinates to specific measured values (e.g., Egozcue et al., 2003). For this reason, we do not report loadings for the various multivariate analyses performed because they do not provide useful information.

To characterize variability and evaluate potential populations within the source terranes, we analyze the ILR transformed compositions for the major and trace element groups of the modern river sediments and Vandam volcaniclastic rocks using both hierarchical clustering analysis and PCA. These methods have previously been applied to geochemical investigations of provenance data and are useful for understanding potential groupings (e.g., Smosna et al., 1999; Pe-Piper et al., 2008). Hierarchical clustering essentially evaluates the "closeness" of given samples to each other, and the results are typically represented graphically on a dendrogram (Krzanowski, 2000). PCA is a technique for reducing dimensionality (Krzanowski, 2000) and can also be evaluated graphically, with similarity being indicated by a grouping on a plot of the principal component (Pe-Piper et al., 2008). We perform both the hierarchical clustering and principal component calculations in the "R" software package (R Core Team, 2010), using the "pvclust" library (Suzuki and Shimodaira, 2009) in the hierarchical clustering analysis to generate a dendrogram with boot-strapped *p*-values (Shimodaira, 2004) to provide an estimation of the robustness of the clusters indicated on the dendrogram. In detail, we use the "Ward" method of clustering and the "Euclidean" distance. In both the cluster analysis and PCA, the suite of major elements does not prove useful in discriminating different populations and, in the case of the principal component analysis, fails to capture significant portions of the data variance, so

these results are not presented, and the major elements set is not used in further analyses.

We then use the results of the clustering and PCA of using the suite of trace element data to inform choices of groups for linear discriminant analysis (LDA) to classify the unknown samples from the KFTB. Unlike the PCA or hierarchical clustering analysis, which do not require any *a priori* assumptions about the relation between samples, LDA is a guided machine learning approach that uses a set of training data divided into known groups to calculate the initial linear discriminant functions (Krzanowski, 2000). These functions are then used to classify unknowns as members of one of these preset groups. We complete these calculations in the "R" software using the "MASS" library (Venables and Ripley, 2002). We use the modern sediments and Vandam volcaniclastic rocks as the training data set to calculate the linear discriminant functions. We calculate multiple discriminant functions, using the ILR transformed compositions with different group assignments, which are described in more detail in the results section (section 5.1.4). To assess the robustness of each set of discriminant functions, we perform cross validation by iteratively recalculating the discriminant functions with one sample from the training data excluded. This sample is then classified according to the calculated discriminant function, and the overall percentage of correctly classified training data provides an indication of the robustness of the chosen groups and the accuracy of the functions. Finally, the KFTB samples are classified using the calculated linear discriminant functions.

5.1.3 Multivariate Characterization of Potential Source Areas

Analyses of the ILR-transformed trace element suite of potential source areas in terms of both PCA (Fig. 4A) and hierarchical clustering (Fig. 4B) show that

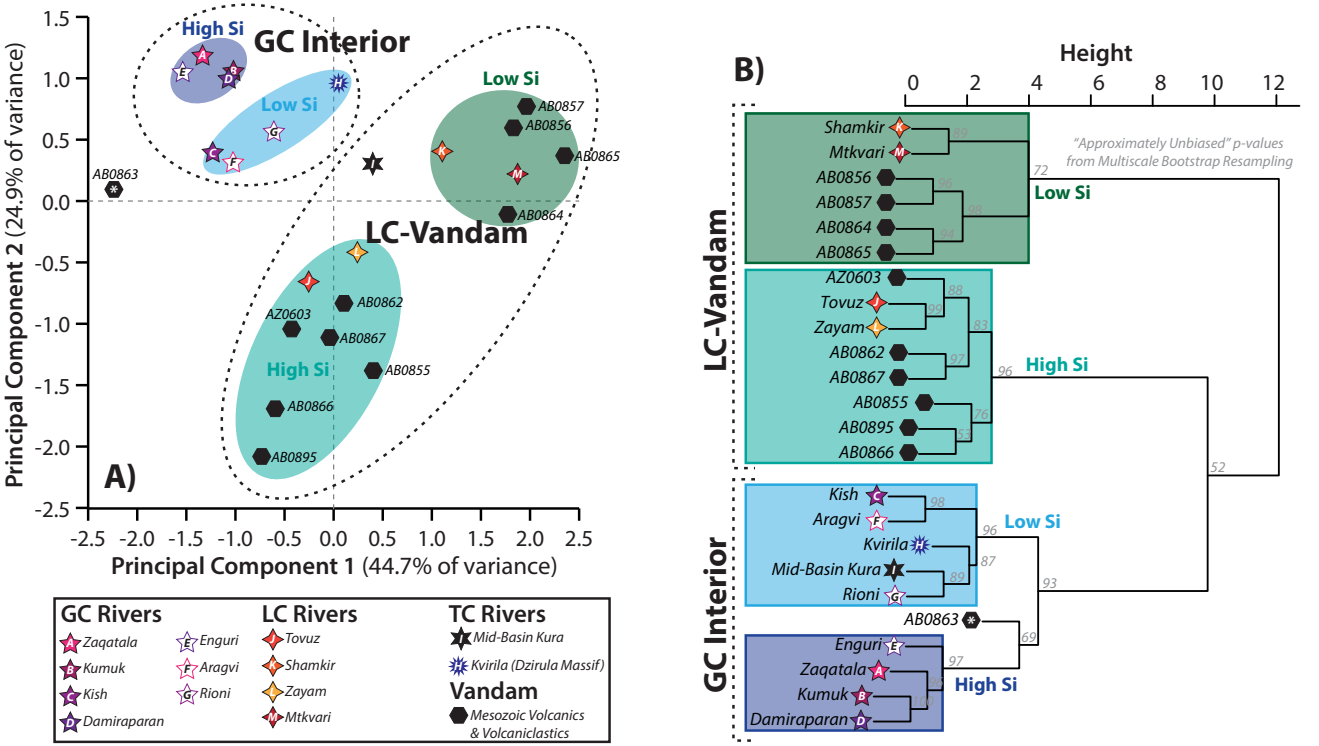

Figure 4. Source area characterization from multivariable statistics of bulk-rock trace element analyses. (A) Result of principal component analysis (PCA) highlighting separation of potential source terranes into four semi-distinct zones with one outlier (sample AB0863; symbol marked with asterisk); Kura River sample plots in the middle of these fields, consistent with the expectation that it is a mixture of all four potential sources. (B) Result of hierarchical clustering analysis highlighting a similar separation as suggested by the PCA in A. For hierarchical clustering, the height shown on the X-axis represents the Euclidean distance between given pairs on the dendrogram. GC—Greater Caucasus; LC—Lesser Caucasus; TC—Transcaucasus.

rivers draining the GC ($N = 7$) are generally geochemically distinct from both the four rivers draining the LC ($N = 4$) and the volcanic and volcanoclastic rocks in the Vandam zone ($N = 11$). In contrast, the LC rivers and the Vandam zone rocks broadly overlap (Fig. 4A). Thus, on the basis of trace element geochemistry and multivariate statistics, we can define two broad end-member sources. The first represents sourcing from the GC interior and is predominantly representative of the Jurassic–Cretaceous flysch, given the extent of the sampled watersheds (Fig. 1). The second represents sourcing from predominantly volcanic and volcaniclastic rocks in either the LC arc or Vandam. Two Transcaucasus rivers have samples that plot between these two end-member groups (Fig. 4A): the Kvirila, which drains the Dzirula Massif (Fig. 1), and the mid-basin Kura River, which incorporates drainages from both the GC and LC, although both show more similarity with the GC interior group than the LC arc–Vandam. Thus, we consider the Transcaucasus rivers as a third broad group within the context of the PCA results and will return to this idea when considering the LDA in Section 5.1.4.

Both the PCA and clustering analysis reveal more subtle divisions within the two broad groups and divide each into two separate subpopulations. For the LC-Vandam group, the cluster analysis yields an identical subdivision into two subgroups as the PCA, for which the first two principal components are able to account for ~70% of the variance (Fig. 4A). For the GC interior group, the subdivision indicated by the cluster analysis (Fig. 4B) is present but less distinct in the PCA, with the mid-basin Kura River sample plotting between the main GC and LC-Vandam groups (Fig. 4A) as previously noted. In both the PCA and the cluster analysis, Vandam sample AB0863 is found to be an outlier. The subdivisions of the two main groups broadly correspond to Si content with a boundary between the two being ~55 wt% SiO_2. Thus, we refer to the two subpopulations within each group as "high Si" and "low Si." In the GC interior group, the low Si member generally includes watersheds that drain more volcanic or volcaniclastic components and/or that have significant amounts of carbonate; e.g., the Kish and Aragvi Rivers have CaO of 25 wt% and 18 wt%, respectively. We use these subdivisions in the LDA that is considered in the next subsection.

It is important to note that while at the gross scale, the two broad geochemically defined sources correspond to geographically distinct sources (i.e., the interior of the GC range versus the LC and Vandam), the subdivisions within each group lack a clear correlation with geographic location. Specifically, for the GC-affiliated rivers, there is no clear along-strike pattern in terms of the two subpopulations. Likewise, for the LC-Vandam group, bedrock samples that are differentiated into the two distinct groups come from outcrops only a few kilometers from each other. Thus, we interpret these internal divisions to reflect geochemical heterogeneity in the sources but that this heterogeneity is not cross correlated with either tectonic or geographic location.

5.1.4 Linear Discriminant Analysis to Classify Unknowns—Methods

We use the four populations identified in the hierarchical clustering and PCA to define initial groups for LDAs (Tables 5 and 6). In detail, we run six different LDAs (LDA-1 through LDA-6), each of which uses a different suite of initial groups as training data. The three highest-performing LDAs have correct rates of classification from cross validation of >80% (Fig. 5; Table 5), similar to the methodology of von Eynatten et al. (2003). Here we present results from two of these (LDA-1 and LDA-3) because there is no robust statistical or geological reason to favor one over the other. We report the third high-performer (LDA-2) in the Supplemental Material (Figs. S13 and S14) because it classifies the KFTB sandstones essentially the same as LDA-1 and yields linear discriminant values that match those of LDA-3. We do not report the three low-performing LDAs (LDA-4 to LDA-6) because they have correct classification rates from cross validation of only 40%–70%. However, we note that one of the low-performing LDAs uses geographically defined groups in which all Vandam volcaniclastic rocks define one group and all LC river sediments define another, thus highlighting that the two geographic regions are not geochemically distinct.

The three high-performing LDAs all use groupings based on the results of the PCA and clustering analysis, with the same groupings for the high Si and low Si LC-Vandam groups but different groupings for the GC interior fields. Outlier Vandam sample AB0863 is excluded from all LDAs (Fig. 4). In LDA-1, the GC interior group is divided as indicated by the cluster analysis into the high Si and low Si subgroups, with the mid-basin Kura River sample included in the training data as part of the low Si group (Fig. 5; Table 6). In LDA-2, all of the GC interior samples are combined in a single group as indicated by the PCA, with the mid-basin Kura River sample excluded from the training data set. LDA-3 is identical to LDA-2 except the mid-basin Kura River sample is included as a separate group.

5.1.5 Linear Discriminant Analysis to Classify Unknowns—Results

Results from applying LDA-1 and LDA-3 to the sandstone samples of unknown provenance are reported in Figures 5 and 6 and Table 6. The most important observation from the geochemical proxies is clear up-section changes in provenance, generally from a LC-Vandam source to a GC interior source (Fig. 6).

In LDA-1, the oldest sample in the Vashlovani section (V-15) groups with LC-Vandam (high Si), with all younger samples classified as being derived exclusively from the GC interior. In contrast, all samples from the Sarica section are classified as having a predominantly LC-Vandam source, except for the youngest sample (S-1735), which groups with the GC interior (low Si). In both cases, there are no systematic up-section variations between high Si and low Si subgroups. Classification of the Xocashen section results in a LC-Vandam source for the lower two samples and a GC interior source for the upper three samples. Similarly, the Bozdagh section records a LC-Vandam source for the lower three samples and a GC interior source for the upper sample. LDA-1 classifies the entire Goy section as being derived from the LC-Vandam source. Of note, Goy is the only section where results from LDA-1 and LDA-2 differ significantly, with LDA-2 assigning the upper three samples to the GC interior source (Figs. S13 and S14).

TABLE 6. LINEAR DISCRIMINANT ANALYSIS (LDA) VALUES FOR KURA FOLD-THRUST BELT SAMPLES AND RESULTANT SOURCE CLASSIFICATIONS

Sample	LDA-1				LDA-2			LDA-3			
	LD1	LD2	LD3	Class	LD1	LD2	Class	LD1	LD2	LD3	Class
B-875	−17.907494	2.93255523	3.7746924	GC interior, low Si	−16.471512	2.1925358	GC interior	−15.766277	1.73355461	−4.7631457	MB Kura River
B-530	−0.5166766	2.5356821	3.195181	Volcaniclastic, high Si	0.5380016	3.3506704	Volcaniclastic, high Si	1.263677	3.3842422	−0.9388666	MB Kura River
B-280	3.5461964	2.98450504	−5.7391429	Volcaniclastic, high Si	−8.319897	0.5560797	Volcaniclastic, high Si	−7.59971	0.58172785	−0.9073078	MB Kura River
B-180	5.0719691	2.90326805	−1.9353734	Volcaniclastic, high Si	−3.436095	2.4004456	Volcaniclastic, high Si	−2.706021	2.60917207	0.4059887	MB Kura River
G-1620	−2.0041637	7.93351566	−7.6097206	Volcaniclastic, high Si	−35.0923	5.1527671	GC interior	−34.358021	5.4017262	0.19783666	GC interior
G-990	20.4986638	12.3400698	−8.1587683	Volcaniclastic, low Si	−21.527328	11.490125	GC interior	−20.761085	12.3169275	4.28962224	MB Kura River
G-680	−1.9939903	10.6373594	−6.6081099	Volcaniclastic, high Si	−43.189363	8.708327	GC interior	−42.442567	9.15480391	1.3718544	GC interior
G-200	11.3901546	5.74414834	−0.5980365	Volcaniclastic, high Si	−7.0973739	7.0951402	Volcaniclastic, high Si	−6.342858	7.77588076	3.62600433	MB Kura River
S-1735	−13.69148	5.01458997	−6.0939181	GC interior, low Si	−39.063392	1.7200245	GC interior	−38.345405	1.6791903	−1.8078593	GC interior
S-1100	53.2925811	7.03027187	−2.7457817	Volcaniclastic, low Si	80.337646	5.8878454	Volcaniclastic, low Si	81.050629	5.31370164	−4.8647969	Volcaniclastic, low Si
S-865	30.8240568	1.93826466	−4.1099078	Volcaniclastic, low Si	23.5743833	2.8798277	Volcaniclastic, high Si	24.327441	3.66836284	5.03900954	Volcaniclastic, high Si
S-610	−0.876575	9.56604275	−7.7178436	Volcaniclastic, high Si	12.7138846	1.136869	Volcaniclastic, high Si	13.361973	−0.9280393	−16.526111	Volcaniclastic, high Si
S-360	3.3155579	−0.4716073	−1.8692174	Volcaniclastic, high Si	0.4812111	−0.9667596	Volcaniclastic, high Si	1.206335	−0.7447173	0.76935151	MB Kura River
S-210	35.5443963	1.94093603	−5.9441851	Volcaniclastic, low Si	49.6087694	−0.1027866	Volcaniclastic, low Si	50.322604	−0.3196973	−2.0915427	Volcaniclastic, low Si
S-90	52.5561846	0.94921527	−8.5439719	Volcaniclastic, low Si	64.0689282	−0.3250262	Volcaniclastic, low Si	64.800511	−0.0557517	1.74886795	Volcaniclastic, low Si
X1-605	−27.248585	−0.1382819	5.7101709	GC interior, high Si	−33.84519	0.9084628	GC interior	−33.123309	1.0069485	−0.6468717	GC interior
X1-410	−19.807044	0.40718867	6.8841489	GC interior, low Si	−29.396833	3.072145	GC interior	−28.657443	3.55380926	2.15320294	MB Kura River
X1-330	−6.28886	7.06214744	−5.3934551	GC interior, low Si	−43.528644	5.773991	GC interior	−42.782171	6.35052776	2.54455889	GC interior
X1-3	10.112174	10.4120193	−7.6028218	Volcaniclastic, high Si	−14.225071	7.2708857	Volcaniclastic, high Si	−13.497026	7.21019298	−2.0638534	MB Kura River
X3-140	19.971446	1.59391034	0.1932576	Volcaniclastic, low Si	13.3068126	3.8780443	Volcaniclastic, high Si	14.062136	4.69999739	5.11849353	Volcaniclastic, high Si
V-1448	−42.34281	7.35572123	−13.098204	GC interior, high Si	−60.868078	−4.0749682	GC interior	−60.227542	−5.9856635	−15.786599	GC interior
V-1240	−28.060323	0.70628577	−0.8703693	GC interior, low Si	−47.148473	−0.7992382	GC interior	−46.430984	−0.7218563	−0.8329884	GC interior
V-1006	−18.594507	1.46776358	−9.9082545	GC interior, low Si	−56.791698	−2.1661298	GC interior	−56.063099	−1.6957915	2.12618876	GC interior
V-914	−32.404873	1.45370266	−6.0457849	GC interior, high Si	−54.337394	−3.2453529	GC interior	−53.640536	−3.6211608	−4.1722587	GC interior
V-602	−16.396058	3.48510799	−5.7811491	GC interior, low Si	−48.273779	1.1954331	GC interior	−47.543031	1.55353175	1.14553777	GC interior
V-212	−20.188285	4.33376382	−9.0275314	GC interior, low Si	−51.038731	−0.4756029	GC interior	−50.328057	−0.5988939	−2.4116632	GC interior
V-15	−8.6959968	3.83073192	−14.608023	GC interior, low Si	−55.355275	−1.0411094	GC interior	−54.621668	−0.4853395	2.71280417	GC interior

Notes: MB—mid-basin; GC and LC are defined as abbreviations for the Greater and Lesser Caucasus; Class implies into which group from the training dataset that samples is classified; LDA—linear discriminant analysis.

Classifying using LDA-3, which includes the mid-basin Kura River as a separate source, produces similar results as LDA-1 and LDA-2 for some of the sections but dramatically different results for others (Figs. 5 and 6; Table 6). The Vashlovani and Sarica sections are again classified as dominantly sourced from the GC interior and LC-Vandam, respectively, although Sarica sample S-360 is classified as similar to the mid-basin Kura River sample. In contrast, all Bozdagh samples are reclassified as being similar to the mid-basin Kura River sample. Both the Xocashen and Goy sections are partially reclassified, resulting in alterations between GC interior and Kura River sources, although the lowest sample in Xocashen remains as sourced from LC-Vandam.

5.1.6 Interpretation of Bulk Geochemistry in Context with Petrography

While the bulk geochemistry is useful for both defining potential source areas and classifying the KFTB sandstones within that context, it is somewhat abstract without a mineralogic or petrologic context. To address this, we develop a comparison between the geochemistry and the petrography of the foreland sediments by way of using the results of the LDA presented in Section 5.1.4. In detail, we consider only the values of the first linear discriminant (i.e., the *x*-axis in Fig. 5) for the different LDAs. Because the decision boundaries within the LDAs are nearly vertical, the first linear discriminant (LD1) is relatively effective as a single numeric metric of source affinity. Specifically, we use LD1 of analyses LDA-1 and LDA-2. We use LDA-2 rather than LDA-3 because it is simplest to interpret the results of the petrography in the context of LDA-2, which uses GC interior, LC-Vandam high Si, and LC-Vandam low Si source divisions, whereas in LDA-3, the mid-basin Kura River source is effectively a mixture of the GC interior and LC-Vandam sources (Fig. S13). It is possible to make this switch because the LD1 values of LDA-2 and LDA-3 are the same, making them largely interchangeable for this purpose.

To compare the LDA results to the sandstone petrography (Fig. 7), we first perform a random forest regression using the percentage of the point-count

components to predict the value of LD1 for both LDA-1 and LDA-2. Random forest regression is a useful method for assessing the importance of sets of multivariate data in contributing to a single variable, in this case, the value of LD1 (e.g., Grömping, 2009). For each LDA, we use the results of the random forest regression to identify the most important components from the sandstone petrography and assess the extent to which they alone or in aggregate correlate to the LDA.

The random forest regression highlights that the six most important petrographic components in LDA-1 are calcium-rich plagioclase, pyroxenes and amphiboles, volcanic lithics, total quartz, sedimentary lithics, and miscellaneous "other" (Fig. 7A; Fig. S8). In detail, the combined percentage of the first three components (calcium-rich plagioclase, pyroxene and amphibole, and volcanic lithics) is positively correlated with LD1, whereas the combined percentage of the last three components (quartz, sedimentary lithics, and the generic "other" grains) is negatively correlated with LD1 (Fig. 7B; Fig. S8). This analysis is consistent with the former three components broadly being associated with a LC-Vandam source and the latter three components being associated with a GC interior source. For LDA-2, the random forest regression is similar but suggests that the two sources are each predominantly defined by only two components: calcium-rich plagioclase and pyroxenes and amphibole for the LC-Vandam source, and quartz and sedimentary lithic components for the GC interior source (Fig. 7C). These components show the same positive and negative linear relationships with LD1 as in LDA-1 but with higher correlation coefficients (Fig. 7D).

Two details that are important to highlight in the comparison of the geochemistry and petrography are that, broadly, (1) the differentiation of LC-Vandam or GC interior geochemical sources reflects relative abundances of the petrographic components discussed above as opposed to strict presence or absence of the relevant petrographic components, and (2) the petrographic components that are important in defining the two sources differ in their relative chemical stability (e.g., Lasaga et al., 1994, and references therein). Specifically, the petrographic components that are correlated with

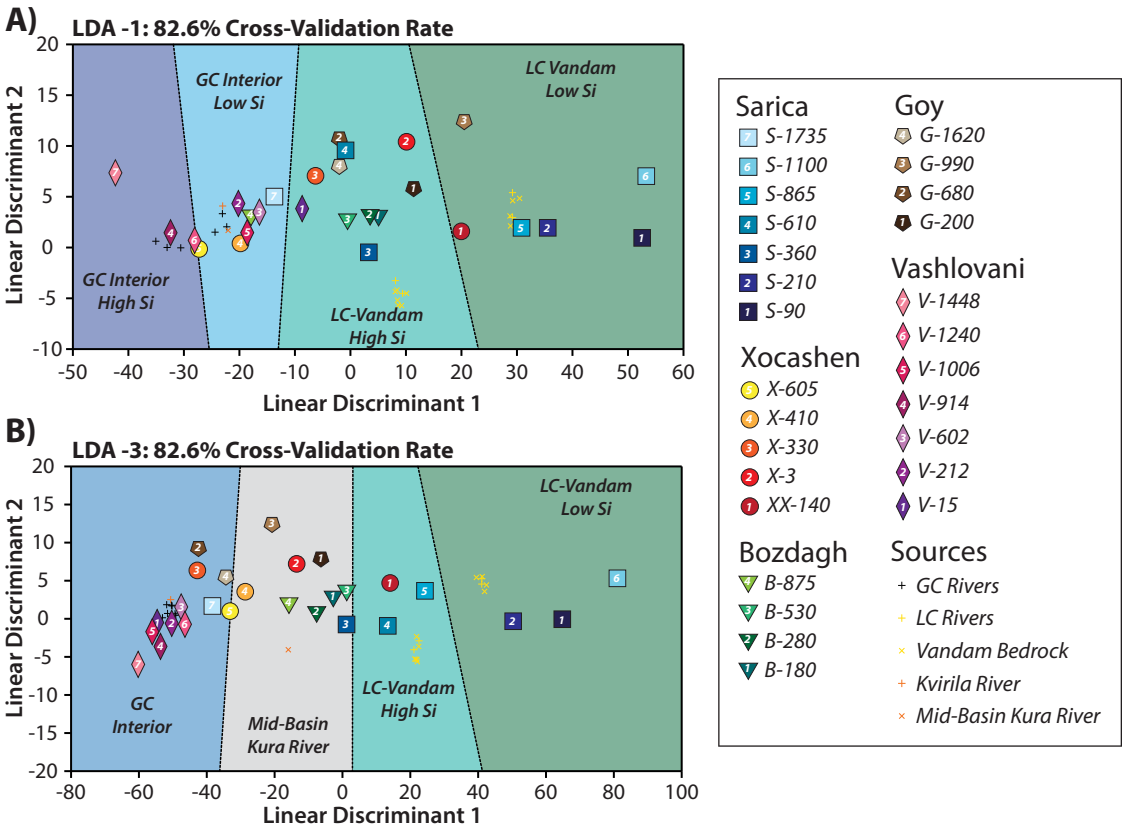

Figure 5. Results of linear discriminant analysis (LDA) considering two different source definitions (LDA-1 and LDA-3); cross-validation rates are the same for both. See Section 5.1 in text for further explanation. Results including LDA-2 are provided in Figure S13 (see text footnote 1). GC—Greater Caucasus; LC—Lesser Caucasus.

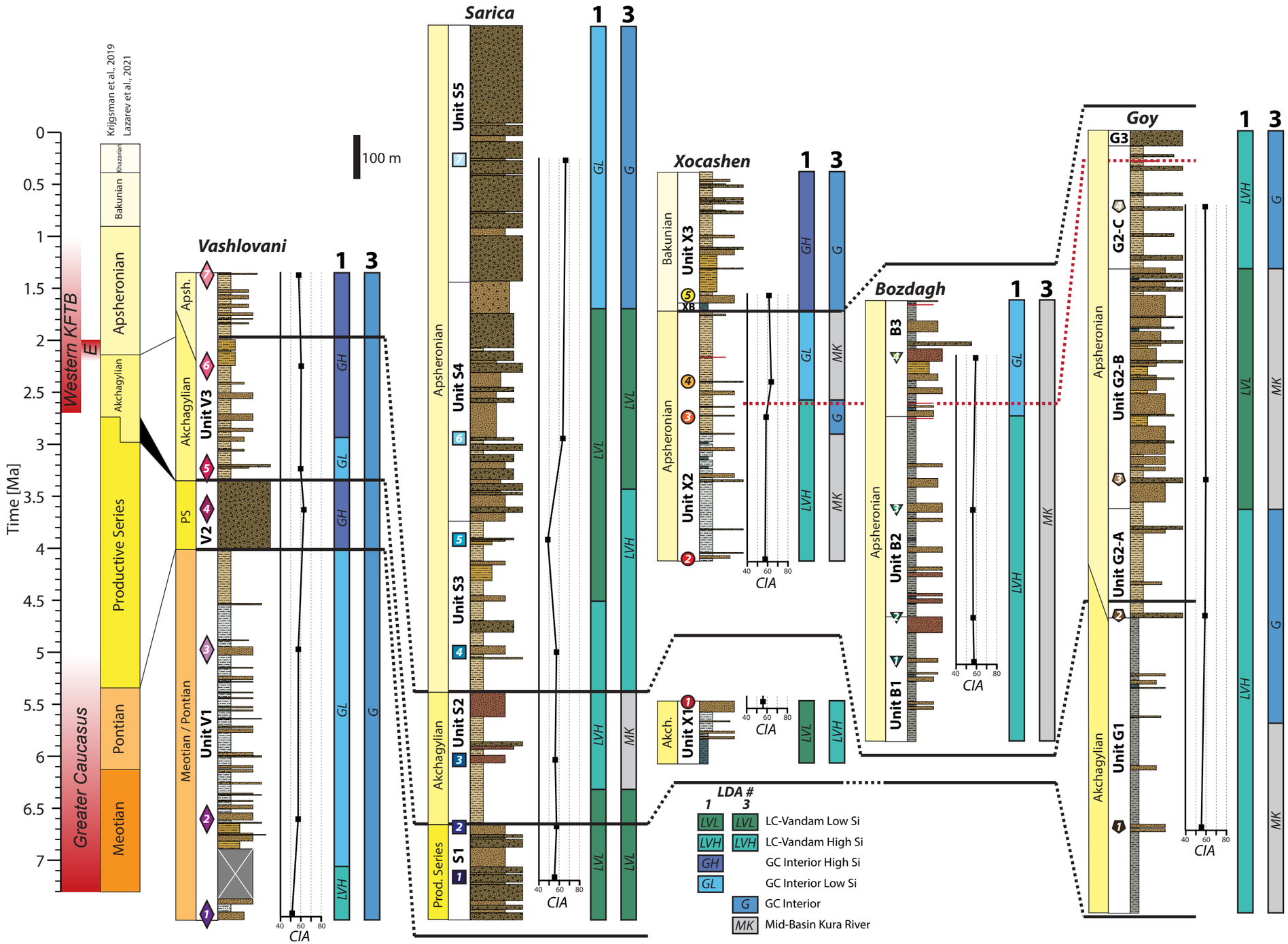

Figure 6. Results of two different linear discriminant analyses (LDAs) (LDA-1 and LDA-3; shown as bars labeled 1 and 3, respectively) considered as a function of stratigraphic position. Correlations and time scale are identical to those shown in Figure 2. Also shown are the chemical index of alteration (CIA; Nesbitt and Young, 1982). Comparisons of CIA to other weathering indices are shown in Figure S12 and discussed in Section S2.2.5 (see text footnote 1). Note that generally we do not have constraint on where within the sections between samples provenance would change, so the location of the changes shown here are schematic. Version of this figure considering results of LDA-2 is provided in Figure S14. KFTB—Kura Fold-Thrust Belt; E—eastern KFTB; GC—Greater Caucasus; LC—Lesser Caucasus.

TABLE 7. SAMPLES AND REFERENCES FOR THOSE SAMPLES USED TO DEFINE COMPOSITE DETRITAL ZIRCON SOURCES

Sample name in reference	Source designation	Reference
CGC-1	GCSL	Tye et al., 2020
CGC-2	GCSL	Tye et al., 2020
CT130924-9A	WGCV	Trexler et al., 2022
EGC-1	GCSL	Tye et al., 2020
EGC-2	GCSL	Tye et al., 2020
EGC-3	GCSL	Tye et al., 2020
EGC-4	GCSL	Tye et al., 2020
EGC-5	EGCV	Tye et al., 2020
EGC-6	EGCV	Tye et al., 2020
EGC-7	EGCV	Tye et al., 2020
GC-41	GCSL	Allen et al., 2006
K3	GCSL	Vasey et al., 2020
LC-1	TBLC	Tye et al., 2020
LC-2	TBLC	Tye et al., 2020
LC-3	TBLC	Tye et al., 2020
LC-4	TBLC	Tye et al., 2020
N1	PJS	Vasey et al., 2020
N2	PJS	Vasey et al., 2020
N3	PJS	Vasey et al., 2020
N4	PJS	Vasey et al., 2020
TC-1	TBLC	Tye et al., 2020
WGC-1	GCB	Tye et al., 2020
WGC-2	GCB	Tye et al., 2020
WGC-3	WGCV	Tye et al., 2020
Bum	GCSL	Forte et al., 2022
Dneiper	EUI	Wang et al., 2011
Don	EUI	Wang et al., 2011
Inguri	GCB	Cowgill et al., 2016
Katex	GCSL	Forte et al., 2022
Kherla	GCSL	Forte et al., 2022
Khopuri	GCSL	Forte et al., 2022
Kish	GCSL	Forte et al., 2022
Kumuk	GCSL	Cowgill et al., 2016
Kura	TBLC	Cowgill et al., 2016
NE-GC	GCSL	Cowgill et al., 2016
SE-GC	EGCV	Cowgill et al., 2016
Svianas Khevi	GCSL	Forte et al., 2022
NW-GC	PJS	Cowgill et al., 2016
Tovuz	TBLC	Cowgill et al., 2016
Tskhradzmula	GCSL	Forte et al., 2022
Volga	EUI	Allen et al., 2006
Volga	EUI	Wang et al., 2011

Source abbreviations: EUI—Eurasian interior, PJS—pre-Jurassic sedimentary rocks, GCB—Greater Caucasus basement, GCSL—Greater Caucasus siliclastic strata, EGCV—Eastern Greater Caucasus volcaniclastics, WGCV—Wester Greater Caucasus volcaniclastics, and TBLC—Transcaucasus basement and Lesser Caucasus.

the LC-Vandam source (e.g., calcium-rich plagioclase, pyroxene) would be expected to weather more quickly than some of the components that define the GC interior (e.g., quartz). Thus, an apparent up-section change from a LC-Vandam source to a GC interior source could reflect a true change in sediment provenance from these two broad geographic source regions or could be reflective of increased weathering of a LC-Vandam–like source. We consider these two options further in the Discussion (section 6.1.3) in light of the results of DZ U-Pb ages presented in the following section.

5.2 U-Pb Detrital Zircon Ages

5.2.1 Analytical Methods

U-Pb geochronology of DZs is a versatile tool widely used for assessing the provenance of siliciclastic sediments (e.g., Fedo et al., 2003; Andersen, 2005; Gehrels, 2012). We perform U-Pb geochronologic analyses of individual DZs from samples of seven Kura Basin sandstones via laser ablation multi-collector inductively coupled plasma mass spectrometry (LA-MC-ICP-MS) at the Arizona LaserChron Center (Tucson, Arizona). Analytical procedures relevant at the time of analysis (2011) are described by Gehrels et al. (2006, 2008). Approximately 110 grains were dated per sample. Because the potential existed for observing young grains (<10 Ma) in many of the samples, we used a 20 s integration time for all samples. Analyses were excluded from plots and statistical treatments based on unacceptable discordance, precision, or in-run fractionation. For extremely young grains (<10 Ma), discordance was largely ignored in choosing whether to include or exclude particular analyses because the calculated $^{206}Pb/^{207}Pb$ for these grains are subject to extremely low precision due to the low concentrations of ^{207}Pb (Gehrels, 2012). Complete analyses are presented in the Supplemental Material (Table S7, see footnote 1).

To consider potential sources for the Kura Basin DZ samples, we also define composite source populations based on the classification from Tye et al. (2020) as described in Section 2.3. Specifically, to define a composite source population, we combined available published DZ age populations from individual samples into a single, composite sample using the same set of samples as Tye et al. (2020), including those from Allen et al. (2006), Wang et al. (2011), Vincent et al. (2013), Cowgill et al. (2016), Trexler et al. (2022), Vasey et al. (2020), and Tye et al. (2020), but supplemented with additional samples reported by Forte et al. (2022). For the samples from Forte et al. (2022) not classified by Tye et al. (2020), we use multidimensional scaling (Vermeesch, 2013) to assess which source samples, and by proxy which composite source terrane, these newer samples are most similar to. Multidimensional scaling (MDS) plots suggest that all of the Forte et al. (2022) samples are best classified as part of the GC siliciclastic composite source. Table 7 lists the samples used from these sources and to which source terrain they are assigned. We also follow Tye et al. (2020) in tracking the six distinct age populations defined in Tye et al. (2020) and discussed in Section 2.3 within both the composite sources and basin samples.

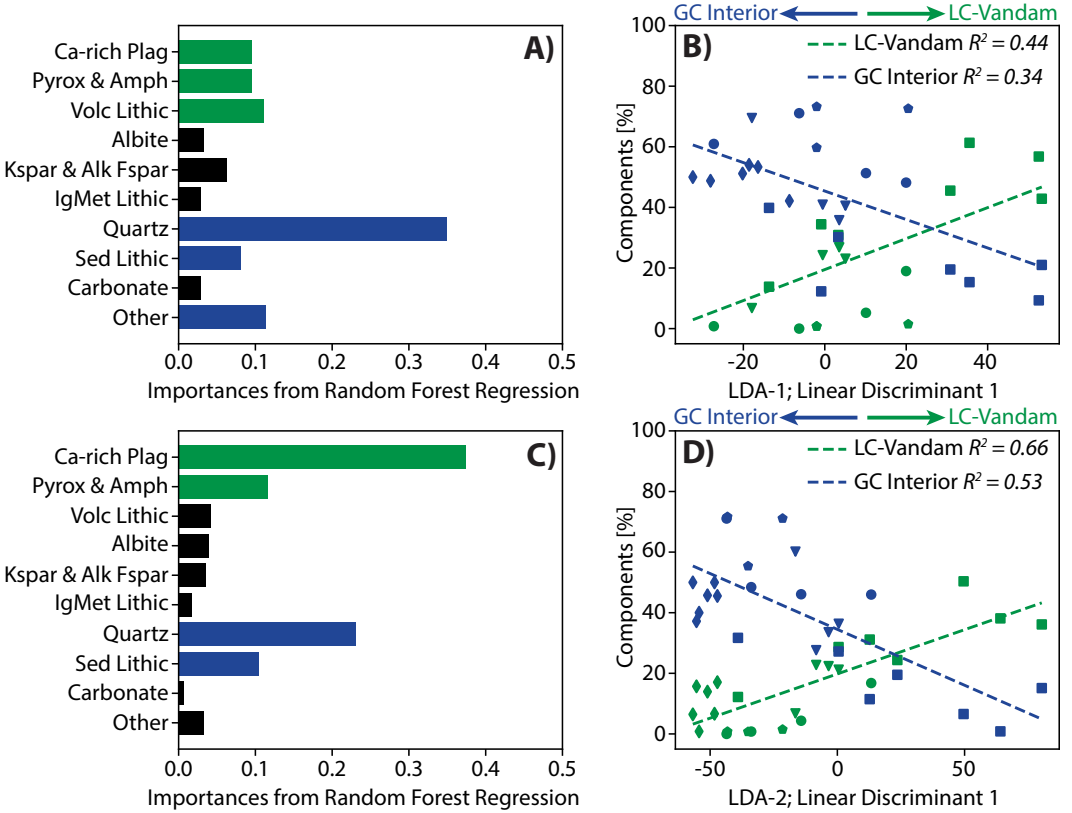

Figure 7. Comparison of linear discriminant analyses (LDAs) of bulk geochemistry and sandstone petrography. (A) Results of random forest regression that assesses ability of a given point count category to predict value of linear discriminant 1 within analysis LDA-1. Green and blue bars indicate components most associated with Lesser Caucasus (LC)–Vandam and Greater Caucasus (GC) interior source, respectively. Black bars indicate components that are less diagnostic for distinguishing between sources. Abbreviations are as follows: Ca-rich Plag—calcium-rich plagioclase; Pyrox & Amph—pyroxene and amphibole; Volc Lithic—volcanic lithic; Kspar & Alk Fspar—potassium feldspar and alkaline feldspar; IgMet Lithic—igneous or metamorphic lithic; Sed Lithic—sedimentary lithic. (B) Plots and linear regressions between summed percentages of components related to either LC-Vandam or a GC interior source as identified in Figure 4A and linear discriminant 1 of LDA-1. (C, D) Same as A and B but considering linear discriminant 1 for LDA-2.

5.2.2 Statistical Methods

For visualizing age distributions, we use both probability distribution plots (PDPs) and kernel density estimates (KDEs) because each has distinct advantages and disadvantages (e.g., Saylor and Sundell, 2016). We use the DensityPlotter software (Vermeesch, 2012) to generate both the PDPs and KDEs for the composite sources and our new samples. We use three different methods to compare the U-Pb ages from our new basin samples with those from potential source terranes: MDS plots (Vermeesch, 2013), Monte Carlo unmixing models (Sundell and Saylor, 2017), and Bayesian population correlation (BPC) (Tye et al., 2019). Ultimately, the three different methods yield largely similar results, so for simplicity, we focus on the results of the BPC because these are the easiest to quantitatively relate to the results of classifying the sediments by their bulk geochemistry. The Supplemental Material contains both methodological details and results of the MDS and Monte Carlo unmixing models (see Section S2.3). In the following, we briefly review key aspects of the BPC method, with similar details for the MDS and Monte Carlo unmixing provided in Section S2.3.1 in the Supplemental Material.

BPC relies on constructing probability model ensembles for each sample and then uses these probability model ensembles in pairwise comparisons to calculate a degree of similarity, i.e., the BPC value (Tye et al., 2019). As shown by Tye et al. (2019), BPC is relatively insensitive to differences in sample size between samples being compared, removing the need for subsampling as is required with unmixing techniques (e.g., Sundell and Saylor, 2017). Output BPC values vary from 0 to 1, where a value near 1 implies a high degree of similarity. The BPC calculation also estimates uncertainty on these values.

5.2.3 U-Pb Age Distributions

We present PDPs and KDEs for both the seven composite DZ sources (Fig. 8) and seven KFTB DZ samples (Fig. 9; Fig. S15) to enable visual comparison prior

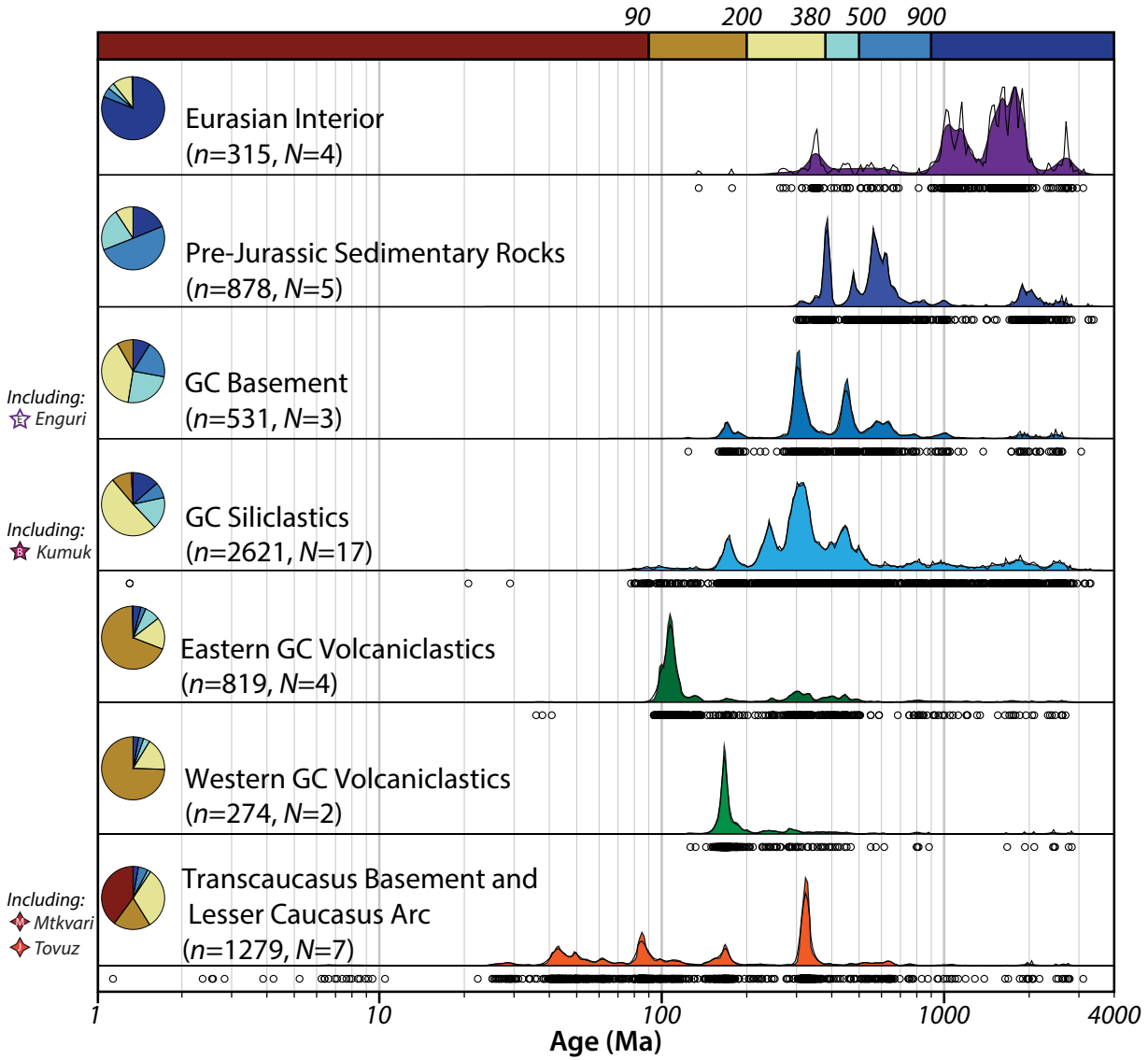

Figure 8. Composite detrital zircon populations used to define source terranes, following definitions by Tye et al. (2020). See text for additional discussion of source terranes. Plot was generated using DensityPlotter (Vermeesch, 2012) with filled and colored kernel density estimates (KDEs) and probability distribution plots (PDPs) represented by hollow black curves. Hollow circles indicate ages of individual grains that contribute to the calculation of the KDEs and PDPs. KDEs were calculated using adaptive bandwidth (see Vermeesch, 2012). Colors of KDEs are for reference in subsequent figures. Colored bars across top show six diagnostic age ranges identified by Tye et al. (2020). Pie charts show proportions of these diagnostic ages within each composite sample. Both total number of zircons that define each source (*n*) and total samples contributing to the source (*N*) are shown. Composite samples are detailed in Table 7 and reported by Allen et al. (2006), Wang et al. (2011), Cowgill et al. (2016), Vasey et al. (2020), Tye et al. (2020), Trexler et al. (2022), and Forte et al. (2022). When one of the composite samples contains a river sample discussed in this effort, we show the corresponding sample name and symbol (e.g., Fig. 1). GC—Greater Caucasus.

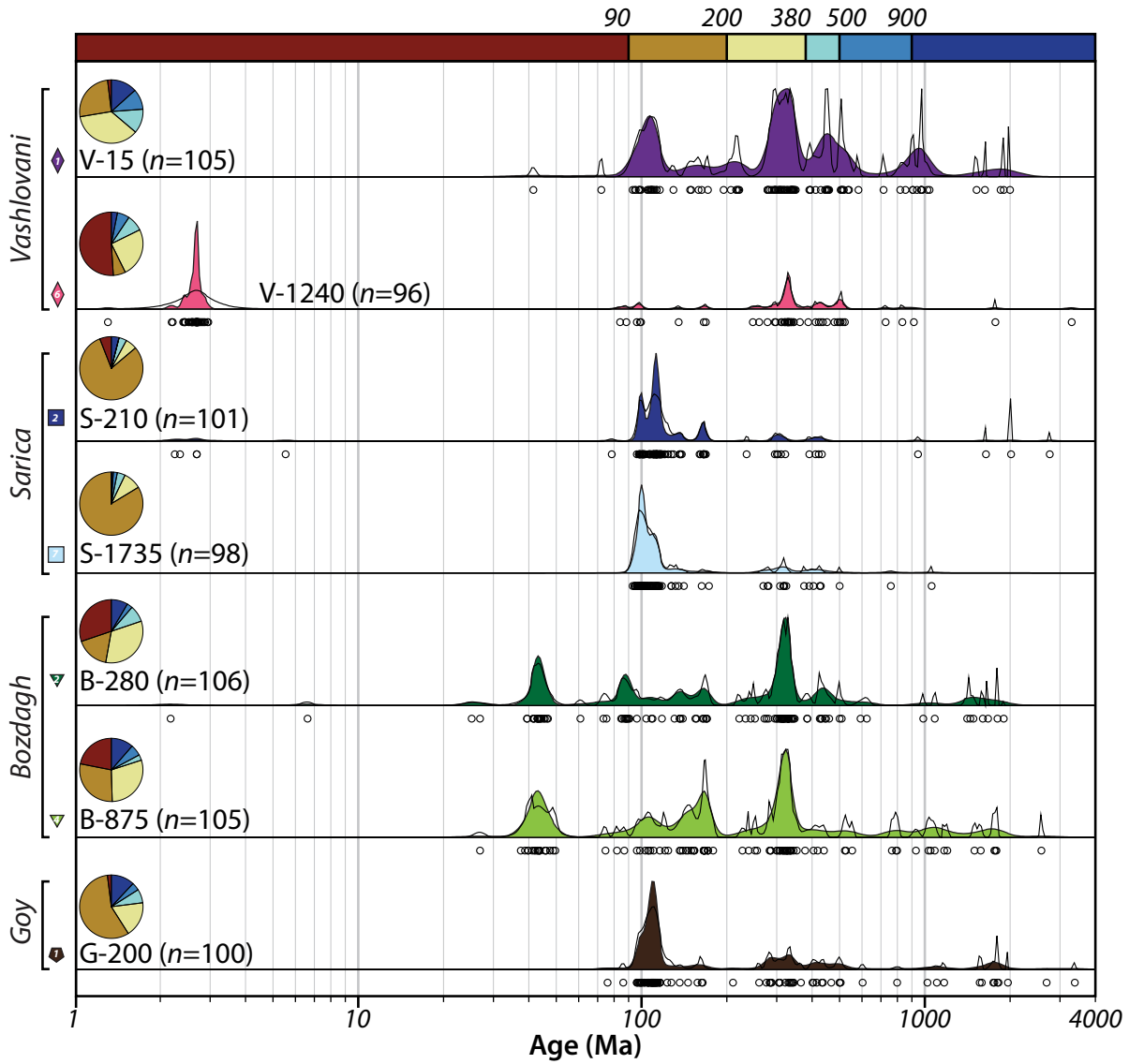

Figure 9. Detrital zircon (DZ) populations for seven new Kura Fold-Thrust Belt samples. Setup of figure is identical to that of Figure 8. DZ populations are grouped by stratigraphic section to ease comparison between tops and bottom of sections. Sample symbols as defined in Figure 1 and used throughout the figures are shown to the left of each spectra. Alternative version of this figure with probability distribution plots and kernel density estimates stacked by approximate stratigraphic age is presented in Figure S15 (see text footnote 1).

to statistical comparison. It is important to note that the definition of source terranes is different between the U-Pb DZs and the geochemical classifications, a point we return to in the Discussion (section 6.1.2). The vast majority of zircon ages within the thrust belt samples are Mesozoic and Paleozoic, although there are some Cenozoic grains in the two samples from the Bozdagh section (B-280 and B-875) and the samples from the lower Sarica and upper Vashlovani sections (S-210 and V-1240, respectively). The only samples with sizeable portions of Proterozoic and older grains are the lower Vashlovani sample (V-15) and both Bozdagh samples (Fig. 9; Fig. S15). Within the context of the six distinctive age populations defined by Tye et al. (2020), the vast majority of samples are dominated by mixtures of <90 Ma grains associated with the LC arc, 90–200 Ma grains associated with either the LC arc or GC rifting, or 200–380 Ma grains associated with the Variscan orogeny. For all samples except V-15, older age populations make up <25% of the total grains. Both S-210 and V-1240 are notable for containing statistically significant numbers of extremely young grains with mean ages of 2.5 ± 0.24 Ma (n = 3) and 2.66 ± 0.046 Ma (n = 47), respectively, which Forte et al. (2015a) used to determine MDAs. The sources of these young grains are unknown, but they overlap in age with silicic volcanism in both the LC (Karapetian et al., 2001) and GC (Shcherbakov et al., 2022).

5.2.4 Statistical Comparisons of KFTB Sandstones with Sources

We remove the populations of very young grains from samples S-210 and V-1240 prior to conducting the statistical comparisons because these grains most likely reflect contemporaneous, or nearly contemporaneous, regional volcanism at the time of deposition. Because none of the composite sources have age populations of this age, including these grains would effectively mask the provenance signature in the statistical methods we employ. That problem is particularly acute for V-1240 because the young grains constitute nearly 50% of the total population in this sample. We present the results of the BPC comparison (Fig. 10) from west to east. Results of the MDS and Monte Carlo unmixing are presented in the Supplemental Material (Fig. S16).

In the BPC comparison (Fig. 10), the two samples from the Vashlovani section have the highest degree of similarity with the GC siliciclastic source along with elevated similarity with the eastern GC volcaniclastic, GC basement, and Transcaucasus basement–LC arc sources. In detail, the second-highest similarity in sample V-15 is to the eastern GC volcaniclastic source, whereas in V-1240 it is to the Transcaucasus basement–LC arc source. Both samples from the Sarica section show a strong similarity with only eastern GC volcaniclastic source (>0.9), with the next-highest similarity being with the Transcaucasus basement–LC arc source (<0.6). Both samples from the Bozdagh section are very similar to the Transcaucasus basement–LC arc source (>0.9) but also show some similarity with the GC siliciclastic source (>0.7). Finally, the G-200 sample from the Goy section is very similar to the eastern GC volcaniclastic source (0.98), with the next similar sources being GC siliciclastic and Transcaucasus basement–LC arc (both <0.7).

Taken together, the results of BPC, MDS, and Monte Carlo unmixing are broadly consistent with each other (Fig. 10; Fig. S16). All methods indicate a close correspondence between samples from the same section, with samples from the top and bottom of the same section being more generally similar to one another than to samples from different sections, even if those samples are more closely time equivalent (Fig. S15). In addition, the three methods indicate broadly consistent sources for the individual samples, although there are some exceptions. The Vashlovani and Bozdagh samples show both the most complicated sourcing and the largest amount of disagreement between the methods. For Vashlovani, all methods indicate significant contributions from GC siliciclastic and GC basement but vary in the extent to which they include eastern GC volcaniclastics or Transcaucasus basement and LC arc. All three methods indicate Transcaucasus basement–LC arc as the primary source for the Bozdagh samples, with some minor inputs from other sources, including GC siliciclastics, eastern GC volcaniclastics, and western GC volcaniclastics, although the proportions or importance of these varies between methods. In contrast, in both Sarica samples and the lower Goy sample, all methods consistently indicate nearly exclusive sourcing from the eastern GC volcaniclastics source (Fig. 10; Fig. S16).

6. DISCUSSION

6.1 Reconciling Differing Results of Geochemical and Detrital Zircon Provenance Methods

The most fundamental result of this study is that the geochemical and/or petrographic and DZ-based approaches yield provenance interpretations for the KFTB sandstones that diverge in meaningful ways for several of the measured sections. The geochemical and/or petrographic proxies indicate clear up-section changes in provenance from a LC-Vandam source to a GC interior source (Fig. 6). In contrast, DZ-based methods generally suggest limited up-section change (Figs. 9 and 10). Thus, if taken in isolation, each method leads to a different interpreted provenance—and potentially tectonic—history for the Kura Basin and GC. To reconcile these apparently divergent results, it is necessary to explain why the results from the two methods differ.

Interpreting the apparent divergence in KFTB sandstone provenance is complicated by the fact that the definitions of the source terranes that naturally emerge from each data set differ from one another. As a result, there is no single set of source terranes that suitably explains the results from both methods. Specifically, Tye et al. (2020) found that five statistically distinct sources within the GC emerge from the U-Pb DZ ages (pre-Jurassic sedimentary, GC basement, GC siliciclastic, eastern GC volcaniclastic, western GC volcaniclastic) and that samples sourced from volcanic and volcaniclastic rocks in the LC (Transcaucasus basement–LC arc source) can be distinguished from those in the GC (eastern and western GC volcaniclastic sources; Figs. 8 and 10). In contrast to the five sources that emerge from the DZ analyses, our sampling of

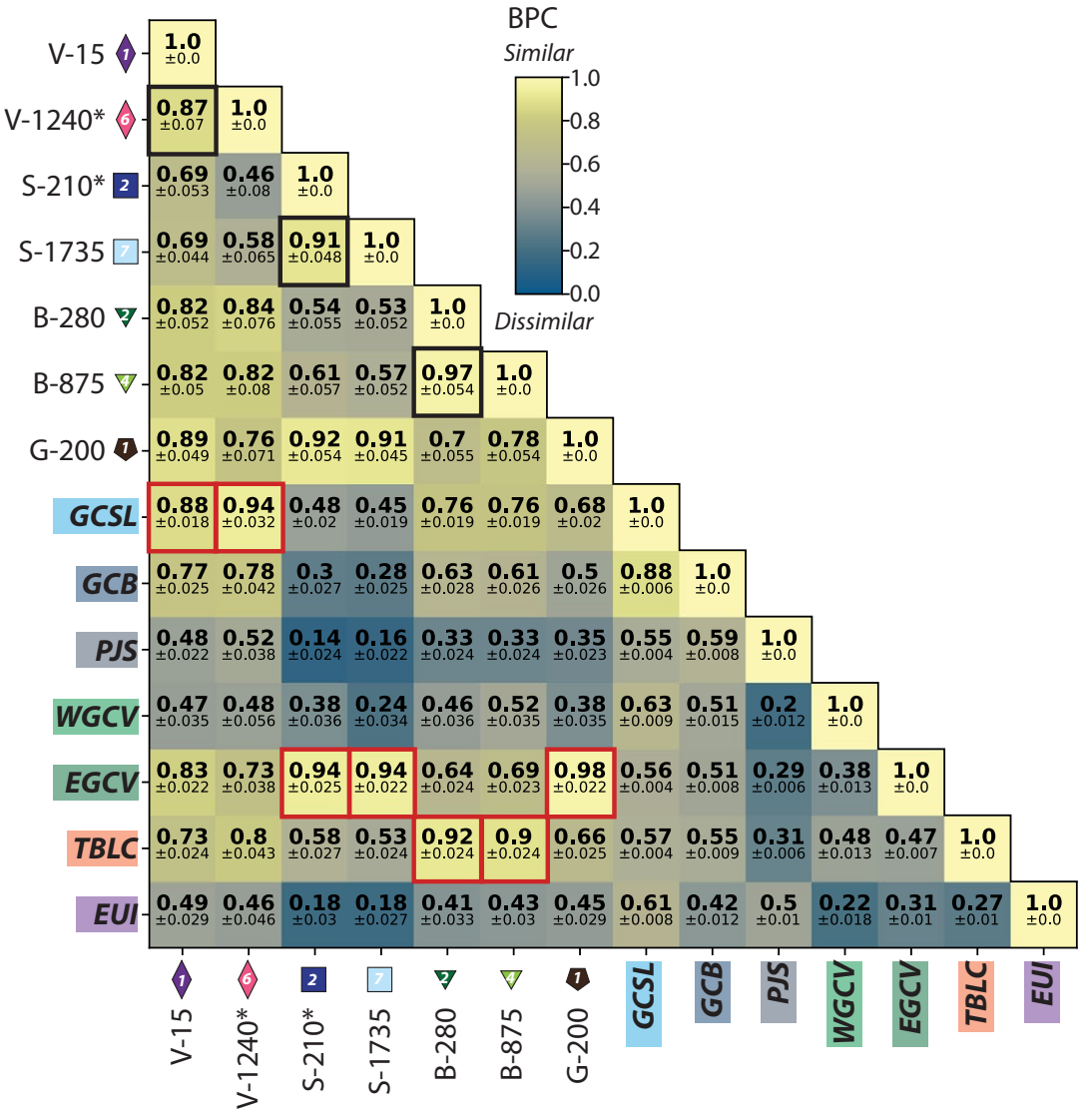

Figure 10. Results of Bayesian population correlation (BPC) (Tye et al., 2019) between Kura Fold-Thrust Belt (KFTB) samples and composite sources. Each box shows the BPC value (between 0 and 1) and the uncertainty on this value. Red boxes indicate composite source and KFTB sample with highest similarity based on BPC; thick black outlines indicate comparisons between samples from top and bottom of individual sections; note that the BPC values between the top and bottom of each sample are relatively high, indicating minimal up-section changes in detrital zircon–derived provenance. To minimize bias, samples V-1240 and S-210 were modified (indicated by *) by removing young populations of grains that define maximum depositional ages; see text for explanation. Source terrane abbreviations: GCSL—Greater Caucasus (GC) siliciclastics; GCB—GC basement; PJS—pre-Jurassic sedimentary rocks; WGCV—western GC volcaniclastics; EGCV—eastern GC volcaniclastics; TBLC—Transcaucasus basement and Lesser Caucasus arc; EUI—Eurasian interior.

similar regions using bulk geochemistry yields a maximum of four statistically distinct sources within the combined GC and LC and also fails to distinguish Jurassic–Cretaceous volcanic and volcaniclastic sources within the GC from those in the LC (Fig. 4; Fig. S10).

To explore the cause underlying the apparent divergence in provenance from the different methods, we first consider the relationships, commonalties, and differences within the definitions of source terranes between the DZ and geochemical approaches and clarify how these do, or do not, relate to each other. We then consider how the source definitions map into implications for the sourcing of the KFTB sandstones before providing a parsimonious explanation for the apparent disagreement.

6.1.1 Source Definitions

The primary difference between the DZ and geochemical approaches is a difference in the degree of geographic specificity, with the DZ approach providing more geographic granularity than the geochemical and/or petrographic approaches. The DZ data permit identification of sediment sourcing from specific geographic areas within the Caucasus region that are not distinguishable geochemically. For example, the DZ method has the ability to differentiate contributions to a KFTB sandstone from the southeastern GC range front to the northeast (i.e., eastern GC volcaniclastic source) versus from the southwestern GC range front to the northwest (i.e., western GC volcaniclastic source) versus from the LC to the south (i.e., Transcaucasus basement–LC arc source) (e.g., Fig. 1; Tye et al., 2020). In contrast, contributions from these regions are indistinguishable from one another geochemically or petrographically and would all broadly appear as coming from a single composite LC–Vandam source (Fig. 4). The apparent homogeneity of the LC–Vandam source in the geochemical data is consistent with prior suggestions of a genetic link between the LC arc and the volcanic and volcaniclastic rocks within the GC and specifically the Vandam (e.g., Kopp and Shcherba, 1985). However, in the context of interpreting provenance within the adjoining foreland, this similarity limits the geographic specificity of geochemical and petrographic classifications. Another example is the ability of the DZ method to identify sourcing of a KFTB sandstone from the interior of the western GC, which would be indicated by contributions from either the pre-Jurassic sedimentary or GC basement sources (e.g., Fig. 1; Tye et al., 2020), whereas sourcing from anywhere in the interior of the range appears in the geochemical or petrographic data as a generic GC interior source without the capacity for further geographic clarification (i.e., western versus eastern GC; Fig. 4). Unfortunately, attempts to extract more geographic information by considering the subpopulations of the geochemical sources, i.e., the high Si and low Si subpopulations of both the GC interior and LC–Vandam sources (Fig. 4), are not successful.

The non-overlapping source definitions within broad geographic regions (e.g., all of the GC-associated DZ sources versus the two geochemical and/or petrographic GC sources) are mostly simply explained in terms of lithologic heterogeneity and the sensitivity of the different methods to that heterogeneity. For example, the Aragvi, Kish, and Damiraparan Rivers within the GC all contain, or are directly adjacent to, samples classified as being part of the GC siliciclastic DZ source but span both GC-affiliated geochemical sources, with the Aragvi and Kish River samples being part of the low Si GC interior source whereas the Damiraparan River sample is part of the high Si GC interior source. Much of these differences likely reflect variable geology within the source catchments, e.g., both the Aragvi and Kish Rivers have high CaO (compared to the Damiraparan), suggesting that in this case the divergence in geochemical classifications may in part reflect the presence or absence of significant carbonate, a characteristic that would not be detectable with DZ geochronology. Similar patterns are observed in the LC- and/or Vandam-associated sources. At the individual river level, both the Tovuz and Mtkvari Rivers were classified as a part of the Transcaucasus basement and LC arc source on the basis of their U-Pb ages, and while they geochemically are both categorized as a LC-Vandam source, the Mtkvari sample is contained within the low Si subpopulation whereas the Tovuz sample is contained within the high Si subpopulation. Similarly, bedrock samples defined geochemically as either of the LC-Vandam sources are contained within watersheds of catchments from which modern sediment U-Pb age populations were used by Tye et al. (2020) to define the eastern GC volcaniclastic source. This includes bedrock sample AB0862, which geochemically is classified here as from the high Si source but whose DZ population is part of the samples used to define the eastern GC volcaniclastic DZ source (Cowgill et al., 2016; Tye et al., 2020).

Petrography on some of the samples from the Vandam region in the GC does not reveal distinguishing characteristics for interpreting geographic or other information from the LC-Vandam subpopulations (Fig. 4; Table S2). Both geochemical populations span samples that are texturally volcanic compared to volcanoclastic, and the clast counts and/or modal mineralogy do not reveal systematic differences. The only clarifying detail from the sandstone petrography of the Vandam volcaniclastic samples relates to sample AB0863, which is an outlier in all geochemical classifications. Compared to the other bedrock samples, AB0863 is completely devoid of calcium-rich plagioclase and has relatively low amounts of pyroxene or amphibole, instead being dominated by albite and potassium and/or alkali feldspar. This would broadly suggest that the calcium-rich plagioclase, pyroxenes, and amphiboles that are largely absent from AB0863 are important in terms of defining both of the LC-Vandam subgroups from a bulk geochemical perspective.

6.1.2 Intercomparison of Detrital Zircon and Geochemical Methods in KFTB Samples

Given the apparent divergence between provenance trends for the KFTB sandstones from geochemistry (Figs. 5 and 6) and DZ (Figs. 9 and 10), it is instructive to consider direct comparisons between these two methods. For

this purpose, we develop an approach for sample-to-sample comparison using the LDA of the geochemical data and the Bayesian population correlation of the DZ data (Fig. 11), similar to how we compared the bulk geochemistry and petrography results (Section 5.1.5). For the geochemistry-DZ comparison, we compare the first linear discriminant of LDA-1 and LDA-2 directly to the BPC value for the eastern GC volcaniclastic, GC siliciclastic, and Transcaucasus basement and LC arc sources, given that these are most diagnostic in the DZ comparison statistics we considered (e.g., Fig. 10; Fig. S16).

Comparing the LDA results and those from DZ suggests relatively little relationship between the two (Fig. 11). Specifically, sample pairs from measured sections that have a large difference in their linear discriminant value (i.e., different provenance source up section) do not necessarily have large differences in their BPC values for relevant sources. Depending on the particular DZ source considered, small trends can be observed, e.g., a positive correlation between eastern GC volcaniclastic BPC and LDA-1 and a negative correlation between GC siliciclastic BPC and LDA-1 for the Vashlovani samples, but the magnitudes of the BPC differences are small compared to differences between sections, e.g., Sarica compared to Vashlovani. This comparison also highlights a similar, and important, result from comparing the geochemical and U-Pb DZ classification of the source terranes, which is that samples can have strongly similar geochemical affinities but have different DZ sources, as is the case for the sample at the top of the Sarica section (S-1735) and the two Vashlovani samples (V-15 and V-1240) (Fig. 11).

6.1.3 Mechanism for Provenance Method Divergence

While there are important nuances as discussed in the prior sections (sections 6.1.1 and 6.1.2), broadly, the comparisons between the bulk geochemistry and DZ U-Pb geochronology from samples of both known (i.e., source areas) and unknown provenance (i.e., the KFTB sandstones) suggest that the two provenance methods indicate a potentially different history of sourcing for KFTB sandstones. Specifically, in terms of bulk geochemistry, most of the locations exhibit an up-section shift from a predominantly LC-Vandam source to a more GC interior–dominated source. In contrast, the DZ analyses from the top and bottom of select sections do not as clearly or consistently show significant changes up section (Figs. 9 and 10; Fig. S16). There are several possible explanations for this disagreement, including (1) sediment recycling and selective weathering within the foreland basin; (2) climatically mediated preferential weathering of unstable components; (3) the non-unique source characterizations via different methods described in the previous sections (sections 6.1.1 and 6.1.2); (4) sensitivity of different provenance methods to different components within the samples; or (5) biasing of DZ signatures by spatially variable erosion, fertility of source terranes, or other filtering processes. The following discusses the first option, which we favor as the primary explanation because the other four options do not fit with the available data, as explained in the Supplemental Material (Section S3). In exploring the cause of the apparent discrepancy, we largely focus on understanding the variation in the Sarica section because it is the most extreme.

In detail, our preferred explanation is that the provenance signatures largely reflect an up-section increase in sediment recycling, such that the sediment source transitions from first-cycle (or initially less-recycled) material eroded from the GC to increasing fractions of recycled versions of this same material as the KFTB developed. Of particular importance is that the primary components that appear to define the LC-Vandam source mineralogically and geochemically, e.g., calcium-rich plagioclase, pyroxene, and amphibole (Fig. 7; Fig. S8), are also species that are expected to weather at rates several orders of magnitude faster than components that define the flysch source, e.g., quartz (e.g., Lasaga et al., 1994, and references therein). The potential importance of chemical weathering of these components is also consistent with prior work in the GC region, where Morton et al. (2003) highlighted the importance of dissolution of clinopyroxene and amphiboles in Productive Series sediments in terms of considering potential sourcing. Thus, in the Sarica section, we envision a scenario where the base of the section was deposited prior to fold-thrust development and was sourced from the GC with a mixture of both GC interior and LC-Vandam sources, although the DZ data indicate the LC-Vandam–type source likely dominated, which is a point we return to in Section 6.2. As portions of the fold-thrust belt north of the Sarica section began to deform, they progressively became a source of recycled sediment for the Sarica region. Specifically, early thrusts within the KFTB exposed rocks of a similar provenance to what is seen at the base of the Sarica section, causing them to be weathered, eroded, and transported prior to deposition at the site of the Sarica section and resulting in the preferential breakdown of the unstable components that are particularly indicative of the volcanic and volcaniclastic source in the geochemical and/or petrographic data. As a result, fewer of these volcanic and volcaniclastic components are preserved up section, resulting in the up-section shift in geochemical signatures that is mirrored in the petrography (e.g., Fig. 7; Fig. S8). However, the zircon signature from these recycled sediments remains effectively the same as that of the original source material from the GC. Additionally, growth of KFTB topography to the north of Sarica would likely have begun diverting GC-sourced rivers, limiting influx of new DZ into the section. This explanation is also broadly consistent with the up-section increases in chemical index of alteration (CIA; see Sections S2.2.3 and S2.2.5 in the Supplemental Material) values seen in the Sarica section and the majority of the other sections, although the CIA values do not suggest deep weathering even at their most extreme (Fig. 6; Fig. S12). Because sandstone petrography and geochemistry data from the Xocashen and Goy sections exhibit similar up-section trends as the Sarica section, we infer they also record recycling and a transition from a GC source to one that is more locally derived from within the KFTB. However, without comparable DZ data from the Xocashen or Goy sections, this hypothesis is less definitive and highlights a need for future work.

While we argue that sediment recycling is important for interpreting the provenance signature in the majority of our KFTB sections, it may not be

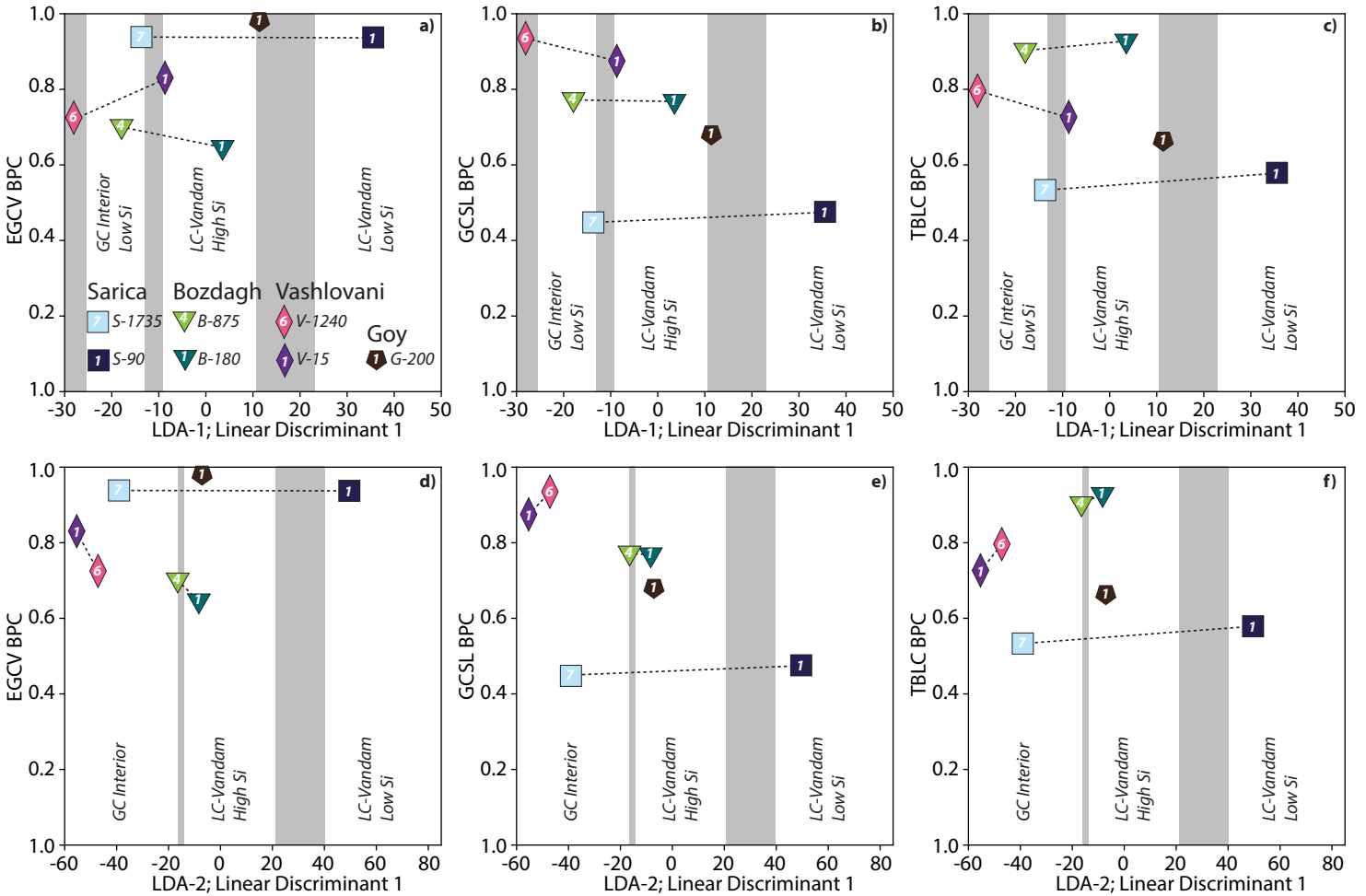

Figure 11. Comparisons between linear discriminant analyses (LDAs) of bulk geochemistry and Bayesian population correlation (BPC) of detrital zircon populations. Shown is comparison of linear discriminant 1 from analysis LDA-1 (panels A–C) or LDA-2 (panels D–F) with BPCs from eastern Greater Caucasus (GC) volcaniclastic source (EGCV) (A, D), GC siliciclastic source (GCSL) (B, E), and Transcaucasus basement and Lesser Caucasus (LC) arc source (TBLC) (C, F). We consider BPC values for EGCV, GCSL, and TBLC sources because these are the best represented in Kura Fold-Thrust Belt sandstones. For each example, vertical gray bars mark range covered by the relevant decision boundaries within the first linear discriminant (see Fig. 6 and Fig. S13, text footnote 1).

dominant in all sections, as indicated by minimal apparent provenance discrepancies between geochemical and DZ methods. In particular, we interpret both the Bozdagh and Vashlovani sections to reflect limited recycling. For Bozdagh, geochemistry, sandstone petrography, and U-Pb DZ populations all combine to indicate a similar history of sourcing and no change in the degree of recycling, consistent with the relatively constant CIA values throughout the section (Figs. 6, 9, and 10). Likewise, we interpret the Vashlovani section as recording minimal changes in the degree of recycling because in this case the geochemical and DZ data both indicate a change up section that reflects a progressively diminishing LC-Vandam source. These observations from Bozdagh and Vashlovani are a major reason why we prefer sediment recycling as the mechanism to explain the apparent discrepancies in provenance data as opposed to a climatically mediated, regional increase in chemical weathering rates (i.e., the second option listed near the beginning of this section) because this latter option predicts up-section changes in the Bozdagh and Vashlovani sections that we do not observe.

6.2 Implications for Greater Caucasus and Kura Fold-Thrust Belt Tectonics

To provide a framework within which to consider the evolution of sediment provenance in the KFTB, Figure 12 presents a visualization of changes in sourcing through time and space. For this purpose, we consider the spatial distribution of indicators of sediment provenance during individual regional stages between the Meotian and Bakunian, integrating additional DZ samples from Tye et al. (2020) where relevant. For each time period in Figure 12 and for each section that has data for that time period, we show the relevant portion of the LDA classification (bars; Fig. 6) and the dominant DZ sources (stars; Fig. 10; Fig. S16). None of the samples from Tye et al. (2020) appear within the map area of Figure 12, but we show what DZ provenance is indicated for samples either west or east along strike within the KFTB at relevant time periods. Where appropriate, we consider the degree of BPC similarity between KFTB samples from this study and those from prior work (see Section S2.3.3 and Fig. S17 in the Supplemental Material, footnote 1). Below, we summarize our preferred interpretation of the implications of the provenance for GC and KFTB tectonics, with a focus on the across-strike traverse of sections from Sarica, Xocashen, and Bozdagh (Fig. 12).

6.2.1 Meotian–Pontian (7.65–5.33 Ma)

Vashlovani is the only location within our measured sections that includes a record of the Meotian–Pontian. This portion of the Vashlovani section records a mixed GC interior and LC-Vandam source, specifically with a DZ signature that reflects a mixture of the eastern GC volcaniclastics, GC siliciclastics, and GC basement. There is some indication of a potential up-section reduction of the LC-Vandam component during Meotian–Pontian time from the petrography and geochemistry. At present, exposures of volcanic or volcaniclastic rock are very limited along the GC range front directly north of the Vashlovani section (Fig. 1). Abundant volcanic and volcaniclastic sources during deposition of the Vashlovani base may indicate that exposures of these volcanic and volcaniclastic rocks were larger during Meotian–Pontian time than at present or that concentrations of volcanic and volcaniclastic components were enhanced via either focused erosion of units with similar exposure as today or lateral transport from areas of the GC range front that expose more of these units.

Outside of the sections, at the western (sample CF-2 from Tye et al., 2020) and eastern (sample EF-5 from Tye et al., 2020) tips of the KFTB, undifferentiated Meotian–Pontian and Pontian sediments, respectively, record a predominantly GC interior source with a GC siliciclastic DZ signature during this time period (Tye et al., 2020). Without a clear sense of where, stratigraphically, CF-2 is located with respect to the Meotian–Pontian samples within the Vashlovani section, it is difficult to compare the implications of the differences between the sourcing of this sample and those of the Vashlovani section, but EF-5, given its Pontian depositional age, suggests a more exclusively GC interior–type source compared to Vashlovani during the same approximate time period. At the western terminus of the KFTB and considering Tye et al. (2020) sample CF-1 from the middle Miocene, which precedes the Meotian–Pontian, we see a potentially similar up-section change from a more LC-Vandam source (CF-1) to more GC interior–dominated source (CF-2) (Tye et al., 2020). Importantly, however, based on BPCs presented by Tye et al. (2020), CF-1 seems more similar to an LC (Transcaucasus basement and LC arc)–derived source than either of the GC volcanic or volcaniclastic DZ sources (i.e., the eastern and western GC volcaniclastics). Tye et al. (2020) suggested that the presence of an LC-affiliated source in CF-1 reflects material that was deposited more distally to the GC, with the present position resulting from subsequent translation toward the GC via north-directed underthrusting of Kura Basin lithosphere beneath the GC. This remains a viable and likely hypothesis. However, given the clear geochemical relationships between the LC volcanics and volcaniclastics and those exposed at least in the eastern GC (e.g., Fig. 4; Fig. S8), an alternative hypothesis is that there was sufficient variability in a formerly larger thrust slice of volcanic and volcaniclastic material within the GC range front that zircons sourced from this thrust sheet could in part look more like those preserved in the surficial LC today. While speculative, the general expectation of a shared tectonic history between the Jurassic–Cretaceous volcanic and volcaniclastic rocks exposed in the modern LC and the modern southern GC (Kopp and Shcherba, 1985) opens the possibility that a more complete section of the LC arc–Vandam rocks might contain larger age suites than in the tectonically isolated, and geographically separated, sections we observe today. More detailed stratigraphy in the region around the Gombori Range, specifically paleocurrent measurements, could help to differentiate these two mechanisms: i.e., do the strata from which the CF-1 sample comes record dominantly south-directed (GC sourced) or north-directed (LC sourced)

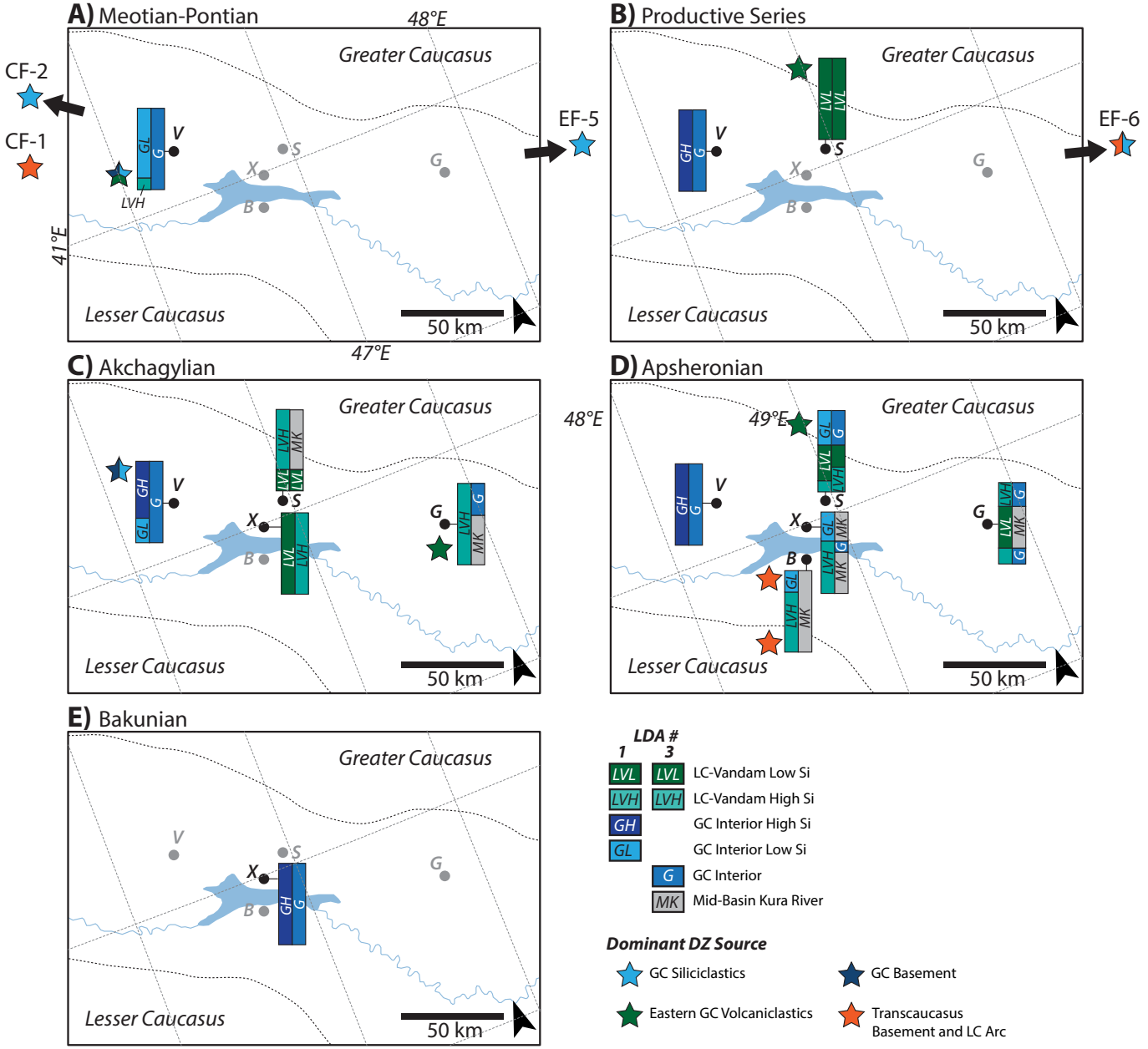

Figure 12. Summary of provenance changes through time and space as indicated by both geochemistry and detrital zircons during Meotian–Pontian (A), Productive Series (B), Akchagylian (C), Apsheronian (D), and Bakunian (E) stages. Vertical colored columns for each section represent the two possible interpretations of provenance from the linear discriminant analysis (LDA) classification of trace element geochemistry for the portion of the stratigraphy within a given time period. Stars indicate detrital zircon (DZ) samples, either from the measured sections (those adjacent to LDA results) or from areas further afield within the Kura Fold-Thrust Belt (KFTB) from Tye et al. (2020). See explanation at bottom right for correspondence between colors and sources; stars containing more than one color indicate inferred mixed sources. Map is focused on central KFTB samples and sections, but results from samples from Tye et al. (2020) outside of this region are shown schematically, with original sample names from Tye et al. (2020) above each. Grayed-out section locations indicate lack of data for that time period from that section. Note that this map is not palinspastic and does not reflect that the distances between sections and the Greater Caucasus (GC) or Lesser Caucasus (LC) range fronts would have been different at time of deposition. Section abbreviations: V—Vashlovani; B—Bozdagh; X—Xocashen; S—Sarica; G—Goy.

paleocurrents? Similarly, a better sense of the volcanic stratigraphy within the Jurassic and Cretaceous LC could provide an indication of whether there are regions characterized by single-age DZ peaks, similar to the volcanic and volcaniclastic sources within the GC.

Deposition in the Vashlovani section and elsewhere during the Meotian–Pontian (~7–5.5 Ma) is coincident with increases in exhumation rate observed throughout the GC between ~10 and 5 Ma (e.g., Avdeev and Niemi, 2011; Vincent et al., 2020; Forte et al., 2022; Tye et al., 2022). This similarity of timing is broadly consistent with the idea that the onset of rapid exhumation of the GC prior to the Meotian–Pontian had established the GC as a dominant sediment source for regions within the southern foreland (e.g., Tye et al., 2020).

6.2.2 Productive Series (5.33–2.95 Ma or 2.7 Ma)

Both the Vashlovani and Sarica sections preserve portions of the Productive Series, but they suggest relatively different sourcing at this time (Fig. 12B). Vashlovani records a dominantly GC interior source with some limited LC-Vandam input remaining. In contrast, Sarica is almost exclusively sourced from an LC-Vandam source with an eastern GC volcanic DZ signature. Present-day catchments north of Sarica within the GC reflect mixtures of the volcanic and flysch bedrock, so the dominance of LC-Vandam input in the Productive Series within the Sarica section appears to require greater proportions of this source at the time of deposition than is seen today, similar to the lower part of the Vashlovani section. Again, explanations for this pattern are either a physically larger exposure of the volcanic and volcaniclastic source within the southern range front at the longitude of Sarica, enhanced erosion of this source during Productive Series time, or lateral transport from an area of the GC range front with larger exposures of volcanic rocks.

Near the eastern terminus of the KFTB, Productive Series sample EF-6 from Tye et al. (2020) records a mixed affinity with both LC (Transcaucasus basement and LC arc) and GC (GC siliciclastic) DZ sources, but here we consider whether EF-6, like its central KFTB counterparts, might instead reflect sourcing from the GC, not the LC. Tye et al. (2020) interpreted the Transcaucasus basement and LC arc component to reflect eastward transport of LC material, either directly from the LC via an axial drainage or from erosion of Kura Basin sediments, most likely related to the coincident draw down of the Caspian Sea (e.g., Popov et al., 2006, 2010; Krijgsman et al., 2010; Forte and Cowgill, 2013; van Baak et al., 2017) and resulting incision by the Kura River (e.g., Kroonenberg et al., 2005). However, at present, both the Vashlovani and Sarica sections are at a greater distance from the GC range front than EF-6 (e.g., Figs. 1 and 12), and thus it is strange that EF-6 would reflect transport from the LC or incised Kura Basin sediments while both Vashlovani and Sarica were dominantly sourced from the GC at this same time. Tye et al. (2020) largely followed suggestions from Morton et al. (2003) of a paleo–Kura River almost exclusively sourced from the LC and that was located relatively near the GC range front, but this contradicts evidence of an entrenched Kura paleocanyon near the modern axis of the basin during Productive Series time (e.g., Kroonenberg et al., 2005). In detail, the interpretation of a LC source for eastern Kura Basin Productive Series sandstones from Morton et al. (2003) relies primarily on the presence of unstable components within the heavy mineral assemblages of these samples, including abundant clinopyroxene, amphibole, and epidote. The similarity between these assemblages and the Productive Series sandstones sourced from the modern and paleo–Kura River led Morton et al. (2003) to argue that the Productive Series sandstones necessarily must be sourced from the LC. Morton et al. (2003) did report heavy mineral assemblages from rivers draining the eastern tip of the GC that contain significant proportions of amphibole, epidote, and clinopyroxene but in lesser amounts than in the modern Kura River, with more stable minerals (e.g., feldspar and quartz) dominating the extreme eastern GC assemblages. Morton et al. (2003) attributed the higher abundance of stable minerals in the GC rivers to the presence of Jurassic and Cretaceous sediments within the catchments and suggested that the presence of the unstable minerals may be due to recycling of paleo-Kura–sourced Productive Series sediments from portions of the river catchments containing these rocks. However, our analysis suggests that the Vandam domain of the southeastern GC proper also may contribute to these heavy mineral assemblages indicative of more mafic, less evolved source terranes, and as such, the underlying association of these unstable components necessarily with a LC source, at least on the basis of heavy minerals alone, is questionable.

To fully reconcile the apparently contradictory results of a potential sourcing of central KFTB sandstones during Productive Series time from the southern margin of the GC coincident with eastern KFTB sandstones from the LC would require (1) palinspastic restoration of the positions of the Sarica section, Vashlovani section, and sample EF-6 locations during Productive Series time—in turn requiring estimates of shortening within the respective regions of the GC and KFTB; (2) constraint on the location of the GC range front along strike during Productive Series time; and (3) ideally some independent constraint on the first-order drainage-network structure within the foreland basin during Productive Series time beyond the location of the trunk Kura River. Generally, none of these details are sufficiently constrained to fully resolve this question. However, we again highlight that larger-than-present exposures of a former volcanic and volcaniclastic source in the GC with more zircon age variability than observed today provides an alternative and parsimonious explanation for the provenance records from EF-6.

Focusing on the Sarica and Vashlovani sections, we interpret the dominance of GC provenance and the coarseness of the Productive Series deposits to have resulted from continued rapid exhumation of the GC and progradation of coarse clastic materials into the foreland basin (e.g., Burbank et al., 1988; Allen and Heller, 2012). The depositional character of these deposits also likely reflects the regional context of the coincident Caspian Sea lowstand (e.g., Forte et al., 2015a). The one Productive Series sample from Vashlovani is notable for being largely devoid of lithic grains (Figs. S8 and S9) and a temporary increase in CIA (Fig. 6), both of which are consistent with an increase in reworking or

weathering. This could reflect local reworking resultant from deformation and uplift of Kura Basin sediments, i.e., initiation of the KFTB, but given that these changes are short lived and that overlying basal Akchagylian sediments look very similar to underlying upper Meotian–Pontian sediments in the Vashlovani section (e.g., Fig. 6; Figs. S8 and S9), we favor an explanation related to the unique Caspian low-stand during the Productive Series deposition and potentially increased weathering during this period.

6.2.3 Akchagylian (2.7 Ma or 2.95–2.1 Ma)

The Akchagylian is represented in the Vashlovani, Sarica, Xocashen, and Goy sections (Fig. 12C). With the exception of Vashlovani, all sections show a strong affinity for the LC-Vandam source near their base and with Goy specifically showing affinity to an eastern GC volcaniclastic DZ source. In both the Sarica and Goy sections, up section toward the Apsheronian boundary, there is a slight decrease in this LC-Vandam source as indicated by petrography and geochemistry. This is not seen within the Xocashen section, but the Akchagylian-Apsheronian boundary is not captured within our sampled stratigraphy there. Similar to other sections, the base of the Goy section shows a strong affinity with a LC-Vandam source both geochemically (Fig. 6; Fig. S11) and in terms of DZ (Figs. 9 and 10; Fig. S16), which is at odds with modern geology because the portion of the GC range front north of Goy is an embayment largely devoid of volcanic and volcaniclastic material. As noted above, possible explanations for this difference are larger past exposures of the volcanic and volcaniclastic source within the southern range front, enhanced erosion of this source during Akchagylian time, or lateral transport from an area of the GC range front with larger exposures of volcanic rocks.

In the Sarica section, a marked decrease in LC-Vandam components that is especially noticeable in the sandstone petrography (Fig. S8) but also detected geochemically (Fig. 6; Fig. S11) could reflect either (1) a decrease in the contribution of volcanic and volcaniclastic inputs reflecting a decrease in the importance of this source within the GC at the longitude of Sarica, or (2) the beginning of sediment recycling reflective of initiation of KFTB structures north of Sarica and reduction in the volcanic and volcaniclastic component through weathering of unstable phases as described previously (section 6.1.3). Presumably, DZ ages from this horizon would help to constrain these options; i.e., if the DZ signature remained dominated by eastern GC volcaniclastic zircons, this would suggest sediment recycling, whereas if the DZ signature began to reflect more GC siliciclastic or other non-volcanic GC inputs, this would support a decreasing extent of an eastern GC volcaniclastic source along the southern range front. In the absence of such data, we instead consider the regional tectonic context of the KFTB to help narrow the options. Farther west within the KFTB, the Akchagylian may reflect the initiation of deformation (e.g., Sukhishvili et al., 2021), but the potential time range also includes much of the Apsheronian (e.g., Fig. 2). Similarly, the Vashlovani section during the Akchagylian, which is in a somewhat similar structural position within the KFTB as Sarica, seems to still record sourcing from the GC as opposed to more local KFTB, i.e., recycled GC, sources. This is exemplified by the geochemistry (Fig. 6; Fig. S11) and DZ (Fig. 9 and 10; Fig. S16) sample(s) from the Akchagylian reflecting a consistent change up section to a reduced LC-Vandam input and sandstone petrography that still suggests LC-Vandam clastic inputs (Fig. 4). Thus, for Sarica, we favor an explanation for provenance during the Akchagylian that the section still recorded sourcing primarily from the GC. This would imply that the timing of KFTB initiation at the longitude of Sarica likely occurred after the Akchagylian and that the change in provenance from the Productive Series to the Akchagylian reflects a reduction in flux of the LC-Vandam source area from the GC.

6.2.4 Apsheronian (2.1–0.8 Ma) and Bakunian

The Apsheronian is represented in all measured sections (Fig. 12D), though the extent of its exposure in the Vashlovani section is uncertain considering the unclear boundary between the Akchagylian and Apsheronian in this location (Fig. 2). Through the duration of the Apsheronian, geochemistry and sandstone petrography suggest that the Sarica, Xocashen, and Bozdagh sections all show decreases in LC-Vandam components. This is also broadly coincident with an up-section coarsening in all three columns. However, in the Xocashen section, much of that coarsening occurs after the Apsheronian, during the Bakunian period, and the coarsening in the Bozdagh section is not as pronounced as in the other two sections. For both Sarica and Xocashen, we interpret these up-section changes in the stratigraphic character as most likely reflecting initiation of the KFTB. For Sarica, this would suggest that structures north of the section location likely began to exhume sometime during the early Apsheronian (unit S3; Fig. 2) or possibly across the Akchagylian-Apsheronian boundary, similar to the timing of initiation of deformation in the Goy region (Forte et al., 2013; Lazarev et al., 2019). For Xocashen, coarsening and reduction in the LC-Vandam–associated component occurred later in the Apsheronian and/or into the Bakunian compared to Sarica. This later timing in the Xocashen section could reflect either a delay related to coarse clastic progradation or that the Sarica fold itself, which is the structure directly north of and across the Adjinour playa from Xocashen, initiated and began to exhume, providing material for southern regions. In the latter case, this would suggest in-sequence propagation, from the structure north of Sarica during the early Apsheronian followed by Sarica during the later Apsheronian and into the Bakunian (Fig. 13).

It is worth noting that the degree of synchronicity of significant up-section coarsening and the reduction in the LC-Vandam component vary between the Xocashen and Sarica sections. The two events roughly correspond at Xocashen, i.e., across the unit X2-X3 or Apsheronian-Bakunian boundary (Fig. 2); however, at Sarica, the coarsening starts across the unit S3-S4 boundary (roughly early to middle Apsheronian) whereas the reduction in the LC-Vandam component occurs closer to the unit S4-S5 boundary (later Apsheronian). For Sarica, it

is unclear if the up-section coarsening or the LC-Vandam reduction better times the initiation of structures within the KFTB to the north. We favor up-section coarsening as being most diagnostic of thrust-belt initiation because we assume that the onset of significant weathering is likely to have temporally lagged behind the transition to coarse sediment arrival from the uplift of structures to the north, in which case the KFTB initiated at this longitude around the Akchagylian-Apsheronian boundary (~2.1 Ma). However, if the reduction in the LC-Vandam component more precisely dates initiation, then onset here is closer to ~1 Ma. Ultimately, distinguishing between these options likely requires additional DZ geochronology within the Sarica section, additional stratigraphic observations of areas within the KFTB north of Sarica, and more precise chronologies of all strata.

While the Bozdagh section shows a reduction in LC-Vandam source components and a slight coarsening upwards, the interpretation of a relatively constant deltaic environment with Transcaucasus basement and LC arc DZ signatures at both the top and bottom of the section do not further constrain KFTB initiation. Instead, we interpret the facies and provenance data to indicate that the Bozdagh section was likely sourced by an east-flowing, longitudinal river that drains both the GC and LC, analogous to the modern Kura River or other present-day axial rivers (Fig. 12). Thus, we interpret the reduction up section of the LC-Vandam component at Bozdagh as likely reflecting an overall reduction in the exposed area of volcanic and volcaniclastic sources in the GC. From paleocurrent data at the western terminus of the KFTB, we know that the development of the KFTB during the Akchagylian–Apsheronian period significantly perturbed the foreland drainage network, given that formerly south-flowing rivers were locally defeated and reversed to drain northwards into the piggyback Alazani Basin (Sukhishvili et al., 2021). Thus, if Bozdagh represents a paleo-Kura-like drainage, then the up-section changes in provenance in the Bozdagh section could also reflect progressive sequestering in the KFTB and nascent Alazani Basin of material derived from the southeastern GC during the Apsheronian.

Finally, in the Goy section, the angular unconformity between Akchagylian and Apsheronian sediments is thought to date the timing of initiation in the KFTB at this longitude (Forte et al., 2013; Lazarev et al., 2019). By the base of the Apsheronian, the provenance of Goy appears to have been dominated by GC interior sources, though coupled with the coarsening upward seen from unit G2-A to G2-B and unit G3 in Lazarev et al. (2019), the independent constraint on the KFTB having initiated by that time suggests the up-section change in the apparent sourcing from geochemistry could also be a recycling signature. DZ data from higher in the Goy section would likely clarify whether this is the case.

6.2.5 Summary of Tectonic Implications from Provenance

In Figure 13, we summarize our preferred sequence of events within the central KFTB at the longitude of the Sarica, Xocashen, and Bozdagh sections and based on our new provenance data and prior work. During Productive Series time, the southern range front of the eastern GC exposed a mixture of thrust-bounded sections of volcanic and volcaniclastic rocks that likely reflect slices of distal LC arc material, overlain by and in thrust contact with GC flysch (Fig. 13A). We hypothesize that at this time, the range-front fault thrusting Mesozoic volcanic rocks over Cenozoic basin fill was the primary active structure in the range, prior to the development of the KFTB. We further infer that the

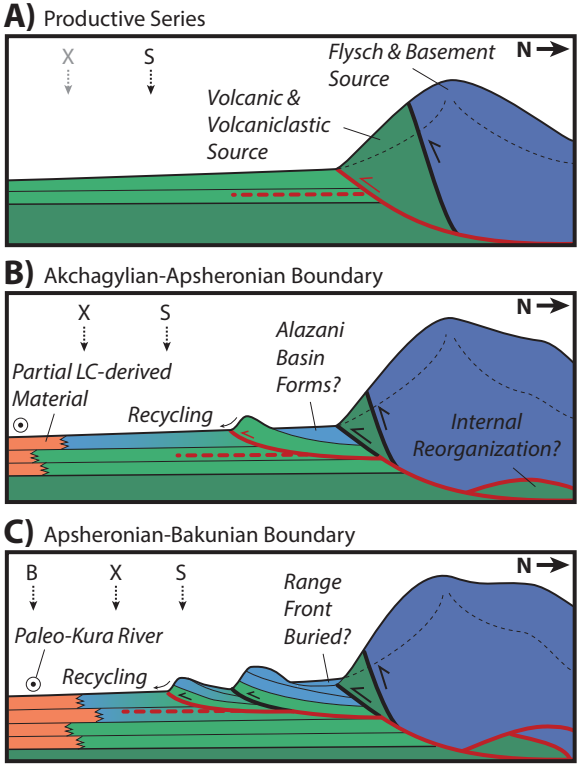

Figure 13. Schematic cross sections through central Kura Fold-Thrust Belt (KFTB) during Productive Series stage (A), at Akchagylian-Apsheronian boundary (B), and at Apsheronian-Bakunian boundary (C). Approximate locations of Bozdagh (B), Xocashen (X), and Sarica (S) measured sections are shown. Diagram is not to scale, but we schematically depict advection of sections toward the Greater Caucasus (GC) via continued underthrusting and reduction in distance between sections as KFTB structures initiated and accommodated shortening. Grayed-out section locations indicate there are no data for that time from that section. Blue colors indicate flysch sources or stratigraphy that appears to be sourced from flysch, green colors indicate volcanic and/or volcaniclastic sources, and orange indicates sourcing from mixed GC and Lesser Caucasus (LC) as seen in Bozdagh section or modern Kura River. Concentric circle indicates approximate location of axial drainage (Kura River).

cross-strike width of volcanic and volcaniclastic rocks along the southeastern range front of the GC was wider at this time than it is today. This model does not preclude other structures from being active at the time, and our data do not directly constraint the history of any of the individual structures within the GC, but the localization of deformation near the range front is consistent with in-sequence propagation of structures and the subsequent evolution of the system as we interpret below from the provenance data.

By the time of the Akchagylian-Apsheronian boundary (Fig. 13B), exposure of the volcanic and volcaniclastic rocks had progressively decreased as the thrust slice(s) that contained these rocks were exhumed and eroded via south-directed thrusting along the range-front fault system(s). On the basis of the provenance and stratigraphy, it is at this time, i.e., ~2.1 Ma, that we suggest deformation began to propagate into the foreland, initiating the KFTB and formation of the Alazani piggyback basin (Fig. 13B). However, as discussed in Section 6.2.4, we acknowledge that available data do not precisely constrain the timing of initiation of the central KFTB and that onset could be younger and closer to ~1 Ma. We favor the interpretation of an initiation age closer to ~2 Ma because we generally assume that coarse sediment arrival from the uplift of structures to the north of Sarica would have preceded significant weathering and associated reduction of the LC-Vandam component of this material. However, clarifying the timing within the central KFTB should be a priority in future work. Our preferred interpretation of an ~2.1 Ma initiation for the central KFTB implies broadly synchronous timing for KFTB initiation along strike, with Akchagylian to basal Apsheronian initiation at the longitude of Sarica, Xocashen, and Bozdagh matching KFTB initiation estimated both to the west (Sukhishvili et al., 2021) and east (Forte et al., 2013; Lazarev et al., 2019). Synchronous initiation along strike is contrary to previous suggestions of east-younging diachronous initiation that was inferred from sparse data (e.g., Forte et al., 2010). Based on recent comparisons of low-temperature thermochronology and ^{10}Be exhumation rates (Forte et al., 2022), Akchagylian to basal Apsheronian initiation of the KFTB would have been coincident with a larger structural reorganization within the range that caused deformation within the interior of the GC to expand to the north, possibly related to duplexing at depth along the basal GC thrust system (Forte et al., 2015b). In addition, initiation of the KFTB likely resulted in initial slowing of activity on the range-front fault system and the onset of increasing embayment of the range front via erosion and burial as the Alazani piggyback basin began to fill (e.g., Forte et al., 2010; Mosar et al., 2010).

By the time of the boundary between the Apsheronian and Bakunian stages (Fig. 13C), we infer that the Sarica fold itself likely began to form, shedding coarser grained and further-recycled material southward to be deposited at Xocashen (Fig. 13C). Such timing implies in-sequence propagation of the KFTB at this longitude, which contrasts with the out-of-sequence propagation seen in portions of the eastern terminus of the belt (Forte et al., 2013) and GC (Tye et al., 2022). Throughout the depositional history, we suggest that Bozdagh experienced deposition from a paleo-Kura River–like axial drainage. This axial drainage subsequently entrenched between the Bozdagh and Xocashen folds sometime during the Bakunian stage or later, when both the Xocashen and Bozdagh folds began to form, but our data do not constrain the timing of either of these structures more precisely than initiation during or after Bakunian time.

Ultimately, our preferred sequence of events within the KFTB is consistent with recent work suggestive of approximately synchronous initiation of the KFTB along strike (Forte et al., 2013; Lazarev et al., 2019; Sukhishvili et al., 2021) and thus is consistent, at least in a structural sense, with widening of the orogen in response to a regional shift to more arid conditions (Whipple and Meade, 2004, 2006; Forte et al., 2013). However, it remains unclear whether a climatically induced widening also explains the potentially coincident internal structural reorganization and northward shift of the locus of exhumation within the GC (Fig. 13; e.g., Forte et al., 2015b, 2022). Internal deformation within the orogen coincident with widening is not an unexpected response to either changes in taper angle (e.g., Whipple and Meade, 2004, 2006; Hoth et al., 2006) or as part of accretion cycles (e.g., Hoth et al., 2007), but establishing the coincidence of KFTB initiation and internal GC reorganization requires better timing of both, especially the internal reorganization. Remaining uncertainty in the exact timing of initiation of the central KFTB structures along the traverse between Sarica and Bozdagh could be reduced via infilling the DZ geochronology record.

Our results highlight that multiproxy sediment provenance work, paired with additional stratigraphic and structural characterization of regions within the KFTB, may be a viable method for constraining the timing of initiation throughout the thrust belt. Such additional timing information is important for clarifying the drivers of fold-thrust belt initiation and deformation front expansion within the GC. In contrast, tying the structural changes to a potential climatic trigger for initiation requires more paleoclimatic context for the KFTB sediments.

6.3 Implications for Provenance Studies in Forelands

Broadly, results of our work provide some general insights for sediment provenance investigations within other foreland fold-thrust belts. DZ U-Pb geochronology is unquestionably a preferred method for sediment provenance investigations across a range of tectonic settings (e.g., Gehrels, 2014; Žák et al., 2020; Jian et al., 2022). However, this method is not without challenges in terms of uniquely interpreting the provenance history while accounting for sources of bias or other complications (e.g., Cawood et al., 2003; Amidon et al., 2005; Andersen, 2005; Link et al., 2005; Lawrence et al., 2011; Raines et al., 2013; Spencer et al., 2018; Malkowski et al., 2019). The results of our analysis echo those of other recent work (e.g., Malkowski et al., 2019), namely that interpretation of DZ geochronology is the most robust when done in concert with other indicators of sediment provenance. In our particular example, the inclusion of bulk rock geochemistry and sandstone petrography is critical for recognizing the potential role of sediment recycling within the KFTB. Furthermore, exploring mechanisms to reconcile the apparent discrepancies between

the geochemical and/or petrographic data and the DZ results leads to insights regarding the timing of onset of sediment recycling and thus initiation of the KFTB, insights that are not apparent from DZ U-Pb populations alone.

One of the reasons for the propagation of DZ as an effectively default provenance method, beyond the ubiquity and durability of zircons in many sediments, is the relative ease and low cost of the analyses (e.g., Gehrels, 2012). In this respect, we emphasize that bulk rock geochemistry of either the same sandstone samples used for DZ geochronology, as we present here, and/or interbedded mudstones (e.g., Pe-Piper et al., 2008; Malkowski et al., 2019) represents a similarly easy and cost-effective provenance technique that pairs well with DZ geochronology. Simultaneous application of both techniques has the potential to reveal additional details regarding the provenance and interpreted tectonic history of a region, as our study demonstrates.

7. CONCLUSIONS

The results of our multiproxy provenance analysis of Kura Fold-Thrust Belt (KFTB) sandstones and potential source regions within the Greater Caucasus (GC) and Lesser Caucasus (LC) provide additional context and considerations for future provenance work within the Kura Basin or KFTB. In addition, these data help to clarify the structural evolution of both the southeastern GC and KFTB and specifically add weight to the suggestion from some prior work that initiation of the KFTB may have been nearly synchronous along strike. Specific notable conclusions from this work include:

(1) Source characterization and thus resulting indications of sediment provenance within the foreland from sandstone petrography, bulk major and trace element geochemistry, and detrital zircon (DZ) geochronology broadly overlap but have some important differences. Source terranes defined on the basis of geochemistry or framework grains span geographically broader regions than those defined by DZ populations. Specifically, while prior work characterizing DZ source terranes identifies seven distinct sources within the Caucasus region (of which five represent a source from the GC, one represents a source from the LC and Transcaucasus, and one represents a source from the East European craton), we are able to differentiate two main sources using sediment geochemistry: one that reflects sourcing from the GC interior (e.g., the basement and/or Jurassic–Cretaceous flysch) and another that reflects sourcing either from the Jurassic–Cretaceous volcanic and volcaniclastics along the southern margin of the GC or the similarly aged LC arc rocks. Both geochemical sources can be further refined into two subpopulations broadly reflective of their relative SiO_2 content, which convey information on the nuanced geology of the particular samples but are not geographically distinct.

(2) Within the KFTB sandstone samples, sandstone petrography and trace element geochemistry are broadly correlative and provide similar information with respect to potential provenance histories. This suggests that with respect to these two methods, future provenance work in the KFTB could largely focus on inclusion of bulk trace element geochemistry, which is a substantially less work-intensive methodology than sandstone petrography.

(3) Our geochemical and petrographic data indicate that the majority of KFTB sections record an up-section change in apparent provenance from a more volcanic and volcaniclastic source (i.e., the LC-Vandam source) to one more reflective of sourcing from the interior of the modern GC, which is dominated by Jurassic–Cretaceous flysch. In contrast, U-Pb ages from DZ suggest relatively minimal changes between the bottom and top of the sections and instead reveal different sourcing between the sections. We interpret that this apparent divergence between the provenance methods in part reflects an up-section increase in sediment recycling and local reworking related to initiation of structures within the belt. This implies that in part, the apparent up-section change evident in the geochemistry and petrography to a modern GC interior–like source is not real but instead reflects that after weathering of unstable components of the LC-Vandam–like source, sediments geochemically and/or petrographically appear somewhat similar to the GC interior source. In detail, while the onset of sediment recycling is captured by geochemical and petrographic data, the DZ data are insensitive to this change.

(4) Integrating provenance changes from the different methods suggests that before the Akchagylian-Apsheronian boundary (~2.1 Ma), a progressive up-section reduction in the volcanic and volcaniclastic component observed within the KFTB reflects a progressive decrease in the spatial extent of this source in southeastern GC. We interpret this decrease over time to reflect progressive exhumation and erosion of a thrust-bounded slice(s) of the Vandam and equivalent rocks along the range-front fault system, although other mechanisms are permitted, such as changes in the spatial distribution of focused erosion or along-strike sourcing of sediment.

(5) We interpret the diminishing volcanic and volcaniclastic component and change in grain size shortly after the Akchagylian-Apsheronian boundary to reflect the onset of KFTB deformation within the central part of the belt, where the mafic to intermediate, unstable components diagnostic of the volcanic and volcaniclastic source terranes were selectively weathered during recycling and local reworking. This implies that the initiation age of the central KFTB overlaps with timing constrained in the western and eastern termini of the belt and further indicates that the belt initiated nearly synchronously along strike. Synchronous initiation of the KFTB is consistent with the proposition that growth of the thrust belt represents a nearly synchronous, major structural reorganization and resultant widening of the GC orogen. Although this reorganization and widening could have been climatically driven, further tests of that hypothesis would benefit from both more complete regional paleoclimate records and refined timing of initiation of the belt, especially in the western section near the Gombori Range.

(6) The structural history we interpret from sediment provenance implies broadly in-sequence, north-to-south propagation of the locus of active deformation from the southeastern margin of the GC into the KFTB. Similarly, our results imply predominantly in-sequence propagation of

structures within the central KFTB as well. This differs from histories of out-of-sequence deformation in the eastern KFTB and eastern tip of the GC, highlighting diverse structural histories over relatively modest (~100 km) distances along strike.

(7) Finally, the results from the KFTB highlight the utility of integrating diverse sediment provenance methods within actively deforming regions because this may allow for better characterization of potential biases and complications that could otherwise hinder correct interpretation but also have the potential to expand the ability to recognize important drivers of provenance change.

ACKNOWLEDGMENTS

We thank Boris Avdeev, Zak Murturzayev, Tea Mumladze, Ana Menabde, David Kandelaki, Christian van Baak, and Iuliana Vasiliev for help in collecting the samples presented here. We additionally thank Tea Godoladze, Misha Elashvili, Zurab Javakhishvili, Talat Kangarli, and Ibrahim Murturzayev for assistance in accessing the field areas and general logistic support. We thank Christopher Campisano for the use of his lab facility at ASU for processing the ash samples for tephra geochemistry; Axel Wittmann for his assistance during microprobe analyses at ASU; Sarah Roeske for her assistance during microprobe analyses at University of California, Davis (UC Davis); and the staff of the Arizona LaserChron Center for their assistance during the detrital zircon analyses. We thank Charles Trexler and Alex Tye for helpful conversations regarding the provenance of sediments and their structural context within the Greater Caucasus region. Finally, we thank Associate Editor Joel Saylor, Nicholas Perez, and an anonymous reviewer for extensive comments on the manuscript. This material is based upon work originally supported by U.S. National Science Foundation (NSF) grants EAR-0810285 (Cowgill), with additional funding provided to Forte by NSF grant EAR-1450970, the UC Davis Department of Geology Cordell Durrell Fund, Geological Society of America, and American Association of Petroleum Geologists. Manuscript preparation was supported by NSF grants EAR-1524631 and EAR-2050623 (Cowgill) and EAR-1524304 and EAR-2050618 (Niemi).

REFERENCES CITED

Abdullaev, R.N., Agabekov, M.G., and Gavrilov, M.D., 1957, K-38-XXIX: Geological map of the USSR: Russian Geological Research Institute, 1:200,000.

Abdullayev, N.R., Weber, J., van Baak, C.G.C., Aliyeva, E., Leslie, C., Riley, G.W., O'Sullivan, P., and Kislitsiyn, R., 2018, Detrital zircon and apatite constraints on depositional ages, sedimentation rates and provenance: Pliocene Productive Series, South Caspian Basin, Azerbaijan: Basin Research, v. 30, p. 835–862, https://doi.org/10.1111/bre.12283.

Adamia, S., Alania, V., Chabukiani, A., Kutelia, Z., and Sadradze, N., 2011a, Greater Caucasus (Cavcasioni): A long-lived North-Tethyan back-arc basin: Turkish Journal of Earth Sciences, v. 20, p. 611–628, https://doi.org/10.3906/yer-1005-12.

Adamia, S., Zakariadze, G., Chkhotua, T., Sadradze, N., Tsereteli, N., Chabukiani, A., and Gventsade, A., 2011b, Geology of the Caucasus: A review: Turkish Journal of Earth Sciences, v. 20, p. 489–544, https://doi.org/10.3906/yer-1005-11.

Adamia, S.A., Lordkipanidze, M.B., and Zakariadze, G.S., 1977, Evolution of an active continental margin as exemplified by the alpine history of the Caucasus: Tectonophysics, v. 40, p. 183–199, https://doi.org/10.1016/0040-1951(77)90065-8.

Agabekov, M.G., Kerimov, K.M., Moshashvili, A.B., and Khain, V.Y., 1976, New data on the structure of the central part of the Kura trough: Geotectonics, v. 10, p. 350–354.

Aghayeva, V., Sachsenhofer, R.F., van Baak, C.G.C., Bayramova, S., Ćorić, S., Frühwirth, M.J., Rzayeva, E., and Vincent, S.J., 2023, Stratigraphy of the Cenozoic succession in eastern Azerbaijan: Implications for petroleum systems and paleogeography in the Caspian basin: Marine and Petroleum Geology, v. 150, https://doi.org/10.1016/j.marpetgeo.2023.106148.

Agustí, J., Vekua, A., Oms, O., Lordkipanidze, D., Bukhsianidze, M., Kiladze, G., and Rook, L., 2009, The Pliocene-Pleistocene succession of Kvabebi (Georgia) and the background to the early human occupation of Southern Caucasus: Quaternary Science Reviews, v. 28, p. 3275–3280, https://doi.org/10.1016/j.quascirev.2009.09.001.

Aitchison, J., 1986, The Statistical Analysis of Compositional Data: London, Chapman and Hall, 416 p.

Alania, V., Beridze, T., Enukidze, O., Chagelishvili, R., Lebanidze, Z., Maqadze, D., Razmadze, A., Sadradze, N., and Tevzadze, N., 2021a, The geometry of the two orogens convergence and collision zones in central Georgia: New data from seismic reflection profiles, *in* Bonali, F.L., Pasquaré Mariotto, F., and Tsereteli, N., eds., Building Knowledge for Geohazard Assessment and Management in the Caucasus and other Orogenic Regions: Dordrecht, Springer Netherlands, NATO Science for Peace and Security Series C: Environmental Security, p. 73–88, https://doi.org/10.1007/978-94-024-2046-3_6.

Alania, V., Tibaldi, A., Bonali, F.L., Enukidze, O., and Russo, E., 2021b, Structural architecture of the western Greater Caucasus orogen: New data from a crustal-scale structural cross-section, *in* Bonali, F.L., Pasquaré Mariotto, F., and Tsereteli, N., eds., Building Knowledge for Geohazard Assessment and Management in the Caucasus and other Orogenic Regions: Dordrecht, Springer Netherlands, NATO Science for Peace and Security Series C: Environmental Security, p. 59–71, https://doi.org/10.1007/978-94-024-2046-3_5.

Alania, V.M., Chabukiani, A.O., Chagelishvili, R.L., Enukidze, O.V., Gogrichiani, K.O, Razmadze, A.N., and Tsereteli, N.S., 2015, Growth structures, piggy-back basins and growth strata of the Georgian part of the Kura foreland fold-thrust belt: Implications for Late Alpine kinematic evolution, *in* Sosson, M., Stephenson, R.A., and Adamia, S.A., eds., Tectonic Evolution of the Eastern Black Sea and Caucasus: Geological Society of London Special Publication 428, p. 171–185, https://doi.org/10.1144/SP428.5.

Aliyeva, E.G.-M., 2005, Reservoirs of the lower Pliocene Productive Series at the western flank of the South Caspian Basin: Lithology and Mineral Resources, v. 40, p. 267–278, https://doi.org/10.1007/s10987-005-0027-7.

Ali-Zade, A.A., 2005, Geological Map of Azerbaijan Republic: National Academy of Sciences of Azerbaijan Republic, 1:500,000.

Allen, M., Jackson, J., and Walker, R., 2004, Late Cenozoic reorganization of the Arabia-Eurasia collision and the comparison of short-term and long-term deformation rates: Tectonics, v. 23, TC2008, https://doi.org/10.1029/2003TC001530.

Allen, M.B., Morton, A.C., Fanning, C.M., Ismail-Zadeh, A.J., and Kroonenberg, S.B., 2006, Zircon age constraints on sediment provenance in the Caspian region: Journal of the Geological Society, v. 163, p. 647–655, https://doi.org/10.1144/0016-764920-068.

Allen, P.A., and Heller, P.L., 2012, Dispersal and preservation of tectonically generated alluvial gravels in sedimentary basins, *in* Busby, C., and Azor, A., eds., Tectonics of Sedimentary Basins: Recent Advances: Chichester, UK, Blackwell Publishing, p. 111–130, https://doi.org/10.1002/9781444347166.ch6.

Amidon, W.H., Burbank, D.W., and Gehrels, G.E., 2005, Construction of detrital mineral populations: Insights from mixing of U-Pb zircon ages in Himalayan rivers: Basin Research, v. 17, p. 463–485, https://doi.org/10.1111/j.1365-2117.2005.00279.x.

Andersen, T., 2005, Detrital zircons as tracers of sedimentary provenance: Limiting conditions from statistics and numerical simulation: Chemical Geology, v. 216, p. 249–270, https://doi.org/10.1016/j.chemgeo.2004.11.013.

Avdeev, B., and Niemi, N.A., 2011, Rapid Pliocene exhumation of the central Greater Caucasus constrained by low-temperature thermochronometry: Tectonics, v. 30, TC2009, https://doi.org/10.1029/2010TC002808.

Bande, A., Horton, B.K., Ramírez, J.C., Mora, A., Parra, M., and Stockli, D.F., 2012, Clastic deposition, provenance, and sequence of Andean thrusting in the frontal Eastern Cordillera and Llanos foreland basin of Columbia: Geological Society of America Bulletin, v. 124, p. 59–76, https://doi.org/10.1130/B30412.1.

Banks, C.J., Robinson, A.G., and Williams, M.P., 1997, Structure and regional tectonics of the Achara-Trialet fold belt and the adjacent Rioni and Karli foreland basins, Republic of Georgia, *in* Robinson, A.G., ed., Regional and Petroleum Geology of the Black Sea and Surrounding Region: American Association of Petroleum Geologists Memoir 68, p. 331–346, https://doi.org/10.1306/M68612C17.

Bhatia, M.R., 1983, Plate tectonics and geochemical composition of sandstones: The Journal of Geology, v. 91, p. 611–627, https://doi.org/10.1086/628815.

Bhatia, M.R., and Crook, K.A.W., 1986, Trace element characteristics of graywackes and tectonic setting discrimination of sedimentary basins: Contributions to Mineralogy and Petrology, v. 92, p. 181–193, https://doi.org/10.1007/BF00375292.

Bonjour, J.-L., and Dabard, M.-P., 1991, Ti/Nb ratios of clastic terrigenous sediments used as an indicator of provenance: Chemical Geology, v. 91, p. 257–267, https://doi.org/10.1016/0009-2541(91)90003-A.

Burbank, D.W., Beck, R.A., Raynolds, R.G.H., Hobbs, R.S., and Tahirkheli, R.A.K., 1988, Thrusting and gravel progradation in foreland basins: A test of post-thrusting gravel dispersal: Geology, v. 16, p. 1143–1146, https://doi.org/10.1130/0091-7613(1988)016<1143:TAGPIF>2.3.CO;2.

Capaldi, T.N., Horton, B.K., McKenzie, N.R., Mackaman-Lofland, C., Stockli, D.F., Ortiz, G., and Alvarado, P., 2020, Neogene retroarc foreland basin evolution, sediment provenance, and magmatism in response to flat slab subduction, western Argentina: Tectonics, v. 39, https://doi.org/10.1029/2019TC005958.

Carrapa, B., Strecker, M.R., and Sobel, E.R., 2006, Cenozoic orogenic growth in the Central Andes: Evidence from sedimentary rock provenance and apatite fission track thermochronology in the Fiambalá Basin, southernmost Puna Plateau margin (NW Argentina): Earth and Planetary Science Letters, v. 247, p. 82–100, https://doi.org/10.1016/j.epsl.2006.04.010.

Cavazza, W., Gusmeo, T., Zattin, M., Alania, V., Enukidze, O., Corrado, S., and Schito, A., 2023, Two-step exhumation of Caucasian intraplate rifts: A proxy of sequential plate-margin collisional orogenies: Geoscience Frontiers, v. 15, https://doi.org/10.1016/j.gsf.2023.101737.

Cawood, P.A., Nemchin, A.A., Freeman, M., and Sircombe, K., 2003, Linking source and sedimentary basin: Detrital zircon record of sediment flux along a modern river system and implications for provenance studies: Earth and Planetary Science Letters, v. 210, p. 259–268, https://doi.org/10.1016/S0012-821X(03)00122-5.

Comas, M., and Thió-Henestrosa, S., 2011, CoDaPack 2.0: A stand-alone, multi-platform compositional software, *in* Egozcue, J.J., Tolosana-Delgado, R., and Ortego, M.I., eds., Proceedings of the 4th International Workshop on Compositional Data Analysis: Barcelona, International Center for Numerical Methods in Engineering.

Cowgill, E., Forte, A.M., Niemi, N.A., Avdeev, B., Tye, A., Trexler, C., Javakishvirli, Z., Elashvili, M., and Godoladze, T., 2016, Relict basin closure and crustal shortening budgets during continental collision: An example from Caucasus sediment provenance: Tectonics, v. 35, p. 2918–2947, https://doi.org/10.1002/2016TC004295.

Cowgill, E., Niemi, N.A., Forte, A.M., and Trexler, C.C., 2018, Reply to Comment by Vincent et al.: Tectonics, v. 37, p. 1017–1028, https://doi.org/10.1002/2017TC004793.

Dahlen, F.A., 1990, Critical taper model of fold-and-thrust belts and accretionary wedges: Annual Review of Earth and Planetary Sciences, v. 18, p. 55–99, https://doi.org/10.1146/annurev.ea.18.050190.000415.

Dahlen, F.A., and Suppe, J., 1988, Mechanics, growth, and erosion of mountain belts, *in* Clark, S.P., Jr., Burchfiel, B.C., and Suppe, J., eds., Processes in Continental Lithospheric Deformation: Geological Society of America Special Paper 218, p. 161–178, https://doi.org/10.1130/SPE218-p161.

Darin, M.H., and Umhoefer, P.J., 2022, Diachronous initiation of Arabia–Eurasia collision from eastern Anatolia to the southeastern Zagros Mountains since middle Eocene time: International Geology Review, v. 64, p. 2653–2681, https://doi.org/10.1080/00206814.2022.2048272.

Davis, D., Suppe, J., and Dahlen, F.A., 1983, Mechanics of fold-and-thrust belts and accretionary wedges: Journal of Geophysical Research: Solid Earth, v. 88, p. 1153–1172, https://doi.org/10.1029/JB088iB02p01153.

DeCelles, P.G., Gehrels, G.E., Quade, J., Ojha, T.P., Kapp, P.A., and Upreti, B.N., 1998, Neogene foreland basin deposits, erosional unroofing, and the kinematic history of the Himalayan fold-thrust belt, western Nepal: Geological Society of America Bulletin, v. 110, p. 2–21, https://doi.org/10.1130/0016-7606(1998)110<0002:NFBDEU>2.3.CO;2.

Dhont, D., and Chorowicz, J., 2006, Review of the neotectonics of the Eastern Turkish-Armenian Plateau by geomorphic analysis of digital elevation model imagery: International Journal of Earth Sciences, v. 95, p. 34–49, https://doi.org/10.1007/s00531-005-0020-3.

Dickinson, W.R., 1970, Interpreting detrital modes of graywacke and arkose: Journal of Sedimentary Petrology, v. 40, p. 695–707, https://doi.org/10.1306/74D72018-2B21-11D7-8648000102C1865D.

Dickinson, W.R., and Suczek, C.A., 1979, Plate tectonics and sandstone compositions: American Association of Petroleum Geologists Bulletin, v. 63, p. 2164–2182, https://doi.org/10.1306/2F9188FB-16CE-11D7-8645000102C1865D.

Egozcue, J.J., and Pawlowsky-Glahn, V., 2005, Groups of parts and their balances in compositional data analysis: Mathematical Geology, v. 37, p. 795–828, https://doi.org/10.1007/s11004-005-7381-9.

Egozcue, J.J., Pawlowsky-Glahn, V., Mateu-Figueras, G., and Barceló-Vidal, C., 2003, Isometric logratio transformations for compositional data analysis: Mathematical Geology, v. 35, p. 279–300, https://doi.org/10.1023/A:1023818214614.

Fedo, C.M., Nesbitt, H.W., and Young, G.M., 1995, Unraveling the effects of potassium metasomatism in sedimentary rocks and paleosols, with implications for paleoweathering conditions and provenance: Geology, v. 23, p. 921–924, https://doi.org/10.1130/0091-7613(1995)023<0921:UTEOPM>2.3.CO;2.

Fedo, C.M., Sircombe, K.N., and Rainbird, R.H., 2003, Detrital zircon analysis of the sedimentary record, *in* Hanchar, J.M., and Hoskin, P.W.O., eds., Zircon: Reviews in Mineralogy & Geochemistry, v. 53, p. 277–304, https://doi.org/10.1515/9781501509322-013.

Forte, A.M., 2012, Late Cenozoic evolution of the Greater Caucasus Mountains and Kura foreland basin: Implications for early orogenesis [Ph.D. dissertation]: Davis, University of California, 338 p.

Forte, A.M., and Cowgill, E., 2013, Late Cenozoic base-level variations of the Caspian Sea: A review of its history and proposed driving mechanisms: Palaeogeography, Palaeoclimatology, Palaeoecology, v. 386, p. 392–407, https://doi.org/10.1016/j.palaeo.2013.05.035.

Forte, A.M., Cowgill, E., Bernardin, T., Kreylos, O., and Hamann, B., 2010, Late Cenozoic deformation of the Kura fold-thrust belt, southern Greater Caucasus: Geological Society of America Bulletin, v. 122, p. 465–486, https://doi.org/10.1130/B26464.1.

Forte, A.M., Cowgill, E., Murtuzayev, I., Kangarli, T., and Stoica, M., 2013, Structural geometries and magnitude of shortening in the eastern Kura fold-thrust belt, Azerbaijan: Implications for the development of the Greater Caucasus Mountains: Tectonics, v. 32, p. 688–717, https://doi.org/10.1002/tect.20032.

Forte, A.M., Cowgill, E., and Whipple, K.X., 2014, Transition from a singly vergent to doubly vergent wedge in a young orogen: The Greater Caucasus: Tectonics, v. 33, p. 2077–2101, https://doi.org/10.1002/2014TC003651.

Forte, A.M., Sumner, D.Y., Cowgill, E., Stoica, M., Murtuzayev, I., Kangarli, T., Elashvili, M., Godoladze, T., and Javakishvirli, Z., 2015a, Late Miocene to Pliocene stratigraphy of the Kura Basin, a subbasin of the South Caspian Basin: Implications for the diachroneity of stage boundaries: Basin Research, v. 27, p. 247–271, https://doi.org/10.1111/bre.12069.

Forte, A.M., Whipple, K.X., and Cowgill, E., 2015b, Drainage network reveals patterns and history of active deformation in the eastern Greater Caucasus: Geosphere, v. 11, p. 1343–1364, https://doi.org/10.1130/GES01121.1.

Forte, A.M., Gutterman, K.R., van Soest, M.C., and Gallagher, K., 2022, Building a young mountain range: Insight into the growth of the Greater Caucasus Mountains from detrital zircon (U-Th)/He thermochronology and ^{10}Be erosion rates: Tectonics, v. 41, https://doi.org/10.1029/2021TC006900.

Froggatt, P.C., 1992, Standardization of the chemical analysis of tephra deposits: Report of the ICCT Working Group: Quaternary International, v. 13–14, p. 93–96, https://doi.org/10.1016/1040-6182(92)90014-S.

Gabunia, L., Vekua, A., and Lordkipanidze, D., 2000, The environmental contexts of early human occupation of Georgia (Transcaucasia): Journal of Human Evolution, v. 38, p. 785–802, https://doi.org/10.1006/jhev.1999.0383.

Gamkrelidze, I., Shengelia, D., Tsutsunava, T., Chung, S.-L., Han, Y., and Chikhelidze, K., 2011, New data on the U-Pb zircon age of the Pre-Alpine crystalline basement of the Black-Sea-Central Transcaucasian Terrane and their geological significance: Bulletin of the Georgian National Academy of Sciences, v. 5, p. 64–76.

Gamkrelidze, I.P., 1986, Geodynamic evolution of the Caucasus and adjacent areas in Alpine time: Tectonophysics, v. 127, p. 261–277, https://doi.org/10.1016/0040-1951(86)90064-8.

Garber, K.L., Finzel, E.S., and Pearson, D.M., 2020, Provenance of synorogenic foreland basin strata in southwestern Montana requires revision of existing models for Laramide tectonism: North American Cordillera: Tectonics, v. 39, https://doi.org/10.1029/2019TC005944.

Gehrels, G., 2012, Detrital zircon U-Pb geochronology: Current methods and new opportunities, *in* Busby, C., and Azor, A., eds., Tectonics of Sedimentary Basins: Recent Advances: Chichester, UK, Blackwell Publishing, p. 47–62, https://doi.org/10.1002/9781444347166.ch2.

Gehrels, G., 2014, Detrital zircon U-Pb geochronology applied to tectonics: Annual Review of Earth and Planetary Sciences, v. 42, p. 127–149, https://doi.org/10.1146/annurev-earth-050212-124012.

Gehrels, G., Valencia, V., and Pullen, A., 2006, Detrital zircon geochronology by laser-ablation multicollector ICPMS at the Arizona LaserChron Center, *in* Olszewski, T., ed., Geochronology: Emerging Opportunities: The Paleontological Society Papers, v. 12, p. 67–76, https://doi.org/10.1017/S1089332600001352.

Gehrels, G.E., Valencia, V.A., and Ruiz, J., 2008, Enhanced precision, accuracy, efficiency, and spatial resolution of U-Pb ages by laser ablation–multicollector–inductively coupled plasma–mass spectrometry: Geochemistry, Geophysics, Geosystems, v. 9, Q03017, https://doi.org/10.1029/2007GC001805.

Grömping, U., 2009, Variable importance assessment in regression: Linear regression versus random forest: The American Statistician, v. 63, p. 308–319, https://doi.org/10.1198/tast.2009.08199.
Gunnels, M., Yetrimishli, G., Kazimova, S., and Sandvol, E., 2020, Seismotectonic evidence for subduction beneath the Eastern Greater Caucasus: Geophysical Journal International, v. 224, p. 1825–1834, https://doi.org/10.1093/gji/ggaa522.
Harnois, L., 1988, The CIW index: A new chemical index of weathering: Sedimentary Geology, v. 55, p. 319–322, https://doi.org/10.1016/0037-0738(88)90137-6.
Herron, M.M., 1988, Geochemical classification of terrigenous sands and shales from core or log data: Journal of Sedimentary Petrology, v. 58, p. 820–829, https://doi.org/10.1306/212F8E77-2B24-11D7-8648000102C1865D.
Hoth, S., Adam, J., Kukowski, N., and Oncken, O., 2006, Influence of erosion on the kinematics of bivergent orogens: Results from scaled sandbox simulations, *in* Willett, S.D., Hovius, N., Brandon, M.T., and Fisher, D.M., eds., Tectonics, Climate, and Landscape Evolution: Geological Society of America Special Paper 398, p. 201–225, https://doi.org/10.1130/2006.2398(12).
Hoth, S., Hoffmann-Rothe, A., and Kukowski, N., 2007, Frontal accretion: An internal clock for bivergent wedge deformation and surface uplift: Journal of Geophysical Research: Solid Earth, v. 112, B06408, https://doi.org/10.1029/2006JB004357.
Ingersoll, R.V., 1990, Actualistic sandstone petrofacies: Discriminating modern and ancient source rocks: Geology, v. 18, p. 733–736, https://doi.org/10.1130/0091-7613(1990)018<0733:ASPDMA>2.3.CO;2.
Ingersoll, R.V., Bullard, T.F., Ford, R.L., Grimm, J.P., Pickle, J.D., and Sares, S.W., 1984, The effect of grain size on detrital modes: A test of the Gazzi-Dickinson point-counting method: Journal of Sedimentary Petrology, v. 54, p. 103–116, https://doi.org/10.1306/212F83B9-2B24-11D7-8648000102C1865D.
Jackson, J., 1992, Partitioning of strike-slip convergent motion between Eurasia and Arabia in eastern Turkey and the Caucasus: Journal of Geophysical Research: Solid Earth, v. 97, p. 12,471–12,479, https://doi.org/10.1029/92JB00944.
Jian, D., Williams, S.E., Yu, S., and Zhao, G., 2022, Quantifying the link between the detrital zircon record and tectonic settings: Journal of Geophysical Research: Solid Earth, v. 127, https://doi.org/10.1029/2022JB024606.
Jones, R.W., and Simmons, M.D., 1996, A review of the stratigraphy of Eastern Paratethys (Oligocene–Holocene): Bulletin of the Natural History Museum of London, v. 52, p. 25–49.
Karapetian, S.G., Jrbashian, R.T., and Mnatsakanian, A.K., 2001, Late collision rhyolitic volcanism in the north-eastern part of the Armenian Highland: Journal of Volcanology and Geothermal Research, v. 112, p. 189–220, https://doi.org/10.1016/S0377-0273(01)00241-4.
Khain, V.E., 1975, Structure and main stages in the tectono-magmatic development of the Caucasus: An attempt at geodynamic interpretation: American Journal of Science, v. 275-A, p. 131–156.
Kopp, M.L., and Shcherba, I.G., 1985, Late Alpine development of the east Caucasus: Geotectonics, v. 19, p. 497–507.
Kovda, I., Mora, C.I., and Wilding, L.P., 2008, PaleoVertisols of the northwest Caucasus: (Micro) morphological, physical, chemical, and isotopic constraints on early to late Pleistocene climate: Journal of Plant Nutrition and Soil Science, v. 171, p. 498–508, https://doi.org/10.1002/jpln.200700037.
Kremenetskiy, A.A., Lapidus, A.V., and Voronovskiy, S.N., 1990, New data on the age and oil and gas potential of the basement of Kura depression, based on ultradeep well logs: Doklady of the National Academy of Sciences of the USSR, v. 312, p. 139–142.
Krijgsman, W., Stoica, M., Vasiliev, I., and Popov, V.V., 2010, Rise and fall of the Paratethys Sea during the Messinian salinity crisis: Earth and Planetary Science Letters, v. 290, p. 183–191, https://doi.org/10.1016/j.epsl.2009.12.020.
Krijgsman, W., et al., 2019, Quaternary time scales for the Pontocaspian domain: Interbasinal connectivity and faunal evolution: Earth-Science Reviews, v. 188, p. 1–40, https://doi.org/10.1016/j.earscirev.2018.10.013.
Kroonenberg, S.B., et al., 2005, Two deltas, two basins, one river, one sea: The modern Volga Delta as an analogue for the Neogene Productive Series, South Caspian Basin, *in* Giosan, L., and Bhattacharya, J.P, eds., River Deltas—Concepts, Models, and Examples: SEPM (Society for Sedimentary Geology) Special Publication 83, p. 231–256, https://doi.org/10.2110/pec.05.83.0231.
Krzanowski, W.J., 2000, Principles of Multivariate Analysis; A User's Perspective (revised edition): Oxford, UK, Oxford University Press, Oxford Statistical Science Series 22, 586 p., https://doi.org/10.1093/oso/9780198507086.001.0001.
Kuehn, S.C., Froese, D.G., and Shane, P.A.R., 2011, The INTAV intercomparison of electron-beam microanalysis of glass by tephrochronology laboratories: Results and recommendations: Quaternary International, v. 246, p. 19–47, https://doi.org/10.1016/j.quaint.2011.08.022.
Kvavadze, E.V., and Vekua, A.K., 1993, Vegetation and climate of the Dmanisi man period (East Georgia) from palynological data: Acta Palaeobotanica, v. 23, p. 343–355.
Lasaga, A.C., Soler, J.M., Ganor, J., Burch, T.E., and Nagy, K.L., 1994, Chemical weathering rate laws and global geochemical cycles: Geochimica et Cosmochimica Acta, v. 58, p. 2361–2386, https://doi.org/10.1016/0016-7037(94)90016-7.
Laskowski, A.K., DeCelles, P.G., and Gehrels, G.E., 2013, Detrital zircon geochronology of Cordilleran retroarc foreland basin strata, western North America: Tectonics, v. 32, p. 1027–1048, https://doi.org/10.1002/tect.20065.
Lawrence, R.L., Cox, R., Mapes, R.W., and Coleman, D.S., 2011, Hydrodyanmic fractionation of zircon age populations: Geological Society of America Bulletin, v. 123, p. 295–305, https://doi.org/10.1130/B30151.1.
Lawton, T.F., Hunt, G.J., and Gehrels, G.E., 2010, Detrital zircon record of thrust belt unroofing in Lower Cretaceous synorogenic conglomerates, central Utah: Geology, v. 38, p. 463–466, https://doi.org/10.1130/G30684.1.
Lazarev, S., Jorissen, E.L., van de Velde, S., Rausch, L., Stoica, M., Wesselingh, F.P., Van Baak, C.G.C., Yanina, T.A., Aliyeva, E., and Krijgsman, W., 2019, Magneto-biostratigraphic age constraints on the palaeoenvironmental evolution of the South Caspian basin during the Early-Middle Pleistocene (Kura basin, Azerbaijan): Quaternary Science Reviews, v. 222, https://doi.org/10.1016/j.quascirev.2019.105895.
Lazarev, S., et al., 2021, Five-fold expansion of the Caspian Sea in the late Pliocene: New and revised magnetostratigraphic and $^{40}Ar/^{39}Ar$ age constraints on the Akchagylian Stage: Global and Planetary Change, v. 206, https://doi.org/10.1016/j.gloplacha.2021.103624.
Leary, R.J., DeCelles, P.G., Quade, J., Gehrels, G.E., and Waanders, G., 2016, The Liuqu Conglomerate, southern Tibet: Early Miocene basin development related to deformation within the Great Counter Thrust system: Lithosphere, v. 8, p. 427–450, https://doi.org/10.1130/L542.1.
Link, P.K., Fanning, C.M., and Beranek, L.P., 2005, Reliability and longitudinal change of detrital-zircon age spectra in the Snake River system, Idaho and Wyoming: An example of reproducing the bumpy barcode: Sedimentary Geology, v. 182, p. 101–142, https://doi.org/10.1016/j.sedgeo.2005.07.012.
Lowe, D.J., 2011, Tephrochronology and its application: A review: Quaternary Geochronology, v. 6, p. 107–153, https://doi.org/10.1016/j.quageo.2010.08.003.
Lowe, D.J., Pearce, N.J.G., Jorgensen, M.A., Kuehn, S.C., Tryon, C.A., and Hayward, C.L., 2017, Correlating tephras and cryptotephras using glass compositional analyses and numerical and statistical methods: Review and evaluation: Quaternary Science Reviews, v. 175, p. 1–44, https://doi.org/10.1016/j.quascirev.2017.08.003.
Malkowski, M.A., Sharman, G.R., Johnstone, S.A., Grove, M.J., Kimbrough, D.L., and Graham, S.A., 2019, Dilution and propagation of provenance trends in sand and mud: Geochemistry and detrital zircon geochronology of modern sediment from central California (U.S.A.): American Journal of Science, v. 319, p. 846–902, https://doi.org/10.2475/10.2019.02.
Mamedov, A.V., 1973, Geological structure of the Mid-Kura Depression: Baku, Elm, 193 p. [in Russian].
Martín-Fernández, J.A., Barceló-Vidal, C., and Pawlowsky-Glahn, V., 2003, Dealing with zeros and missing values in compositional data sets using nonparametric imputation: Mathematical Geology, v. 35, p. 253–278, https://doi.org/10.1023/A:1023866030544.
Mayringer, F., Treloar, P.J., Gerdes, A., Finger, F., and Shengelia, D., 2011, New age data from the Dzirula Massif, Georgia: Implications for the evolution of the Caucasian Variscides: American Journal of Science, v. 311, p. 404–441, https://doi.org/10.2475/05.2011.02.
McKenzie, D., Jackson, J., and Priestley, K., 2019, Continental collisions and the origin of subcrustal continental earthquakes: Canadian Journal of Earth Sciences, v. 56, p. 1101–1118, https://doi.org/10.1139/cjes-2018-0289.
Messager, E., Lordkipanidze, D., Delhon, C., and Ferring, C.R., 2010a, Palaeoecological implications of the Lower Pleistocene phytolith record from the Dmanisi Site (Georgia): Palaeogeography, Palaeoclimatology, Palaeoecology, v. 288, p. 1–13, https://doi.org/10.1016/j.palaeo.2010.01.020.
Messager, E., Lordkipanidze, D., Kvavadze, E., Ferring, C.R., and Voinchet, P., 2010b, Palaeoenvironmental reconstruction of Dmanisi site (Georgia) based on palaeobotanical data: Quaternary International, v. 223–224, p. 20–27, https://doi.org/10.1016/j.quaint.2009.12.016.
Morton, A., and Yaxley, G., 2007, Detrital apatite geochemistry and its application in provenance studies, *in* Arribas, J., Critelli, S., and Johnsson, M.J., eds., Sedimentary Provenance and Petrogenesis: Perspectives from Petrography and Geochemistry: Geological Society of America Special Paper 420, p. 319–344, https://doi.org/10.1130/2006.2420(19).
Morton, A.C., Allen, M.B., Simmons, M., Spathopoulos, F., Still, J., Hinds, D.J., Ismail-Zadeh, A., and Kroonenberg, S.B., 2003, Provenance patterns in a neotectonic basin: Pliocene and

Quaternary sediment supply to the South Caspian: Basin Research, v. 15, p. 321–337, https://doi.org/10.1046/j.1365-2117.2003.00208.x.
Mosar, J., Kangarli, T., Bochud, M., Glasmacher, U.A., Rast, A., Brunet, M.-F., and Sosson, M., 2010, Cenozoic-Recent tectonics and uplift in the Greater Caucasus: A perspective from Azerbaijan, *in* Sosson, M., Kaymakci, N., Stephenson, R.A., Bergerat, F., and Starostenko, V.I., eds., Sedimentary Basin Tectonics from the Black Sea and Caucasus to the Arabian Platform: Geological Society of London Special Publication 340, p. 261–280, https://doi.org/10.1144/SP340.12.
Mumladze, T., Forte, A.M., Cowgill, E.S., Trexler, C.C., Niemi, N.A., Yikilmaz, M.B., and Kellogg, L.H., 2015, Subducted, detached, and torn slabs beneath the Greater Caucasus: GeoResJ, v. 5, p. 36–46, https://doi.org/10.1016/j.grj.2014.09.004.
Nagel, S., Castelltort, S., Garzanti, E., Lin, A.T., Willett, S.D., Mouthereau, F., Limonta, M., and Adatte, T., 2014, Provenance evolution during arc-continent collision: Sedimentary petrography of Miocene to Pleistocene sediments in the western foreland basin of Taiwan: Journal of Sedimentary Research, v. 84, p. 513–528, https://doi.org/10.2110/jsr.2014.44.
Nesbitt, H.W., and Young, G.M., 1982, Early Proterozoic climates and plate motions inferred from major element chemistry of lutites: Nature, v. 299, p. 715–717, https://doi.org/10.1038/299715a0.
Ogg, J.G., 2020, Geomagnetic Polarity Time Scale, *in* Gradstein, F.M., Ogg, J.G., Schmitz, M.D., and Ogg, G.M., eds., Geologic Time Scale 2020: Amsterdam, Elsevier, v. 1, p. 159–192, https://doi.org/10.1016/B978-0-12-824360-2.00005-X.
Palcu, D.V., Vasiliev, I., Stoica, M., and Krijgsman, W., 2019, The end of the Great Khersonian Drying of Eurasia: Magnetostratigraphic dating of the Maeotian transgression in the Eastern Paratethys: Basin Research, v. 31, p. 33–58, https://doi.org/10.1111/bre.12307.
Panaiotu, C.E., Vasiliev, I., Panaiotu, C.G., Krijgsman, W., and Langereis, C.G., 2007, Provenance analysis as a key to orogenic exhumation: A case study from the East Carpathians (Romania): Terra Nova, v. 19, p. 120–126, https://doi.org/10.1111/j.1365-3121.2006.00726.x.
Pawlowsky-Glahn, V., and Egozcue, J.J., 2006, Compositional data and their analysis: An introduction, *in* Buccianti, A., Mateu-Figueras, G., and Pawlowsky-Glahn, V., eds., Compositional Data Analysis in the Geosciences: From Theory to Practice: Geological Society of London Special Publication 264, p. 1–10, https://doi.org/10.1144/GSL.SP.2006.264.01.01.
Pe-Piper, G., Triantafyllidis, S., and Piper, D.J.W., 2008, Geochemical identification of clastic sediment provenance from known sources of similar geology: The Cretaceous Scotian Basin, Canada: Journal of Sedimentary Research, v. 78, p. 595–607, https://doi.org/10.2110/jsr.2008.067.
Perkins, M.E., Nash, W.P., Brown, F.H., and Fleck, R.J., 1995, Fallout tuffs of Trapper Creek, Idaho—A record of Miocene explosive volcanism in the Snake River Plain volcanic province: Geological Society of America Bulletin, v. 107, p. 1484–1506, https://doi.org/10.1130/0016-7606(1995)107<1484:FTOTCI>2.3.CO;2.
Philip, H., Cisternas, A., Gvishiani, A., and Gorshkov, A., 1989, The Caucasus: An actual example of the initial stages of continental collision: Tectonophysics, v. 161, p. 1–21, https://doi.org/10.1016/0040-1951(89)90297-7.
Popov, S.V., Shcherba, I.G., Ilyina, L.B., Nevesskaya, L.A., Paramonova, N.P., Khondkarian, S.O., and Magyar, I., 2006, Late Miocene to Pliocene palaeogeography of the Paratethys and its relation to the Mediterranean: Palaeogeography, Palaeoclimatology, Palaeoecology, v. 238, p. 91–106, https://doi.org/10.1016/j.palaeo.2006.03.020.
Popov, S.V., Antipov, M.P., Zastroshnov, A.S., Kurina, E.E., and Pinchuk, T.N., 2010, Sea-level fluctuations on the northern shelf of the eastern Paratethys in the Oligocene-Neogene: Stratigraphy and Geological Correlation, v. 18, p. 200–224, https://doi.org/10.1134/S0869593810020073.
Raines, M.K., Hubbard, S.M., Kukulski, R.B., Leier, A.L., and Gehrels, G.E., 2013, Sediment dispersal in an evolving foreland: Detrital zircon geochronology from Upper Jurassic and lowermost Cretaceous strata, Alberta Basin, Canada: Geological Society of America Bulletin, v. 125, p. 741–755, https://doi.org/10.1130/B30671.1.
R Core Team, 2010, R: A language and environment for statistical computing: Vienna, Austria, R Foundation for Statistical Computing, http://www.r-project.org (last accessed 1 July 2012).
Reilinger, R., et al., 2006, GPS constraints on continental deformation in the Africa-Arabia-Eurasia continental collision zone and implications for the dynamics of plate interactions: Journal of Geophysical Research, v. 111, B05411, https://doi.org/10.1029/2005JB004051.
Reynolds, A.D., et al., 1998, Implications of outcrop geology for reservoirs in the Neogene Productive Series: Apsheron Peninsula, Azerbaijan: American Association of Petroleum Geologists Bulletin, v. 82, p. 25–49, https://doi.org/10.1306/1D9BC38B-172D-11D7-8645000102C1865D.
Richards, K., van Baak, C.G.C., Athersuch, J., Hoyle, T.M., Stoica, M., Austin, W.E.N., Cage, A.G., Wonders, A.A.H., Marret, F., and Pinnington, C.A., 2018, Palynology and micropalaeontology of the Pliocene-Pleistocene transition in outcrop from the western Caspian Sea, Azerbaijan: Potential links with the Mediterranean, Black Sea and the Arctic Ocean?: Palaeogeography, Palaeoclimatology, Palaeoecology, v. 511, p. 119–143, https://doi.org/10.1016/j.palaeo.2018.07.018.
Roe, G.H., Whipple, K.X., and Fletcher, J.K., 2008, Feedbacks among climate, erosion, and tectonics in a critical wedge orogen: American Journal of Science, v. 308, p. 815–842, https://doi.org/10.2475/07.2008.01.
Rolland, Y., Sosson, M., Adamia, S., and Sadradze, N., 2011, Prolonged Variscan to Alpine history of an active Eurasian margin (Georgia, Armenia) revealed by $^{40}Ar/^{39}Ar$ dating: Gondwana Research, v. 20, p. 798–815, https://doi.org/10.1016/j.gr.2011.05.007.
Roman, D.C., Campisano, C., Quade, J., DiMaggio, E., Arrowsmith, J.R., and Feibel, C., 2008, Composite tephrostratigraphy of the Dikika, Gona, Hadar, and Ledi-Geraru project areas, northern Awash, Ethiopia, *in* Quade, J., and Wynn, J.G., eds., The Geology of Early Humans in the Horn of Africa: Geological Society of America Special Paper 446, p. 119–134, https://doi.org/10.1130/2008.2446(05).
Roser, B.P., and Korsch, R.J., 1986, Determination of tectonic setting of sandstone-mudstone suites using SiO_2 and K_2O/Na_2O ratio: The Journal of Geology, v. 94, p. 635–650, https://doi.org/10.1086/629071.
Roser, B.P., and Korsch, R.J., 1988, Provenance signatures of sandstone-mudstone suites determined using discriminant function analysis of major-element data: Chemical Geology, v. 67, p. 119–139, https://doi.org/10.1016/0009-2541(88)90010-1.
Safonova, I., Maruyama, S., Hirata, T., Kon, Y., and Rino, S., 2010, LA ICP MS U-Pb ages of detrital zircons from Russia largest rivers: Implications for major granitoid events in Eurasia and global episodes of supercontinent formation: Journal of Geodynamics, v. 50, p. 134–153, https://doi.org/10.1016/j.jog.2010.02.008.
Saintot, A., Brunet, M.-F., Yakovlev, F., Sébrier, M., Stephenson, R., Ershov, A., Chalot-Prat, F., and McCann, T., 2006, The Mesozoic-Cenozoic tectonic evolution of the Greater Caucasus, *in* Gee, D.G., and Stephenson, R.A., eds., European Lithosphere Dynamics: Geological Society of London Memoir 32, p. 277–289, https://doi.org/10.1144/GSL.MEM.2006.032.01.16.
Saylor, J.E., and Sundell, K.E., 2016, Quantifying comparison of large detrital geochronology data sets: Geosphere, v. 12, p. 203–220, https://doi.org/10.1130/GES01237.1.
Shcherbakov, V., Bindeman, I., and Gazeev, V., 2022, Geochemical, isotopic and petrological constraints on the origin and evolution of the recent silicic magmatism of the Greater Caucasus: Minerals (Basel), v. 12, 105, https://doi.org/10.3390/min12010105.
Shengelia, D., Shubitidze, L., Chung, S.-L., Chiu, H.-Y., and Treloar, P., 2012, New data on the formation and age of orthoclase gabbro of the Dzirula crystalline massif (Georgia): Bulletin of the Georgian National Academy of Sciences, v. 6, p. 75–82.
Shikhalibeyli, E.S., Abdullayev, R.N., and Ali-Zade, A.A., 1988, Geological results from the Saatly superdeep drillhole: International Geology Review, v. 30, p. 1272–1277, https://doi.org/10.1080/00206818809466108.
Shimodaira, H., 2004, Approximately unbiased tests of regions using multistep-multiscale boot-strap resampling: Annals of Statistics, v. 32, p. 2616–2641, https://doi.org/10.1214/009053604000000823.
Sinclair, H.D., 1997, Flysch to molasse transition in peripheral foreland basins: The role of the passive margin versus slab breakoff: Geology, v. 25, p. 1123–1126, https://doi.org/10.1130/0091-7613(1997)025<1123:FTMTIP>2.3.CO;2.
Skobeltsyn, G., Mellors, R., Gök, R., Türkelli, N., Yetirmishli, G., and Sandvol, E., 2014, Upper mantle *S* wave velocity structure of the East Anatolian-Caucasus region: Tectonics, v. 33, p. 207–221, https://doi.org/10.1002/2013TC003334.
Smosna, R., Bruner, K.R., and Burns, A., 1999, Numerical analysis of sandstone composition, provenance, and paleogeography: Journal of Sedimentary Research, v. 69, p. 1063–1070, https://doi.org/10.2110/jsr.69.1063.
Sobornov, K., 2021, Structure and evolution of the Terek-Caspian fold-and-thrust belt: New insights from regional seismic data: Journal of Petroleum Geology, v. 44, p. 259–286, https://doi.org/10.1111/jpg.12793.
Sobornov, K.O., 1994, Structure and petroleum potential of the Dagestan thrust belt, northeastern Caucasus, Russia: Bulletin of Canadian Petroleum Geology, v. 42, p. 352–364.
Sobornov, K.O., 1996, Lateral variations in structural styles of tectonic wedging in the northeastern Caucasus: Bulletin of Canadian Petroleum Geology, v. 44, p. 385–399.
Somin, M.L., 2011, Pre-Jurassic basement of the Greater Caucasus: Brief overview: Turkish Journal of Earth Sciences, v. 20, p. 546–610, https://doi.org/10.3906/yer-1008-6.
Spencer, C.J., Kirkland, C.L., and Roberts, N.M.W., 2018, Implications of erosion and bedrock composition on zircon fertility: Examples from South America and Western Australia: Terra Nova, v. 30, p. 289–295, https://doi.org/10.1111/ter.12338.

Stolar, D.B., Willett, S.D., and Roe, G.H., 2006, Climatic and tectonic forcing of a critical orogen, *in* Willett, S.D., Hovius, N., Brandon, M.T., and Fisher, D.M., eds., Tectonics, Climate, and Landscape Evolution: Geological Society of America Special Paper 398, p. 241–250, https://doi.org/10.1130/2006.2398(14).

Sukhishvili, L., Forte, A.M., Merebashvili, G., Leonard, J., Whipple, K.X., Javakhishvili, Z., Heimsath, A., and Godoladze, T., 2021, Active deformation and Plio-Pleistocene fluvial reorganization of the western Kura fold–thrust belt, Georgia: Implications for the evolution of the Greater Caucasus Mountains: Geological Magazine, v. 158, p. 583–597, https://doi.org/10.1017/S0016756820000709.

Sundell, K.E., and Saylor, J.E., 2017, Unmixing detrital geochronology age distributions: Geochemistry, Geophysics, Geosystems, v. 18, p. 2872–2886, https://doi.org/10.1002/2016GC006774.

Suzuki, R., and Shimodaira, H., 2009, pvclust: Hierarchical clustering with P-values via multiscale bootstrap resampling: http://www.is.titech.ac.jp/~shimo/prog/pvclust/ (last accessed 1 July 2012).

Tibaldi, A., Russo, E., Bonali, F.L., Alania, V., Chabukiani, A., Enukidze, O., and Tsereteli, N., 2017, 3-D anatomy of an active fault-propagation fold: A multidisciplinary case study from Tsaishi, western Caucasus (Georgia): Tectonophysics, v. 717, p. 253–269, https://doi.org/10.1016/j.tecto.2017.08.006.

Tibaldi, A., Bonali, F.L., Russo, E., and Pasquarè Mariotto, F.A., 2018, Structural development and stress evolution of an arcuate fold-and-thrust system, southwestern Greater Caucasus, Republic of Georgia: Journal of Asian Earth Sciences, v. 156, p. 226–245, https://doi.org/10.1016/j.jseaes.2018.01.025.

Tibaldi, A., Babayev, G., Bonali, F.L., Pasquaré Mariotto, F., Russo, E., Tsereteli, N., and Corti, N., 2021, Active kinematics of the Greater Caucasus from seismological and GPS data: A review, *in* Bonali, F.L., Pasquaré Mariotto, F., and Tsereteli, N., eds., Building Knowledge for Geohazard Assessment and Management in the Caucasus and Other Orogenic Regions: Dordrecht, Springer Netherlands, NATO Science for Peace and Security Series C: Environmental Security, p. 33–57, https://doi.org/10.1007/978-94-024-2046-3_4.

Totten, M.W., Hanan, M.A., and Weaver, B.L., 2000, Beyond whole-rock geochemistry of shales: The importance of assessing mineralogic controls for revealing tectonic discriminants of multiple sediment sources for the Ouachita Mountain flysch deposits: Geological Society of America Bulletin, v. 112, p. 1012–1022, https://doi.org/10.1130/0016-7606(2000)112<1012:BWGOST>2.0.CO;2.

Trexler, C.C., Cowgill, E., Spencer, J.Q.G., and Godoladze, T., 2020, Rate of active shortening across the southern thrust front of the Greater Caucasus in western Georgia from kinematic modeling of folded river terraces above a listric thrust: Earth and Planetary Science Letters, v. 544, https://doi.org/10.1016/j.epsl.2020.116362.

Trexler, C.C., Cowgill, E.S., Niemi, N.A., Vasey, D.A., and Godoladze, T., 2022, Tectonostratigraphy and major structures of the Georgian Greater Caucasus: Implications for structural architecture, along-strike continuity, and orogen evolution: Geosphere, v. 18, p. 211–240, https://doi.org/10.1130/GES02385.1.

Trexler, C.C., Cowgill, E.S., Vasey, D.A., and Niemi, N.A., 2023, Total shortening estimates across the western Greater Caucasus Mountains from balanced cross sections and area balancing: Tektonika, v. 1, p. 198–208, https://doi.org/10.55575/tektonika2023.1.2.50.

Tsereteli, N., Tibaldi, A., Alania, V., Gventsadse, A., Enukidze, O., Varazanashvili, O., and Müller, B.I.R., 2016, Active tectonics of central-western Caucasus, Georgia: Tectonophysics, v. 691, p. 328–344, https://doi.org/10.1016/j.tecto.2016.10.025.

Tye, A.R., Wolf, A.S., and Niemi, N.A., 2019, Bayesian population correlation: A probabilistic approach to inferring and comparing population distributions for detrital zircon ages: Chemical Geology, v. 518, p. 67–78, https://doi.org/10.1016/j.chemgeo.2019.03.039.

Tye, A.R., Niemi, N.A., Safarov, R.T., Kadirov, F.A., and Babayev, G.R., 2020, Sedimentary response to a collision orogeny recorded in detrital zircon provenance of Greater Caucasus foreland basin sediments: Basin Research, v. 33, p. 933–967, https://doi.org/10.1111/bre.12499.

Tye, A.R., Niemi, N.A., Cowgill, E., Kadirov, F.A., and Babayev, G.R., 2022, Diverse deformation mechanisms and lithologic controls in an active orogenic wedge: Structural geology and thermochronometry of the eastern Greater Caucasus: Tectonics, v. 41, https://doi.org/10.1029/2022TC007349.

van Baak, C.G.C., 2010, Glacio-marine transgressions of the early and middle Pleistocene Caspian Basin, Azerbaijan [MS thesis]: Utrecht, Netherlands, Utrecht University, 21 p.

Van Baak, C.G.C., Vasiliev, I., Stoica, M., Kuiper, K.F., Forte, A.M., Aliyeva, E., and Krijgsman, W., 2013, A magnetostratigraphic time frame for Plio-Pleistocene transgressions in the South Caspian Basin, Azerbaijan: Global and Planetary Change, v. 103, p. 119–134, https://doi.org/10.1016/j.gloplacha.2012.05.004.

van Baak, C.G.C., Stoica, M., Grothe, A., Aliyeva, E., and Krijgsman, W., 2016, Mediterranean-Paratethys connectivity during the Messinian salinity crisis: The Pontian of Azerbaijan: Global and Planetary Change, v. 141, p. 63–81, https://doi.org/10.1016/j.gloplacha.2016.04.005.

van Baak, C.G.C., et al., 2017, Paratethys response to the Messinian salinity crisis: Earth-Science Reviews, v. 172, p. 193–223, https://doi.org/10.1016/j.earscirev.2017.07.015.

Van Baak, C.G.C., Grothe, A., Richards, K., Stoica, M., Aliyeva, E., Davies, G.R., Kuiper, K.F., and Krijgsman, W., 2019, Flooding of the Caspian Sea at the intensification of Northern Hemisphere Glaciations: Global and Planetary Change, v. 174, p. 153–163, https://doi.org/10.1016/j.gloplacha.2019.01.007.

van der Boon, A., van Hinsbergen, D.J.J., Rezaeian, M., Gürer, D., Honarmand, M., Pastor-Galán, D., Krijgsman, W., and Langereis, C.G., 2018, Quantifying Arabia–Eurasia convergence accommodated in the Greater Caucasus by paleomagnetic reconstruction: Earth and Planetary Science Letters, v. 482, p. 454–469, https://doi.org/10.1016/j.epsl.2017.11.025.

van Hinsbergen, D.J.J., Torsvik, T.H., Schmid, S.M., Maţenco, L.C., Maffione, M., Vissers, R.L.M., Gürer, D., and Spakman, W., 2019, Orogenic architecture of the Mediterranean region and kinematic reconstruction of its tectonic evolution since the Triassic: Gondwana Research, v. 81, p. 79–229, https://doi.org/10.1016/j.gr.2019.07.009.

Vasey, D.A., Cowgill, E., Roeske, S.M., Niemi, N.A., Godoladze, T., Skhirtladze, I., and Gogoladze, S., 2020, Evolution of the Greater Caucasus basement and formation of the Main Caucasus Thrust, Georgia: Tectonics, v. 39, https://doi.org/10.1029/2019TC005828.

Vasey, D.A., Cowgill, E., and Cooper, K.M., 2021, A preliminary framework for magmatism in modern continental back-arc basins and its application to the Triassic-Jurassic tectonic evolution of the Caucasus: Geochemistry, Geophysics, Geosystems, v. 22, https://doi.org/10.1029/2020GC009490.

Vasey, D.A., Garcia, L., Cowgill, E., Trexler, C.C., and Godoladze, T., 2024, Episodic evolution of a protracted convergent margin revealed by detrital zircon geochronology in the Greater Caucasus: Basin Research, v. 36, https://doi.org/10.1111/bre.12825.

Vasiliev, I., Iosifidi, A.G., Khramov, A.N., Krijgsman, W., Kuiper, K.F., Langereis, C.G., Popov, V.V., Stoica, M., Tomsha, V.A., and Yudin, S.V., 2011, Magnetostratigraphy and radio-isotope dating of upper Miocene–lower Pliocene sedimentary successions of the Black Sea Basin (Taman Peninsula, Russia): Palaeogeography, Palaeoclimatology, Palaeoecology, v. 310, p. 163–175, https://doi.org/10.1016/j.palaeo.2011.06.022.

Vasiliev, I., et al., 2022, Biomarkers reveal two paramount Pliocene-Pleistocene connectivity events in the Caspian Sea Basin: Palaeogeography, Palaeoclimatology, Palaeoecology, v. 587, p. 110802, https://doi.org/10.1016/j.palaeo.2021.110802.

Venables, W.N., and Ripley, B.D., 2002, Modern Applied Statistics with S: New York, Springer-Verlag, 495 p., https://doi.org/10.1007/978-0-387-21706-2.

Vermeesch, P., 2012, On the visualization of detrital age distributions: Chemical Geology, v. 312–313, p. 190–194, https://doi.org/10.1016/j.chemgeo.2012.04.021.

Vermeesch, P., 2013, Multi-sample comparison of detrital age distributions: Chemical Geology, v. 341, p. 140–146, https://doi.org/10.1016/j.chemgeo.2013.01.010.

Vezzoli, G., Garzanti, E., Vincent, S.J., Andò, S., Carter, A., and Resentini, A., 2014, Tracking sediment provenance and erosional evolution of the western Greater Caucasus: Earth Surface Processes and Landforms, v. 39, p. 1101–1114, https://doi.org/10.1002/esp.3567.

Vezzoli, G., Garzanti, E., Limonta, M., and Radeff, G., 2020, Focused erosion at the core of the Greater Caucasus: Sediment generation and dispersal from Mt. Elbrus to the Caspian Sea: Earth-Science Reviews, v. 200, https://doi.org/10.1016/j.earscirev.2019.102987.

Vincent, S.J., Morton, A.C., Carter, A., Gibbs, S., and Barabadze, T.G., 2007, Oligocene uplift of the Western Greater Caucasus: An effect of initial Arabia-Eurasia collision: Terra Nova, v. 19, p. 160–166, https://doi.org/10.1111/j.1365-3121.2007.00731.x.

Vincent, S.J., Davies, C.E., Richards, K., and Aliyeva, E., 2010, Contrasting Pliocene fluvial depositional systems within the rapidly subsiding South Caspian Basin: A case study of the palaeo-Volga and palaeo-Kura river systems in the Surakhany Suite, Upper Productive Series, onshore Azerbaijan: Marine and Petroleum Geology, v. 27, p. 2079–2106, https://doi.org/10.1016/j.marpetgeo.2010.09.007.

Vincent, S.J., Morton, A.C., Hyden, F., and Fanning, M., 2013, Insights from petrography, mineralogy and U-Pb zircon geochronology into the provenance and reservoir potential of Cenozoic siliciclastic depositional systems supplying the northern margin of the Eastern Black Sea: Marine and Petroleum Geology, v. 45, p. 331–348, https://doi.org/10.1016/j.marpetgeo.2013.04.002.

Vincent, S.J., Hyden, F., and Braham, W., 2014, Along-strike variations in the composition of sandstones derived from the uplifting western Greater Caucasus: Causes and implications

for reservoir quality prediction in the Eastern Black Sea, *in* Scott, R.A., Smyth, H.R., Morton, A.C., and Richardson, N., eds., Sediment Provenance Studies in Hydrocarbon Exploration and Production: Geological Society of London Special Publication 386, p. 111–127, https://doi.org/10.1144/SP386.15.

Vincent, S.J., Braham, W., Lavrishchev, V.A., Maynard, J.R., and Harland, M., 2016, The formation and inversion of the western Greater Caucasus Basin and the uplift of the western Greater Caucasus: Implications for the wider Black Sea region: Tectonics, v. 35, p. 2948–2962, https://doi.org/10.1002/2016TC004204.

Vincent, S.J., Saintot, A., Mosar, J., Okay, A.I., and Nikishin, A.M., 2018, Comment on "Relict basin closure and crustal shortening budgets during continental collision: An example from Caucasus sediment provenance" by Cowgill et al (2016): Tectonics, v. 37, p. 1006–1016, https://doi.org/10.1002/2017TC004515.

Vincent, S.J., Somin, M.L., Carter, A., Vezzoli, G., Fox, M., and Vautravers, B., 2020, Testing models of Cenozoic exhumation in the western Greater Caucasus: Tectonics, v. 39, https://doi.org/10.1029/2018TC005451.

Von Eynatten, H., 2003, Petrography and chemistry of sandstones from the Swiss Molasse Basin: An archive of the Oligocene to Miocene evolution of the Central Alps: Sedimentology, v. 50, p. 703–724, https://doi.org/10.1046/j.1365-3091.2003.00571.x.

von Eynatten, H., Barceló-Vidal, C., and Pawlowsky-Glahn, V., 2003, Composition and discrimination of sandstones: A statistical evaluation of different analytical methods: Journal of Sedimentary Research, v. 73, p. 47–57, https://doi.org/10.1306/070102730047.

Wang, C.Y., Campbell, I.H., Stepanov, A.S., Allen, C.M., and Burtsev, I.N., 2011, Growth rate of the preserved continental crust: II. Constraints from Hf and O isotopes in detrital zircons from Greater Russian Rivers: Geochimica et Cosmochimica Acta, v. 75, p. 1308–1345, https://doi.org/10.1016/j.gca.2010.12.010.

Whipple, K.X., and Meade, B.J., 2004, Controls on the strength of coupling among climate, erosion, and deformation in two-sided, frictional orogenic wedges at steady state: Journal of Geophysical Research: Earth Surface, v. 109, F01011, https://doi.org/10.1029/2003JF000019.

Whipple, K.X., and Meade, B.J., 2006, Orogen response to changes in climatic and tectonic forcing: Earth and Planetary Science Letters, v. 243, p. 218–228, https://doi.org/10.1016/j.epsl.2005.12.022.

Žák, J., Svojtka, M., Hajná, J., and Ackerman, L., 2020, Detrital zircon geochronology and processes in accretionary wedges: Earth-Science Reviews, v. 207, https://doi.org/10.1016/j.earscirev.2020.103214.

Zakariadze, G., Karpenko, S., Bazylev, B., Solov'eva, N., Lyalikov, A., Adamia, S.A., and Oberhänsli, R., 1998, Petrology, geochemistry, and Sm-Nd age of the pre-Late Hercynian paleooceanic complex of the Dzirula salient, Transcaucasian Massif: Petrology, v. 6, p. 388–408.

Zonenshain, L.P., and Le Pichon, X., 1986, Deep basins of the Black Sea and Caspian Sea as remnants of Mesozoic back-arc basins: Tectonophysics, v. 123, p. 181–211, https://doi.org/10.1016/0040-1951(86)90197-6.

Zubakov, V.A., and Borzenkova, I.I., 1990, Global Palaeoclimate of the Late Cenozoic: Amsterdam, Elsevier, 456 p.